Politechnika
Częstochowska

Wydział Inżynierii
Mechanicznej i Informatyki

PhD thesis

Analiza wpływu oddziaływania akustycznego na utratę stabilności przepływu w warstwie przyściennej

Analysis of the impact of acoustic excitation on the loss of flow stability in the boundary layer

mgr inż. Vasyl Sokolenko

Thesis supervisor:

Prof. dr hab Eng. Witold Elsner

Częstochowa, 2023

Acknowledgments:

I would like to express my heartfelt appreciation to Prof. dr hab Eng. Witold Elsner for providing the opportunity to work on the research project and for his invaluable assistance in conducting the experiment. I am grateful for the time he dedicated to me throughout the implementation of this doctoral thesis.

I extend my sincere gratitude to all the participants of the research project Dr. Eng. Artur Dróżdż, prof. PCz, Dr hab. Eng. Renata Gnatowska, Prof. PW dr hab. Eng. Sławomir Kubacki, and Dr. Eng. Zbigniew Rarata for their valuable guidance in designing the research section, conducting measurements, and analysing the experimental data.

I would also like to take this opportunity to thank my family and loved ones for their unwavering support and patience during my research journey. Their presence and understanding played an important role in my progress and success.

Contents

Nomenclature

B	slope of the best fit line (–)	
C_f	skin friction coefficient (–)	
Cp	pressure coefficient (–)	$C_p(x) = (P_s(x) - P_{s_{in}})/(P_{tot} - P_{s_{in}})$
E	output voltage of hot-wire (volt)	
E_0	extrapolated value where U = zero, (volt)	
f	frequency (Hz)	
H	shape factor (–)	$H = \delta^*/\theta$
K	boundary–layer thickness δ^* wavelength (–)	
k	wavenumber (–)	$\mathrm{k} = 2\pi * f/U$
L_{APG}	length of APG	
L_s	position of separation onset (mm)	
n	number of periods (–)	
$P_{s_{in}}$	static pressure at the inlet plate (Pa)	
P_s	static pressure (Pa)	
P_{tot}	stagnation pressure in the freestream (Pa)	
$R11$	autocorrelation function (–)	
Re_{APG}	APG distance Reynolds number (–)	$Re_{L_{TE}} = U_2 L_{APG}/v$
Re_x	separation onset distance Reynolds number (–)	$Re_x = UL_s/v$
Re_{δ^*}	boundary–layer thickness Reynolds number (–)	$Re_{\delta^*} = U\delta^*/v$
Re_θ	momentum thickness Reynolds number (–)	$Re_\theta = U\theta/v$
St	Strouhal number	$St = f * \theta/U$
T_{11}	time macroscale (s)	$T_{11} = \int_0^\infty R_{11}(\tau)d\tau$
Tu	turbulent intensity (%)	$Tu = u'/U_{e\_in}$
T_h	threshold value (–)	

t	time (s)
U	mean velocity (m/s)
U_2	velocity at the trailing edge (m/s)
Ue_{in}	boundary layer edge velocity at the inlet plate (m/s)
U_{in}	mean velocity at the inlet plate (m/s)
U_∞	Free-stream velocity (m/s)
u'	root mean square values of fluctuating velocity (m/s)
u'_{max}	maximum value of u' (m/s)
x	distance in the measuring section (mm)
x_s	separation onset (mm)
x_m	position of maximum height of bubble (mm)
x_t	transition onset (mm)
x_T	end of the l-t transition (mm)
x_r	reattachment point (mm)

Greak symbols

η	Blasius boundary layer (–) $\eta = y\sqrt{U/\nu x}$
δ_{99}	boundary layer thickness (mm)
δ^*	boundary layer displacement thickness (mm)
θ	momentum thickness (mm)
Λ_{11}	integral length scale (m)
λ_{11}	Taylor microscale (s)
λ_K	average wavelength
μ	dynamic viscosity (Pa*s)
ν	kinematic viscosity (m^2/s)

τ_w	wall shear stress

Abbreviations:

APG	adverse pressure gradient
BL	boundary layer
DAQ	data acquisition systems
DI	direct injection
DSP	digital signal processor
FPG	favourable pressure gradient
LBL	laminar boundary layer
l-t	laminar-turbulent
NE	non–excitation
PN	pink noise
PSD	power spectra density
SPL	sound pressure level
TBL	turbulent boundary layer
TE	trailing edge
T-S	Tollmien–Schlichting
VGJ	vortex generating jets

1. Introduction

The understanding and prediction of the stability of laminar shear flows and the transition to turbulence are crucial in the field of fluid mechanics. A variety of factors such as surface roughness, free stream turbulence, surface curvature, pressure gradient, surface temperature, Mach number, Reynolds number, acoustic excitation, and fluid injection or suction at the wall can influence the transition process. Despite the many complexities involved, there is currently no comprehensive theory for the transition process, and the origin of turbulence remains a challenging problem in the field of fluid mechanics.

The study of the laminar-turbulent (l-t) transition and boundary layer separation is a crucial aspect of fluid dynamics, with significant implications for a wide range of industrial and natural systems, such as aircrafts, automobiles, ships, compressor blades, and wind turbines. The boundary layer separation refers to the thin layer of fluid that separates from the surface of an object as it moves through a fluid medium. The l-t transition can be associated with detachment of the flow and formation of a laminar separation bubble (LSB), which dimension can influence the overall efficiency and performance of various systems in energy engineering, aviation, marine industry etc. The size of the separation boundary layer is highly dependent on numerous factors, including the angle of inflow, friction, the shape of the surface, and the l-t transition process. That is why understanding the dynamics and behaviour of the separation boundary layer is crucial for the operation, safety, and optimisation of industrial systems. This knowledge may be used to improve the performance of these systems by developing techniques to control or delay the flow separation.

A common feature of rotating machinery, especially where high velocities are involved is acoustics. The systems found in the aviation industry are a good example. In modern turbofan engines, the boundary layers developing on the surfaces of turbine blades are exposed to strong perturbations caused by acoustic waves. A high concentration of acoustic energy inside such an engine can have a major impact on the stability of the laminar boundary layer and can trigger an earlier laminar-turbulent transition (Ezerskii, 1985). For current high by–pass ratio engine the sound spectrum consists of both tonal and broadband components, contributions of which come from all rotating machines i.e. the fan, the compressor, the turbine, but also from the combustion chamber and the jet (Moreau, 2019).

The acoustic energy generated by rotating machines may also have an effect on the stability of the flow and the formation of a separated boundary layer. Understanding the mechanisms behind these phenomena can lead to the development of improved designs for industrial systems, as well as a reduction in their environmental impact through increased efficiency.

The main focus of this study is to investigate the mechanism by which acoustics, generated as broadband noise or harmonic excitation, affect the laminar-turbulent transition process in a separated boundary layer. Through the use of advanced measurement techniques and data post processing, this study aims to provide a detailed understanding of the physical processes involved in the interaction between acoustics and the detached boundary layer, and how these interactions may be used to control or manipulate the transition process.

The investigation was supported by National Science Centre under Grant No. 2018/31/B/ST8/01717.

2. Literature review

History

Ludwig Prandtl's discovery of the separated boundary layer in 1904 marked a turning point in fluid dynamics comprehension and established the groundwork for contemporary aerodynamics. The boundary layer is an essential aspect of aerodynamics, since the performance of systems such as aircraft engines, wind turbines, and automobile structures is heavily impacted by itsbehaviour and its interaction with the surrounding flow. In particular, reverse flow created by boundary layer separation can result in undesirable outcomes, such as increased drag, reduced lift, and decreased efficiency (Carmichael, 1981; Jones et al., 2008; Mueller & DeLaurier, 2003). Consequently, understanding of boundary layer separation is crucial for achieving optimal performance across numerous applications. In 1951, (Schubauer & Klebanoff, 1951) conducted pioneering research on the impact of separation bubbles on turbulence development and the laminar-turbulent transition process. This ground–breaking work initiated ongoing investigations into the complex phenomenon of separation bubbles and their influence on flow behaviour, a topic that continues to be explored by researchers today.

When exposed to a sufficiently strong adverse pressure gradient (APG), a laminar boundary layer developing along an airfoil can separate. It is important to note that "laminar" in this context refers to the boundary layer condition at separation, not the flow regime throughout the bubble. In specific situations, when separation is unstable (see Figure 2.1), the increase in momentum exchange due to the transition from flow in the separated shear layer can cause reattachment. This results in the formation of a closed recirculation region near the surface, known as a laminar separation bubble (Schubauer & Klebanoff, 1951), in the time–averaged context. This phenomenon can lead to numerous negative effects. Consequently, a multitude of studies have been conducted to explore and predict the dynamic properties and stability features of LSB (Gaster & Grant, 1975; Tani, 1964; Dovgal et al., 1994; Watmuff, 1999).

L-T transition over LSB

Many existing studies focus on the laminar-turbulent transition in a separated shear layer (Dovgal et al., 1994; Lin & Pauley, 1996; Watmuff, 1999). The laminar-turbulent transition is highly sensitive to factors such as surface roughness, free-stream turbulence, or incident wakes. Piotrowski et al. (2010) have proposed a model for predicting transitions in wall–bounded flow, which has been compared with experimental data and other transition models. The investigation revealed that the proposed model has the potential to accurately replicate the important flow features. His study was conducted across a range of Reynolds numbers with varying degrees of inlet turbulence intensity.

Past research demonstrates that the transient process within the separated shear layer starts with the amplification of low–amplitude disturbances. This initial amplification takes place in the range of unstable frequencies and is accurately represented by linear stability theory (Häggmark et al., 2001; Marxen et al., 2012). According to Lou & Hourmouziadis (2000), the reattachment of the laminar separation bubble is primarily induced by the amplification of fluctuations in the separating shear layer. Their investigation focused on flows at four different Reynolds numbers, ranging from $Re_x = 2.9 \, x \, 10^5$ to $Re_x = 1.4 \, x \, 10^6$. The wave packet evolves into the characteristic cat's eye pattern, as experimentally demonstrated by Watmuff (Watmuff, 1999). As the perturbation amplitude increases, nonlinear interactions arise during the later stages of the transition (Alam & Sandham, 2000; Rist et al., 2004). Expanding perturbations can lead to the shear layer transition into periodically shedding vortices, as depicted in Figure 2.1. Shear layer vortices in the LSB were detected in flows over airfoils (Burgmann et al., 2006; Burgmann & Schröder, 2008; Jones et al., 2010; Wolf et al., 2011) and flat plates (Alam & Sandham, 2000; Marxen et al., 2012; Rist et al., 2004; Watmuff, 1999). It was shown that viscous effects diminish with increasing Reynolds number and the distance between the separated shear layer and the wall (Diwan & Ramesh, 2009; Dovgal et al., 1994; Ulrich et al., 1996). By incorporating these factors into the strong dependence on the displacement thickness Reynolds number Boutilier

& Yarusevych, (2012) demonstrated that the difference between the maximum amplification rate predicted by viscous and inviscid solutions is found to be within a 15% margin for all the examined profiles. This implies that the presence of viscosity does not significantly dampen the inviscid instability of this flow.

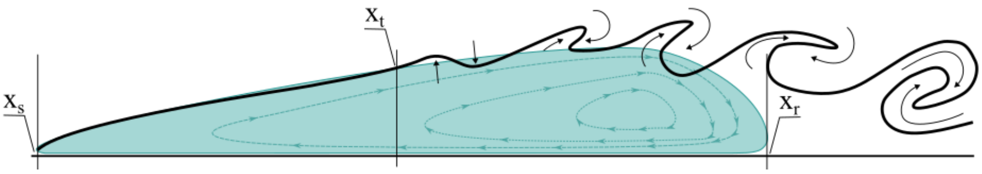

Figure 2.1 Sketch of separated boundary layer phenomena.

McAuliffe & Yaras, (2008) found that in APG flows with low freestream turbulence levels the growth of Tollmien–Schlichting (T-S) instability occurs downstream the separation point, leading to the formation of roll–up structures characteristic of Kelvin-Helmholtz (K-H) instability. This suggests that K-H instability may be preceded by the development of T-S waves. Talan & Hourmouziadis (2002) have reported a significant relationship between K-H instability at a relatively limited range of Strouhal numbers, specifically within the range of St = 0.008 – 0.012. Where St was calculated based on the momentum thickness at the separation point, velocity at the edge of the boundary layer at the separation point and frequency of the oscillating. Their research was carried out for steady and unsteady flow with a Reynolds number of $Re_x = 1.2 \times 10^5$.

Passive methods of controlling LSB

The negative impacts of the separation bubble phenomenon have led to numerous studies exploring the potential of passive control methods to influence the size of the separated bubble. Passive methods for controlling separated boundary layer flow refer to techniques that do not require the input of external energy or mechanical components. The overarching goal is to strengthen the boundary layer, making it more resistance against adverse pressure gradients. According to Sieverding et al., (2004) the use of rough surfaces or roughness elements has been effective in reducing or eliminating separation in fluid flows. However, their investigation also revealed several negative aspects associated with this approach. Specifically, rough surfaces were found to have little effect on low Reynolds number flows, which limits their applicability in certain situations. Additionally, the use of rough surfaces can lead to an increase in the weight and complexity of construction, which may be undesirable in practical applications. Volino (2003) conducted a study to evaluate the effectiveness of rectangular bars in preventing the formation of separation bubbles on turbine blades. The research demonstrated promising results; however, the efficiency of this method is dependent on both the Reynolds number and the size of the rectangular bars. This presents a challenge in determining the optimal size of rectangular bars for applications operating on a broad range of Reynolds numbers. Zhang et al., (2006) conducted a study examining the impact of surface trips on ultra high–lift blades. Their findings demonstrated the effectiveness of this approach in preventing boundary layer separation. The efficiency of this method can be attributed to the acceleration of the boundary layer transition process, both under and between wakes, facilitated by surface trips. Olsman & Colonius, (2011) conducted a direct numerical simulation (DNS) study which presents results for flows around airfoils with and without cavities, exploring flow regimes and physics. They observed two flow regimes in airfoils with cavities and the impact of oscillations on boundary layer separation. The research highlights complex flow physics involving multiple instabilities and suggests further experiments for deeper insights. (Açıkel & Serdar Genç, 2018) investigated the control methods of LSB on wind turbine airfoils at low Reynolds numbers using a partially flexible membrane. The membrane effectively suppressed LSB, increased lift coefficient, and reduced drag coefficient, leading to improved airfoil performance. The effectiveness of this flow control method decreased with increasing Reynolds numbers. The interaction between the partially flexible membrane and the LSB influenced the vibrations and deformation of the membrane, with different vibration modes observed. The results highlight the potential of using partially flexible membranes to control LSB and to improve the aerodynamic performance of wind turbine airfoils.

Active methods of control of LSB

An alternative approach to flow control is the implementation of active control methods. These techniques primarily involve the delivery of energy into the flow, which consequently changes the flow structure and potentially improves the aerodynamic performance of the system under consideration. By leveraging dynamic changes, active control methods can achieve enhanced efficiency and optimisation in a wide range of applications. Glezer & Amitay, (2002) showed the efficacy of vortex generating jets (VGJ) for controlling fluid flows on solid surfaces. The interaction between a synthetic jet and a cross–flow over a solid surface leads to the modification of the boundary layer and to a local displacement of the cross–flow. Goodfellow et al., (2011) conducted a study focusing on flow control utilizing synthetic jets at a low Reynolds number $Re = 10^4$. Their findings demonstrated a decrease in the drag coefficient, indicating the potential effectiveness of synthetic jets as a viable flow control mechanism in low–Reynolds–number regimes. Corke et al. (2011), in their research, effectively employed periodic plasma actuators for active flow control at two distinct Reynolds numbers, $2.17 \, x \, 10^5$ and $3.07 \, x \, 10^5$. The study presented the potential applicability of plasma actuators in managing flow dynamics across various Reynolds number regimes. (Rizzetta & Visbal, 2011) used the same method and show in their work the successful forcing of earlier l-t transition. Cattafesta and Sheplak, (2011) conducted a comprehensive review of various types of actuators, highlighting the technical challenges that must be addressed in order to improve their effectiveness. Their work offers valuable insight into the current state of actuator technology and the obstacles that need to be overcome for successful implementation in various applications. The large–eddy simulation (LES) investigation (Atzori et al., 2020) and experimental investigation (Eto et al., 2019; Kornilov et al., 2019) showed the significant efficiency of combined blowing/suction methods for boundary layer control. It was shown decreasing on the friction drag but the pressure drag increased more. It can be concluded that this method can be used for boundary layer control but its needs deeper knowledge.

Acoustic energy in the flow

In contemporary turbofan engines, boundary layers that form on compressor and turbine blade surfaces are subject to intense perturbations due to high acoustic energy levels. The high concentration of acoustic energy within such engines can affect the laminar boundary layer's stability, potentially causing an earlier transition from flow (Ezerskii, 1985). The sound spectrum of modern high–bypass ratio engines includes both tonal and broadband components (Moreau, 2019), which originate from various rotating elements such as the fan, compressor, turbine, combustion chamber, and jet. In most cases, multiple tones were observed (Arbey & Bataille, 1983; Chong & Joseph, 2012). The dominant or primary tone corresponds to the largest sound pressure fluctuations. These tones were linked to the dissipation of instability waves that begin upstream and are amplified by a separated shear layer at the trailing edge (Arbey & Bataille, 1983). Nash et al., (1999) observed that a separation bubble or separated shear layer in close proximity to the trailing edge is a necessary condition for the occurrence of such tones.

Acoustics excitation as method of flow control

Also, one of the methods for avoiding LSB is the usage of acoustics excitation. Gaster & Grant (1975) pioneered the introduction of impulsive perturbations, exciting a full spectrum of instability modes and generating a wavepacket via selective amplification. This study investigated the generation of a wave packet in the boundary layer using a pulsed input disturbance method. Despite the noise in the raw hot-wire anemometry signals, ensemble averaging and digital filtering helped to obtain clear data. The growth and development of the wave packet were analysed, and it was observed that distortions in the packet emerged as it propagated downstream.

The most prevalent type of applied impact is sinusoidal and other periodic excitation at the separated shear layer's most unstable frequency (Bernardini et al., 2012), which is typically determined using linear stability theory (LST) analysis. Consequently, tonal emissions might significantly influence flow development on the suction side of an airfoil in low-Reynolds number flows, resulting in substantial alterations in separation bubble dynamics and airfoil characteristics.

The impact of tonal excitation might also be crucial for experimental studies focusing on separation bubble dynamics, considering the well–documented sensitivity of LSB to test section environments (Ol et al., 2005). Various studies examining flow control over airfoils at low Reynolds numbers with acoustic excitation suggest that acoustic forcing can result in notable changes in detached shear layer development, especially on the suction side of the airfoil (Nishioka et al., 1990; Suzuki & Ishii, 2001; Zaman & McKinzie, 1991). Collins & Zelenevitz, (1975) describe an investigation of the effects of external sound on the flow over a static wing at high angles of attack 20.25° and 23.9° for velocities in the range from 12.6 to 27.3 m/s. In the study, the lift, drag, and moment coefficients of a wing with a NACA 2412 section were measured and the flow state was evaluated using tufts. As the sound source a tonal sound in the range from 739 to 7996 Hz and sound pressure level (SPL) range from 88 to 134 dB, produced by a speaker placed downstream and above the wing. The results indicated that partial attachment can occur with an increase in SPL, and once partial attachment occurs, the SPL can be greatly decreased without changing the wing properties. Also, an important observation is that increasing the angle of attack of the wing requires a higher SPL to force the reattachment of LSB. Zaman, (1992) summarizes experimental results on the effect of tonal acoustic excitation on separated flow at a large angle of wing attack. The study found that as the amplitude of excitation is increased, a large increase in lift is achieved, but the optimum effect shifts to a lower Strouhal number. The Strouhal number yielding the optimum effect can be an order of magnitude lower than that corresponding to the linear, inviscid instability of the separated shear layer. The study also notes that the observed lift breakdown associated with a separation bubble is characteristic of only the flow in which the separated shear layer is initially laminar.

The appearance of frequency of excitation can be explained by an acoustic feedback loop between trailing edge radiation and the receptivity region above. This is explained by the fact that acoustic waves introduce a phase change into instability waves arising in the area of receptivity region of the boundary layer, it was found that such an inverse acoustic relationship exists and is equal to $2\pi(n + 1/2)$, which was acquired through experiments (Arbey & Bataille, 1983; Plogmann et al., 2013; Schumacher et al., 2014; Takagi & Konishi, 2010) and simulations (Fosas de Pando et al., 2014; Jones et al., 2008). However, there is some debate regarding the location of the receptivity region of the upper boundary layer and the length of the feedback loop. Although Arbey & Bataille (1983) related the receptivity region to the maximum marginal velocity area, subsequent studies positioned it where the first instability occurs.

In many flow control studies addressing LSB on airfoils, the emphasis has been on changes in average LSB features and airfoil efficiency rather than concurrent changes in bubble dynamics. Yarusevych et al. (2007) connected the most effective excitation frequency to the frequency of the most amplified perturbations in undisturbed flow.

Broadband acoustic excitation

Kurelek et al. (2018) examined the effects of tonal and broadband acoustic excitation in the range 89.5–94.9 dB on flow development and transition in a laminar separation bubble on the suction side of a NACA 0018 airfoil. For study a closed-loop wind tunnel facility at a Reynolds number of $1.25\ x\ 10^5$ and an angle of attack of 4 degrees was used. The results showed that both tonal and broadband excitation produce similar changes in the mean separation bubble topology. Both lead to the delay of boundary layer separation, a reduction in the maximum bubble height, and upstream advancement in the shape factor maximum and mean reattachment locations. The impact of pink noise on the laminar boundary layer was also investigated by Sokolenko et al. (2021). The investigation reveal noticeable changes in fluctuation structures near the transition point and alterations in mean velocity profiles. Based on own experimental data and the reference experimental data by Kurelek et al. (2018), a modelling approach was proposed to describe this phenomenon using the RANS equations (Kubacki et al., 2023). In particular, the attempts have been made to extend the predictive capabilities of transitional algebraic intermittency model widely described in Kubacki & Dick (2016), by including the effect of external acoustic forcing on transition in separated boundary layer.

Summary

Summing up, the study of separated boundary layer physics has been the subject of extensive research in recent years. Much research has been aimed at understanding the underlying physics of the boundary layer, and of flow separation control methods. A lot of methods are being proposed for passive control of the boundary layer to prevent separation. Active control techniques, which involve supplying energy externally to the boundary layer and increasing the turbulence of the near wall flow, have also received significant attention recently. These works have highlighted the potential of using acoustic waves to actively control the boundary layer, while most of studies dealt with monoharmonic forcing. On the other hand, in real flow configurations, for example in aircraft engines, broadband noise is present, which also affects the near-wall flow. It should also be noted that noise level inside the aircraft engine is very high, reaching up to SPL = 150 dB. Studies in the available literature, only apart from the old one (Collins & Zelenevitz, 1975), have not exceeded the level of 100 dB, which is very far from real conditions. Additionally, the high level of sound pressure require specialised equipment such as professional loudspeakers and amplifiers.

Although most studies on active control of the separated boundary layer have been related to the use of periodic excitation, the effects of broadband acoustic waves on the boundary layer also have a huge impact and are still relatively poorly understood. Therefore, further research is needed to deepen our understanding of the effects of high–energy acoustic pressure and compare the effects of broadband and tonal excitation on the boundary layer. This will not only enhance our understanding of the underlying physics of the boundary layer, but also aid in the development of an effective active control technique for improving the performance of aerodynamic profiles.

3. Objective and outline of the thesis

The main objective of this thesis was to investigate the impact of acoustic excitation on the laminar separation bubble. Through the use of advanced measurement techniques and data post processing, this study aims to provide a detailed understanding of the physical processes involved in the interaction between acoustics and the separated shear layer, and to explain how these interactions can be used to control or manipulate the transition process.

In this dissertation, an attempt was made to get closer to the conditions present in an aircraft engine flow system by using pink noise at SPL equal to 125 and 135 dB, which have not been reached experimentally, two Reynolds numbers i.e. 185 000 and 370 000 were considered. In addition, for comparison, a mono–harmonic signal with forcing of 125 dB was used for a one-given Reynolds number.

One of the aims was then to cross–examine these cases and elucidate underlying physical mechanisms responsible for the process of instability and flow breakdown in the separated shear layer. In addition the effect of acoustics on characteristic phases of the laminar separation bubble, such as, separation onset, the triggering of laminar-turbulent transition process, reattachment point was described. Another aspect of this research was the design and optimization of the acoustic excitation system. This involved selecting the appropriate frequency range and amplitude of the acoustic wave level, the design concept of acoustic system as well as the appropriate location and orientation of the speakers.

The specific research questions that this thesis will address include:

- What is the influence of Reynolds number on separated shear layer phenomena?
- How does the acoustic excitation impact the important stages of separated shear layer development, i.e. the separation onset, laminar-turbulent onset, LSB thickness, reattachment point, and integral boundary layer parameters?

- How do the frequency and amplitude of the acoustic wave affect the flow statistics of the separated boundary layer?
- What physical phenomena are responsible for the turbulence breakdown in the LSB and how the acoustic excitation modifies the process?

In order to achieve these research objectives, extensive experimental studies have been planned, using mainly the constant temperature anemometry (CTA). Investigation were conducted with the use a wind tunnel and a specialized test section that has been designed to mimic the conditions of the separation of boundary layer. The test section allows to observe the flow characteristics of the system in real-time and measure the performance of the acoustic excitation system. The research was carried out as part of project No. 2018/31/B/ST8/01717 supported by National Science Centre, in collaboration with the Warsaw University of Technology. One of the tasks of the Czestochowa University of Technology was to provide data to validate the numerical modelling methods being developed by the partner research group. The results of the research using the experimental data were submitted for publication in Kubacki et al., (2023).

The results of this research can have a wide range of applications in the field of fluid dynamics. The findings will be of particular interest to engineers and scientists who are working on the design and optimization of industrial systems, such as aircraft, automobiles, ships, and wind turbines. Additionally, the results of this research will be of interest to researchers in the field of acoustics, as they will provide insights into the fundamental physics of the interaction between an acoustic wave and a fluid. Ultimately, this research will help to pave the way for the development of new and more efficient technologies that can be used to improve performance and reduce the environmental impact of a wide range of industrial systems.

4. Description of the experimental set–up

4.1. Wind tunnel

The experimental studies presented in this dissertation were conducted using a subsonic open-circuit wind tunnel located at the Department of Thermal Machines at Częstochowa University of Technology. A diagram of the test stand is shown Figure 4.1. The source of wind for the tunnel is a centrifugal fan with a capacity 19 000 m³/h, driven by a DC motor. At the inlet of the fan system, a fabric filter has been implemented to purify the air before entering the measurement section. This procedure is essential for obtaining undisturbed results during hot-wire anemometry measurements.

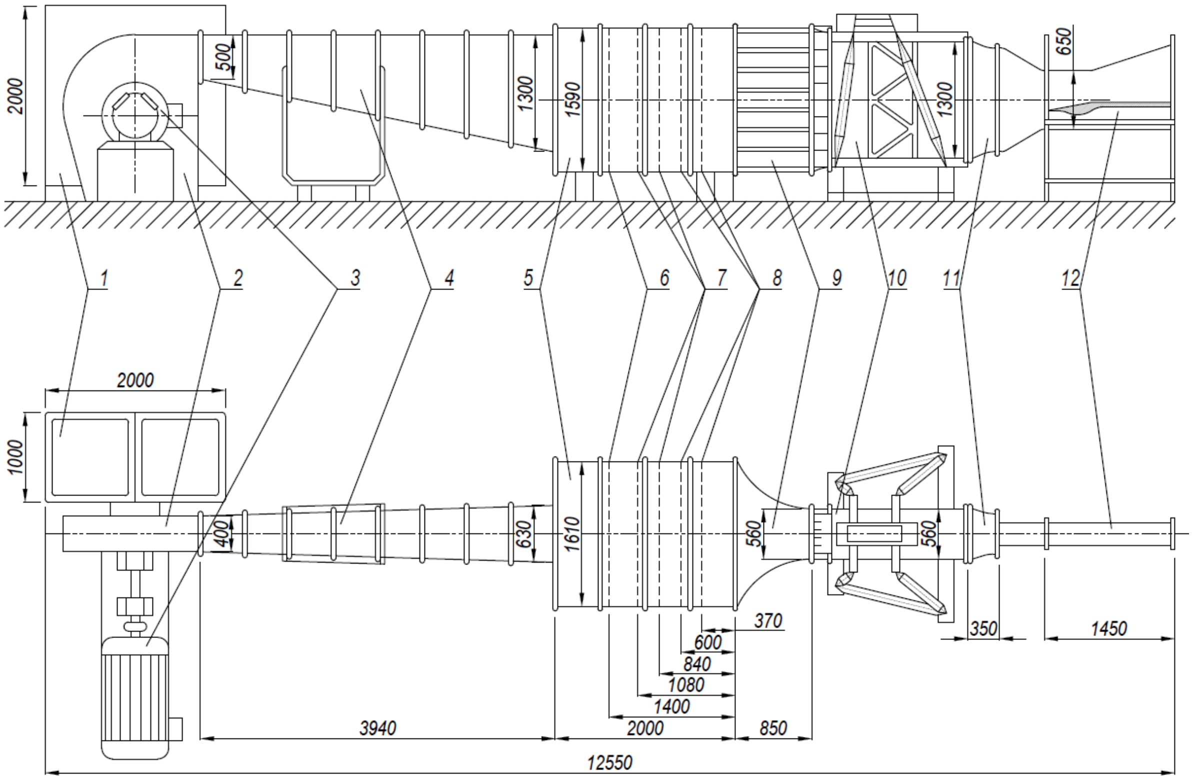

Figure 4.1 Wind tunnel diagram: 1 – fabric filter, 2 – fan, 3 – DC motor, 4 – diffuser, 5 – settling chamber, 6 – grid 0.8×0.8, 7 – grid 1×1, 8 – grid 2×2, 9 – contraction channel, 10 – intermediate channel, 11 – second contraction channel, 12 – test section

The air from the fan is directed through a diffuser that increases the cross-sectional area of the airflow, and then into a settling chamber. The settling chamber is equipped with a series of meshes that are designed to homogenise the velocity profile and decrease the turbulence intensity. The settling chamber is followed by a contracion nozle that changes the direction of the airflow and leads to an intermediate channel. The intermediate channel is equipped with grid and two additional contraction channels that further homogenise airflow and lead to a straight outlet channel with a cross–sectional area of 250 mm x 720 mm. This allowed for a low level of inlet turbulence intensity (Eq. 1) of Tu = 0.8% for test case 5 m/s and Tu = 1.2% for case 10 m/s case, which is necessary to provide a cleaner environment that magnifies the effects of the acoustic excitation.

Equation of turbulent intensity:

$$Tu = \frac{u'}{U_{e\_in}} \qquad \textit{(Eq. 1)}$$

The experimental setup was designed to provide a controlled environment with minimal disturbances, this is essential for accurate measurement of the effect of acoustic excitation on the flow separation. The wind tunnel, which was effectively showcased, offers a consistent and steady airflow within the inlet section, with the capacity to achieve varying wind speeds ranging from a standstill at 0 meters per second, all the way up to a maximum velocity of 50 meters per second.

4.2. Test section

There are many types of experimental test section configurations. One of the features of the test section is to preserve the symmetry of the flow. The choice of symmetric or asymmetric test section configuration was initially considered for the investigation. Both configurations have been observed in various studies and have their own advantages (Funazaki & Kato, 2002; Gostelow & Thomas, 2006; Howell, 1999; Stieger, 2002). The symmetric configuration allows for duplicate measurements on both sides of the testing object and ease of achieving zero incidence inflow, while the asymmetric configuration simplifies construction as it does not require duplication of the wall shape. Finally, for the present investigation of the separation bubble in the laminar boundary layer, it was decided to use asymmetric type. A similar shape of the wind tunnel was used in previous investigations conducted at the

Department of Thermal Machinery of Czestochowa University of Technology (Dróżdż & Elsner, 2011; Dróżdż & Elsner, 2013, 2014; Materny et al., 2008).

The test section (Figure 4.2) was specifically engineered to simulate the pressure coefficient C_p (Eq. 2) distribution present in the axial compressor blading, as illustrated in Figure 4.3. This was achieved through the implementation of a geometric design that generates an APG from a location approximately 382.5 mm downstream from the leading edge, after throat of the measuring channel. Subsequent to the contraction end, the outlet gap was located below the flat plate with the aim of obtaining a fresh build-up of boundary layer on the flat plate. The pressure distributions C_p presented in Figure 4.3 were measured at a constant distance from the bottom wall equal $y = 100$ mm along the flat plate.

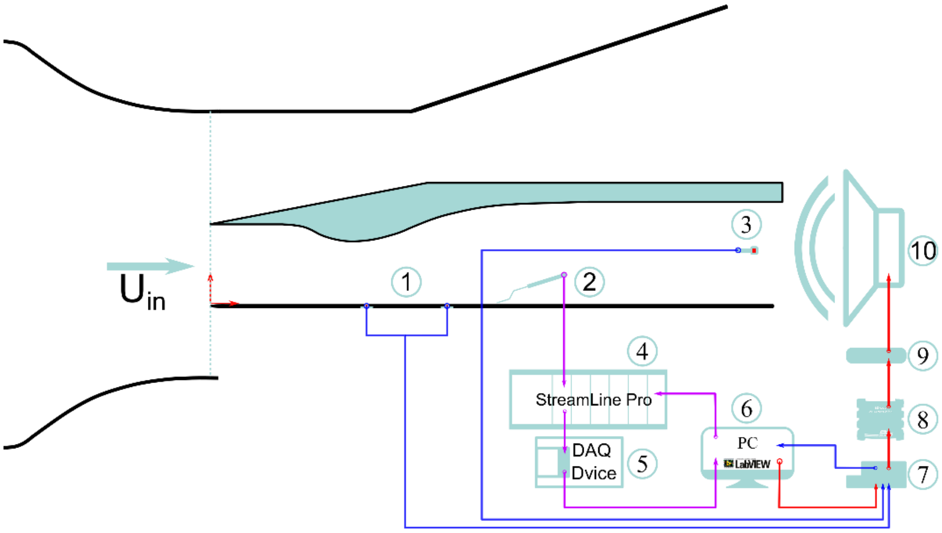

Figure 4.2 Diagram of the test section: 1) two flush-mount microphones, 2) single hot-wire probe, 3) free-stream microphone, 4) HWA system, 5) data acquisition device NI – 6356, 6) personal computer, 7) data acquisition device cDAQ – 9185, 8) direct injection box, 9) audio amplifier, 10) acoustic generator

$$C_p(x) = \frac{P_s(x) - P_{s_{in}}}{P_{tot} - P_{s_{in}}} \qquad \text{(Eq. 2)}$$

The pressure distribution indicates acceleration in the favourable pressure gradient (FPG) region and deceleration in the APG region due to the decrease and an increase in cross-sectional area, respectively. The difference in static pressure values, especially seen in the location of the throat, between cases 5 and 10 m/s can be explained by different conditions at the inlet of the test section as well as the flow blockage caused by the outlet of the speaker at the test section. The measurements were conducted over a 1450 mm long and 250 mm wide plexiglass flat plate, with an elliptical leading edge. The flat plate was inclined at an angle of 1 degree with respect to the flow direction, to generate a stable (without separation at the leading edge) Blasius boundary layer. This configuration allowed for the investigation of flow physics in the near-wall region and provided information on the development of the boundary layer, including displacement thickness and momentum thickness. Furthermore, measurements were conducted, at various Reynolds numbers, on the development of the boundary layer.

In order to prevent the occurrence of separation bubbles at the upper wall in the inlet, a tripping wire was installed. The trip wire made from steel has 1.5 mm in diameter. The wire was designed to trigger a faster transition to turbulent boundary layer of the incoming flow, which helps to maintain the attached flow state and thus prevents the formation of separation bubbles on the upper curvature.

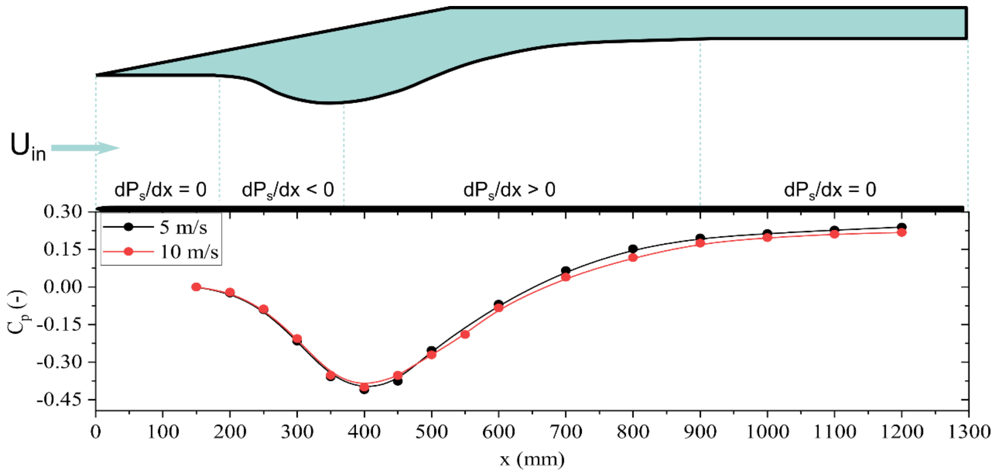

Figure 4.3 Pressure distribution inside the test section for both investigated cases, at the distance y = 100 mm from the flat plate

In order to facilitate the control and measurement of the drive system, a traverse system was installed externally to the measurement chamber. The control axis *x* uses a step motor that is coupled to linear actuators utilising a belt drive system for control, while the y axis employs a step motor that is coupled to a worm gear mechanism utilising. A programmable 4-axis trajectory controller, WObit MIC488, was used to drive the step motors in the system. The system allows for the measurement of velocity at any point within the test chamber symmetry plane, with a precision of probe positioning 0.01 mm in the *y* direction and 0.0385 mm in *x* direction.

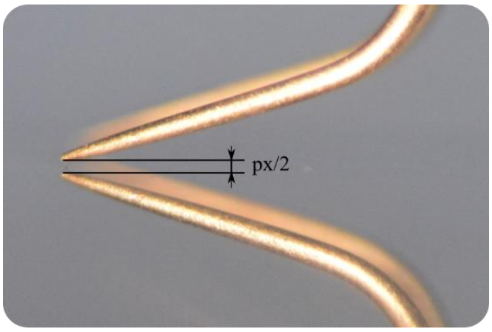

Figure 4.4 Macro photo of hot-wire probe

To determine the distance of the hot-wire probe from the wall with high accuracy, a photographic technique was employed. The transparent side walls of the test section allowed for the use of a NIKON digital camera D5200 and a set of macro lenses Tamron AF 180mm / 3,5 SP Di Macro to take a photo through the wall and to determine the probe's distance from the flat plate. Due to the fact that the flat plate reflects the tips of the hot-wire on the surface, it is possible to move the probe next to the surface of the plate without damaging it. When the probe picture is taken (Figure 4.4), the number of pixels between the tips of the probe and their reflection on the flat plate can be counted. Half the number of pixels determines the probe to wall distance. To scale this distance a millimetre reference image was also taken, which allows to convert pixels to millimetres. The resulting resolution was approximately 263 px = 1 mm, yielding a positioning accuracy similar to precision of the probe positioning (0.01) mm (assuming that the wire is located in the centre of the tips of prongs and parallel to the wall).

The construction of the traverse system and test section enable hot-wire measurements within the range of *x* = -100 mm to 900 mm, with a vertical measurement limit defined by the height of the upper wall. Table 4.1 presents the data of all recorded profiles, including all types of sound excitation employed during the experiments. Distinct excitation conditions were examined in the study, including non-excitation (NE), pink noise (PN), and sinusoidal noise (Sin). The noise was generated at two sound pressure levels: 125 dB and 135 dB.

Table 4.1 Location of the analysed planes using a single probe along with the type of generated noise

U_{in} (m/s)	*x* coordinates (mm)	Rage of *y* coordinates (mm)	Type of excitation			
			NE 89 dB	PN 125 dB	PN 135 dB	Sin 125 dB
5	70	0–60	✓	✓	✓	x
	200	0–50	✓	✓	✓	x
	300	0–90	✓	✓	✓	x
	400	0–140	✓	✓	✓	x
	500	0–140	✓	✓	✓	x
	525	0–140	✓	✓	✓	x
	550	0–140	✓	✓	✓	x
	575	0–140	✓	✓	✓	x
	600	0–150	✓	✓	✓	x
	625	0–150	✓	✓	✓	x
	650	0–140	✓	✓	✓	x
	675	0–140	✓	✓	✓	x
	700	0–140	✓	✓	✓	x
	800	0–140	✓	✓	✓	x
	900	0–130	✓	x	✓	x
10	300	0–60	✓	✓	✓	✓
	400	0–120	✓	✓	✓	✓
	500	0–120	✓	✓	✓	✓
	525	0–140	✓	✓	✓	✓
	550	0–140	✓	✓	✓	✓
	575	0–140	✓	✓	✓	✓
	600	0–150	✓	✓	✓	✓
	625	0–150	✓	✓	✓	✓
	650	0–140	✓	✓	✓	✓

4.3. Acoustic excitation generator

The primary objective of the study was to analyse the effect of acoustic forcing on the development of a shear layer above the separation bubble. As stated earlier, it was assumed that the study would be conducted for a wide range of acoustic power up to 135 dB, which for broadband excitation has not been tested so far according to the contemporary literature. For this purpose, it was necessary to design and manufacture a suitable acoustic system. The task of the thesis was to develop a design concept, while the technical design and manufacture was outsourced to the professional POL-AUDIO company. This system consists of three loudspeakers with different frequency ranges, a professional power amplifier, direct injection (DI) box and a signal generator.

Great demands were placed on the performance of the loudspeakers. Due to the specific geometric requirements of the housing (outlet: 650 *x* 250 mm) and the need to maintain a maximum continuous SPL across the frequency band of at least 130dB, and with short-term measurements (less than one minute) SPL of 135 dB, a multi-stage optimization of the internal geometry of the speaker was necessary. The first loudspeaker, a low-frequency woofer, operates in the range of 40 Hz to 130 Hz. The second loudspeaker, a middle frequency generator, operates within the range of 100 Hz to 650 Hz. The third loudspeaker, a middle – high frequency generator, operates within the range of 0.5 kHz to 20 kHz. The frequency range of each generator overlaps with that of the other generators, enabling stable and controllable sound production over the broad range of 0.04 to 20 kHz.

Due to the dominant frequencies identified in the separated boundary layer, two speakers low-frequency woofer and middle-high frequency generator were used in preliminary studies. Finally, in the main studies included in the dissertation, only the middle-high frequency generator, which employs a 15 – inch one-way speaker (T115 – 800) with a frequency response of 100 – 500 Hz ± 3dB was used. The impedance of the speaker is 8 Ohm, and the peak power is 800 W. The loudspeaker is capable of producing noise (both tonal and broadband) with the desired amplitude and frequency, and maintaining a stable level of noise excitation over an extended period of time

(~ 60 minutes). This is necessary for the acquisition of data under stable conditions of noise excitation. Figure 4.5b shows the power spectral density (PSD) recorded at the speaker outlet during pink noise generation for two SPLs. The black line corresponds to the background acoustic signal recorded with the wind tunnel in operation. As can be observed, the amplified frequency is in the range of speaker characteristics. The speaker was placed at a certain distance from the outlet of the wind tunnel and orientated to point upstream the flow, as depicted in Figure 4.2. This position was chosen to ensure that the speaker did not interfere with the flow within the measurement area. To ensure stable flow and acoustic conditions the position of the loudspeaker was fixed and not adjustable during the course of the experiment.

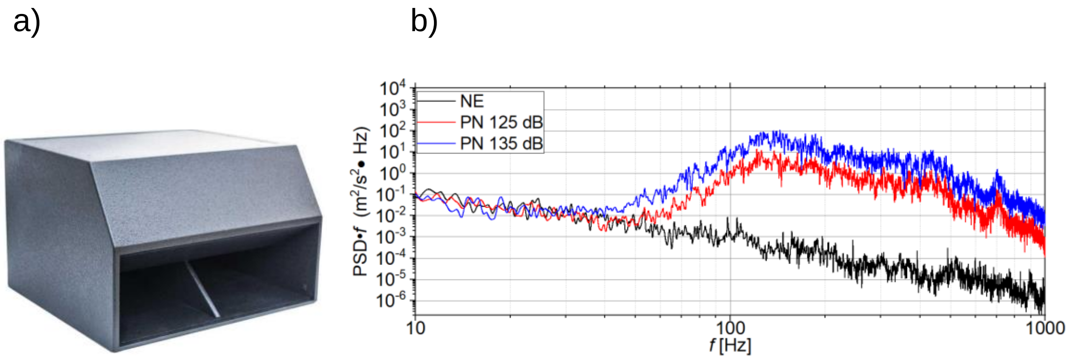

Figure 4.5 Acoustic generator loudspeaker (a) PSD of generated pink noise (b)

The speaker was connected to the Powersoft K10 DSP, a professional-grade power amplifier that is engineered for use in a variety of applications, including live shows. The K10 DSP is equipped with a powerful DSP (Digital Signal Processor) that enables advanced control and processing of the audio signal, including: filtering, equalisation, and limiting. Additionally, the K10 DSP features advanced protection functions that safeguard the amplifier and speakers from damage caused by overloading, short-circuits, and thermal overload. The K10 SDP can be controlled and monitored via an Ethernet connection, allowing remote control and monitoring of the amplifier's status and performance, thus ensuring optimal performance during the experiment.

The amplifier was controlled by the National Instruments NI – 9263 module (Figure 4.6). It is a high-performance analogue output module that can at the same time update multiple channels at a rate of 100 kS/s/ch. It is designed with various protective features such as overvoltage protection, short-circuit protection, and low crosstalk, ensuring the safety of the device and the system. Rate and high relative accuracy, making it suitable for applications that require precise signal output. The module is also NIST traceable calibrated and has a double isolation barrier between the channels and the earth ground for improved noise immunity. Each channel of the module is equipped with a digital-to-analogue converter (DAC) that generates a voltage signal as its output.

Figure 4.6 NI - 9263 module

The signal to NI – 9263 was sent by a programme developed within the environment of a visual programming language, LabVIEW, from National Instruments. The program enabled the generation of signals across a wide frequency range, with variable amplitudes and various types of noise including tonal and broadband noise, thus providing a high degree of flexibility in terms of signal generation for the experiment.

Between amplifier K10 DSP and output module NI – 9263 (DI) the BSS AR – 133 DI box (see Figure 4.7) was installed. The box fulfils multiple functions, including signal conversion to a balanced signal. Many audio sources, such as converters, output unbalanced signals, which can be susceptible to radio wave noise and interference when transmitted over long, multi – strand cables between the generator and the loudspeaker. By converting these signals to a balanced format, the AR – 133 can help to reduce interference and ensure a clear and consistent audio signal.

Figure 4.7 The BSS AR - 133 DI box

In addition to signal conversion, the AR – 133 also performs impedance corrections. Impedance is a measure of opposition to the flow of electric current in a circuit, and different devices and components can have different impedance levels. The AR – 133 is designed to provide a high-impedance input that can be used with a variety of sources, and it also has a low-impedance output that can be used to connect to professional audio equipment such as amplifiers. Overall, the BSS AR – 133 is a versatile direct injection box that can help to ensure high-quality audio signals in a range of professional audio applications.

4.4. Measuring Equipment

The velocity measurements inside the test section were performed using a hot-wire anemometry (HWA) technique, specifically the Dantec Dynamics Streamline Pro apparatus utilising a single gold-plated hot-wire probe. The StreamLine Pro CTA system is a high performance data acquisition system manufactured by Dantec Dynamics. The Constant Temperature Anemometer (CTA) is a widely accepted method for measuring fluid flow velocities in both gaseous and liquid flows. It utilizes the principle of King's law (Eq. 3) and the rate of cooling of small heated sensors placed in the flow.

$$E^2 = E_0^2 + BU^n \qquad \text{(Eq. 3)}$$

The sensor is one arm of a Wheatstone bridge-circuit, in which the temperature is kept constant. The output voltage from the anemometer is digitised and then converted to velocity using probe calibration.

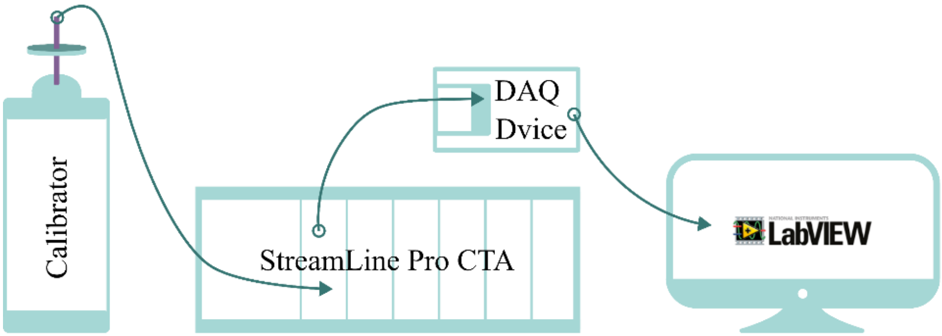

Figure 4.8 Diagram of calibrating system

Accurate measurements using CTA technology require calibration of the sensor. The StreamLine Pro Automatic Calibrator offers in-situ air velocity calibration to ensure high precision, especially for the low velocities (below 1.5 m/s) that were the case of measurements preformed during this thesis. This calibrator (Figure 4.8) is designed for the calibration of hot-wire probes in air at velocities ranging from a few cm/s to over 300 m/s. The probe is positioned in a free jet with a flat, low-turbulence velocity profile during the calibration process. The calibrator is controlled through the StreamWare Pro software.

A gold-plated boundary layer HWA boundary-layer-type 55P05 probe (Figure 4.4) with a sensing length of 1.25mm and a diameter of 5μm, was used in the study. To minimize flow perturbations, the probe was inserted into the test section from behind the separation region. To avoid disconnection between hot-wire probe and CTA system, the calibration of the hot-wire probe using Dantec’s calibrator unit was performed in-situ through the hole in the flat plate designed for insertion of the calibrator nozzle. Data acquisition was performed at a sampling frequency of 5 kHz and a sampling time of 40 seconds. Temperature variations during the measurement of a single velocity profile were kept within ±0.2 °C. When the temperature in the wind tunnel deviated from the calibration temperature, a temperature-based voltage correction was automatically applied. The measurements were performed with a high degree of accuracy, the free-stream velocity and static pressure at the inlet plane ($x = 0$) were monitored with uncertainties of 1% and 10% respectively.

Figure 4.9 NI - 6356 module

The data obtained from the CTA system was transmitted to the NI – 6356 module (Figure 4.9), a high-performance data acquisition module manufactured by National Instruments. It is designed to be ability to acquire up to 8 analog input channels at a sampling rate of 1.25 MS/s per channel. The module also has the flexibility to support various types of inputs such as single-ended and differential, thus providing a wide range of measurement options.

Figure 4.10 GRAS 46BE 1/4" CCP Free - field

Advanced sound field measurements were conducted utilizing a GRAS microphones system. The system comprises of both flush-mounted and free-field microphones, which are connected to a National Instruments analog-digital amplifier (NI – 9232) (see Figure 4.12). This amplifier is then connected to a modular data acquisition system (cDAQ – 9185).

The data acquisition and post-processing are performed using an in – house developed LabVIEW software. During the measurement, the GRAS 46BE 1/4" CCP Free-field microphone (Figure 4.10) was placed at the outlet of the test section to measure the SPL generated by the speaker. Two GRAS 47BX 1/4" CCP (Figure 4.11) flush mount microphones were strategically positioned on the flat plate, located at a distance of 400 mm and 600 mm from the leading edge. These microphones were utilized to determine the dominant frequency of the flow, measure the natural SPL of the flow, and monitor the SPL generated by the noise generator. The flush-mounted design of the microphones allows for minimal disturbance of the flow, ensuring accurate measurements of the flow characteristics in the boundary layer. The system has an accuracy range of 20 Hz to 20 KHz, with an uncertainty of ±0.1 dB in the measured SPLs, which is within the typical range of such measuring devices.

Figure 4.11 GRAS 47BX 1/4" CCP flush mount

Figure 4.12 NI-9232 module

The NI – 9232 (Figure 4.12) is a high performance data acquisition module manufactured by National Instruments. It is a multichannel device that can acquire up to 3 analogue input channels, with a sampling rate of up to 250 kS/s per channel. It also has an option for different types of input, such as differential, single- ended and thermocouple input, RTD, and thermistor. The NI – 9232 is designed for use in industrial, research, and laboratory environments. It is a high-performance device that can be used for a wide range of data acquisition applications, such as temperature, voltage, and frequency measurements.The cDAQ – 9185 (see Figure 4.13) is a modular data acquisition system manufactured by National Instruments. It is part of the CompactDAQ platform, designed for use in various industrial,

Figure 4.13 cDAQ – 9185 module

research, and laboratory environments. This device has a variety of features including: support for multiple analogue and digital I/O modules; ability to be controlled through USB, Ethernet, or wireless interfaces; compatibility with a range of software, including LabVIEW and MATLAB; support for advanced triggering and synchronization capabilities-several isolation options to protect against voltage and current transients. It supports a wide range of data acquisition applications, such as temperature, voltage, and frequency measurements designed for harsh industrial and mobile environments, with a wide operating temperature range and rugged metal enclosure. It is a versatile device that can be used for a wide range of data acquisition applications, such as temperature, voltage, and frequency measurements, and it is designed to withstand harsh industrial and mobile environments including high SPLs.

Analysis of the boundary layer parameters was performed using a spreadsheet in the Excel software, which facilitated the calculation of parameters such as pressure coefficient, shape factor, friction velocity, boundary layer thickness, displacement thickness, momentum thickness and others.

In order to properly post process the measurement signals scripts to calculate power spectra and intermittency were developed in the high-level programming language Python. These scripts enabled efficient computation and visualisation of spectral graphs. Libraries such as Pandas, NumPy, SciPy, and Matplotlib were utilized in the creation of the spectra. The scripts are included in Appendix 1.

4.5. Definition and selection of inlet conditions

The selection of appropriate Reynolds numbers is crucial in the study of boundary layer separation. In this study, it was decided to perform the experimental research for two inlet velocities i.e. U_{in} = 5 and 10 m/s, which correspond to Reynolds numbers 185 000 and 370 000. The Reynolds number is defined based on the length of the flat plate from the leading edge to the point of separation onset and the free-stream velocity at that location. The choice of the Reynolds numbers was dictated by the range of velocities achievable in the wind tunnel on one hand and the desired conditions in the APG area on the other.

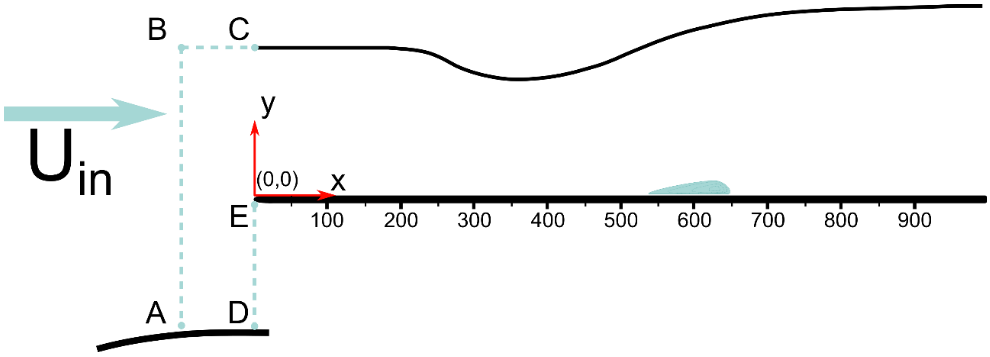

Figure 4.14 Location of inlet traverses

In such studies, it is always crucial to establish and maintain stable inlet conditions. Figure 4.14 presents the location of planes where flow conditions were determined using hot-wire anemometry (HWA), utilizing an X-wire probe, while Table 4.1shows the coordinates of those planes.

Table 4.2 Location of the analysed planes using an X-wire probe along with the type of generated noise

U_{in} (m/s)	*x* coordinates (mm)	*y* coordinates (mm)	Type of excitation
5	-100	-212 – 200	NE
	-100 – (-20)	200	NE
	0	-212 – (-10)	NE
10	-100	-212 – 200	NE
	-100 – (-20)	200	NE
	0	-212 – (-10)	NE

The locations of the velocity measurement points, referred to as traverses, were carefully selected to accurately determine the mean velocity vectors in the flow prior to entering the test section to further use for numerical simulation purpose.

Table 4.3 The coordinates of the A, B, C, D, and E points

Point	A	B	C	D	E
(*x*;y) coordinates	(-100; -212)	(-100; 200)	(-100; -20)	(-212; 0)	(-10; 0)

The traverse A – B, located 100 mm from the leading edge and perpendicular to the flat plate, covers the full width of the flow from the inlet to the upper plate. The traverse B – C, placed along the flow at a height of 200 mm from the flat plate, provides information on the flow direction in the plane of the upper wall. The traverse D – E, perpendicular to the flow and covering the outlet from the lower slot, describes the velocity vectors beneath the flat plate. The coordinates of the A, B, C, D, and E points are presented in Table 4.3, with reference to the zero point of the coordinate system shown in Figure 4.2 and located above the leading edge.

The mean velocity and root mean square *u'* values obtained in cross sections A – B for flow velocities of 5 m/s and 10 m/s were analysed. The flow inlet conditions to the wind tunnel A – B for both cases (see Figure 4.15) were characterized by a stable and unchanged velocity component *U* and *V* oriented according to the plane of the flat plate, as well as a constant distribution of velocity fluctuations components. The analysis revealed that the *U* component remained unchanged until it approached the surface of the outlet nozzle located below the flat plate, where its significant decrease in value occurs. On the other hand, the *V* component exhibited a slight increase as the x-wire probe moved away from the plane of the flat plate, which is an expected behaviour as the significant amount of flow escapes through the lower gap and above the upper plate. Figure 4.16 presents the velocity component distributions along traverse B – C for both inlet velocities. The graphs show a consistent trend of velocity distribution, with relatively constant values of the *U* and *V* components over the entire distance. However, a slight decrease in the *U* component and an increase in the negative value of V component can be observed in the vicinity of the leading edge of the upper wall. This is a result of inclined coordinate system (inclined flat plate) in respect to the inlet flow.

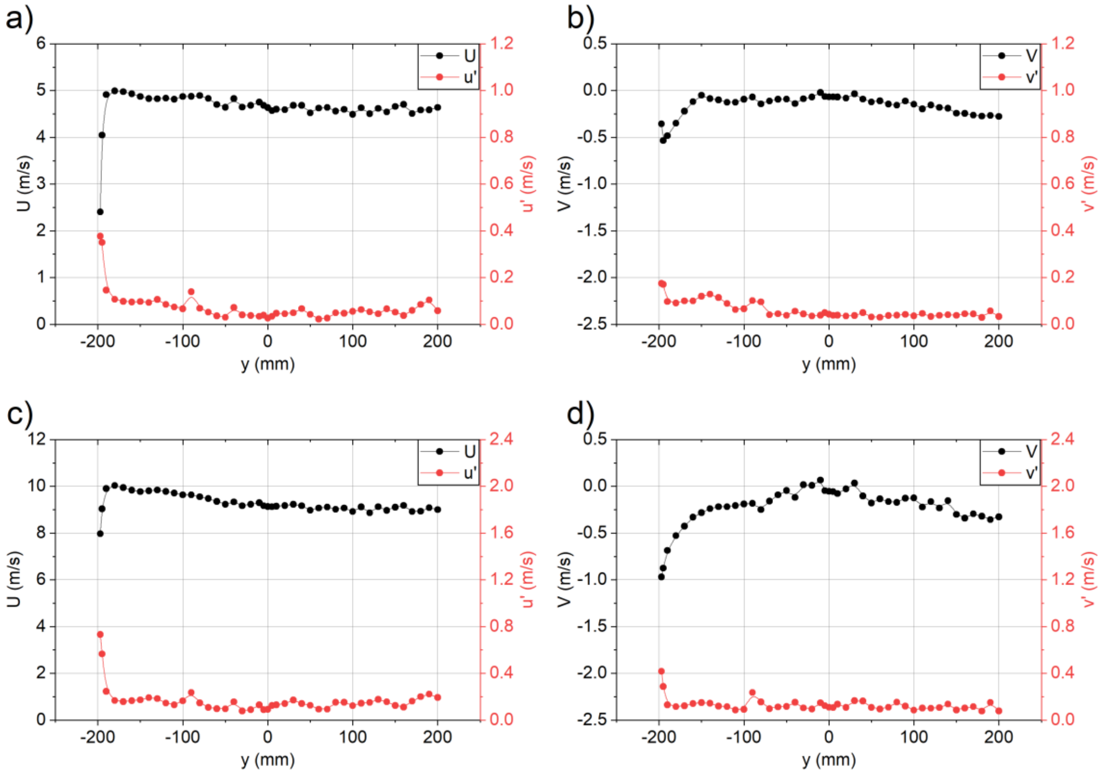

Figure 4.15 A – B traverses, velocity component U and u’ for 5 m/s case (a), velocity component V and v’ for 5 m/s case (b) velocity component U and u’ for 10 m/s case (c) velocity component V and v’ for 10 m/s case (d).

Figure 4.17 displays the results of the measurements recorded at the traverse D – E, which is positioned in the lower gap located below the leading edge and perpendicular to the flow. It can be seen that, in the vicinity of the surface of the nozzle exit, there is a significant change in the velocity vector components, *U* and V.

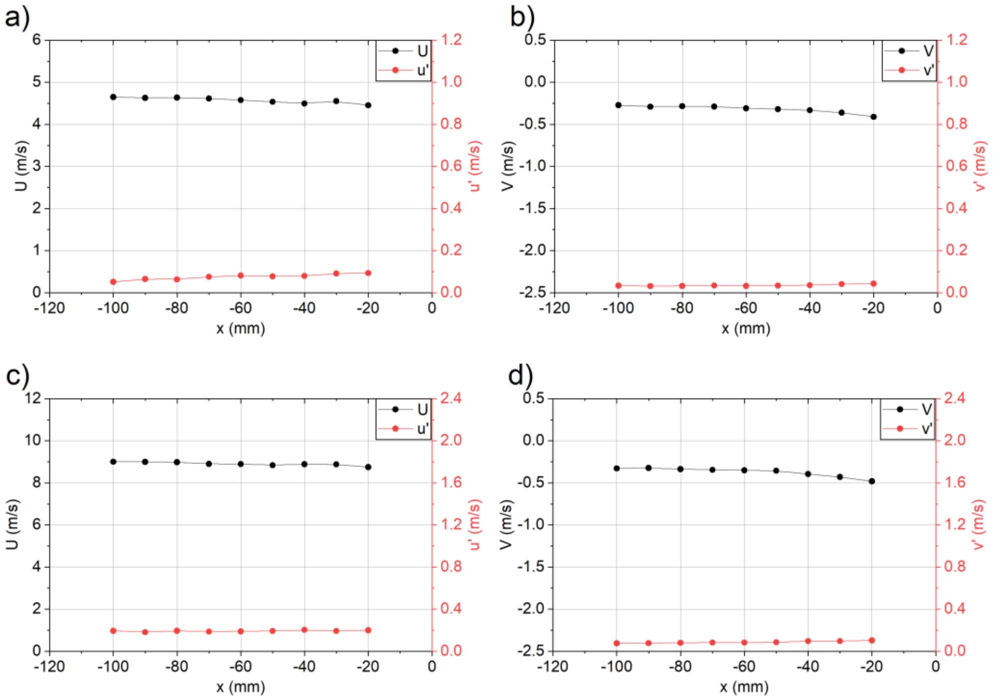

Figure 4.16 B – C traverses, velocity component U and u’ for 5 m/s case (a), velocity component V and v’ for 5 m/s case (b) velocity component U and u’ for 10 m/s case (c) velocity component V and v’ for 10 m/s case (d).

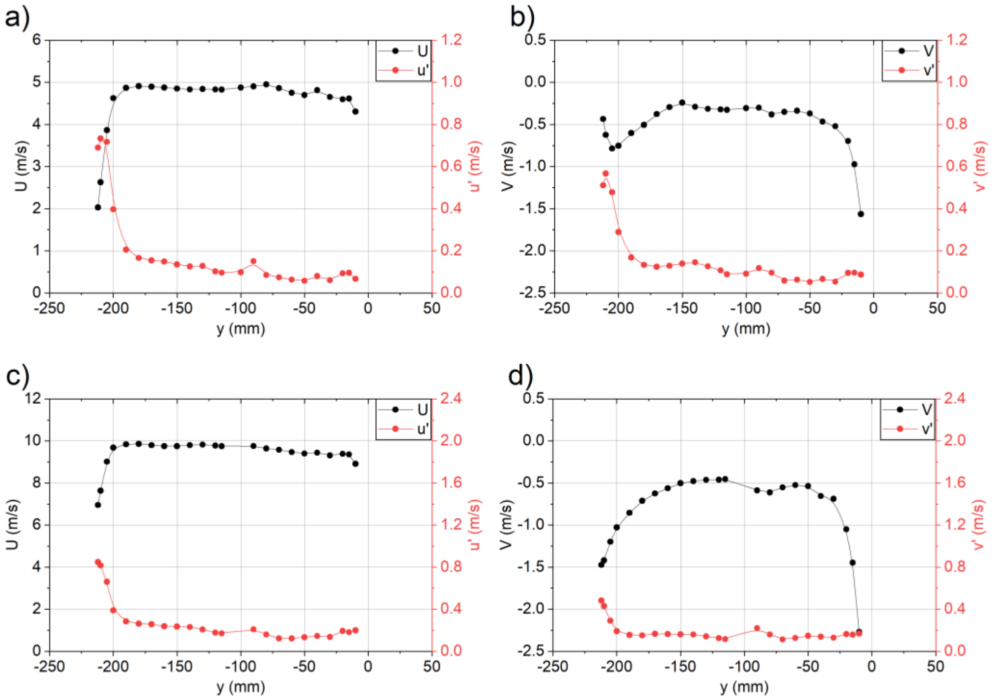

Figure 4.17 D – E traverses, velocity component U and u’ for 5 m/s case (a), velocity component V and v’ for 5 m/s case (b) velocity component U and u’ for 10 m/s case (c) velocity component V and v’ for 10 m/s case (d).

Turbulence intensity and length scales are important parameters used to describe the fluctuating behaviour of fluid flows. The integral length scale defines the spatial dimension of turbulence structures and represents the average size of the largest eddies. On the other hand, the Taylor micro length scale represents the average size of the smallest eddies in the flow. To calculate the integral and Taylor micro length scales, the method was proposed by Roach (1987). Having the autocorrelation function:

$$R_{11}(\tau) = \frac{u(t)u(t+\tau)}{(u')^2} \qquad \textit{(Eq. 4)}$$

a Taylor microscale can be defined as:

$$\tau_{11} = \sqrt{2}\left[-\left(\frac{\partial^2 R_{11}}{\partial \tau^2}\right)_{\tau=0}\right]^{-1/2} \qquad \textit{(Eq. 5)}$$

while time macroscale is:

$$T_{11} = \int_0^\infty R_{11}(\tau)d\tau \qquad \textit{(Eq. 6)}$$

One way to estimate the spatial scales of turbulence is through the use of the Taylor hypothesis, which suggests that the turbulence structure appears to be frozen in time. This allows us to relate spatial scales to time scales. Specifically, assuming that vortices propagate with an average velocity, we can calculate the spatial Taylor microscale

$$\lambda_{11} = U_1 \tau_{11} \qquad \textit{(Eq. 7)}$$

and integral length scale Λ_{11}:

$$\Lambda_{11} = U_1 T \qquad \textit{(Eq. 8)}$$

where U_1 is the streamwise velocity, in direction x.

Autocorrelation functions R_{11} of the streamwise u(t) for the defined planes at the inlet were shown in Figure 4.18. The function R_{11} decays slowly with correlation lag τ. It can be observed that depending on the measurement plane, the shape of the function varies slightly. However, it is important to note that in the freestream the length scales are consistent and can be assumed the average value of length scales on level 0.009 m and 0.015 m for micro and integral length scales, respectively.

Table 4.4 Micro and integral length scales of inlet flow

Case (m/s)	traverses	micro length scales λ_{11} (m)	integral length scales Λ_{11} (m)
5	A – B	0.0097	0.0173
	B – C	0.0097	0.0135
	D – E	0.0080	0.0161
10	A – B	0.0092	0.0173
	B – C	0.0088	0.0162
	D – E	0.0063	0.0135

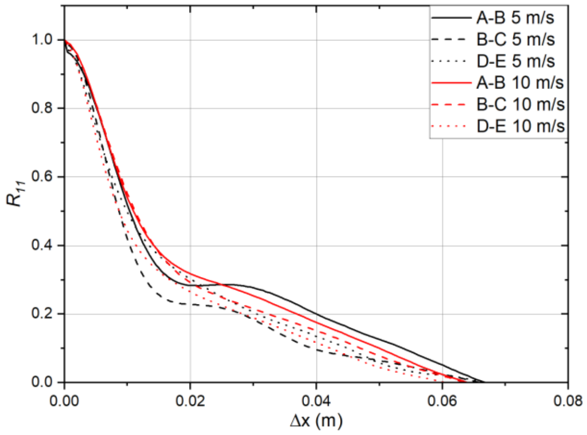

Figure 4.18 Autocorrelation functions.

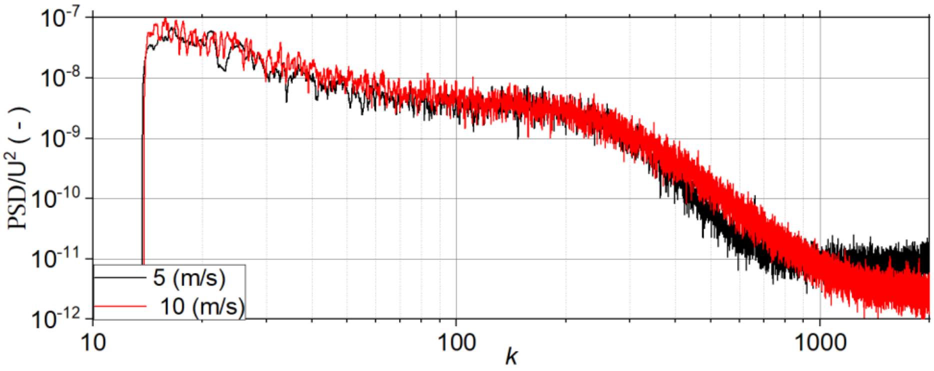

Figure 4.19 Power spectrum density of velocity signal in the freestream($k = 2\pi * f/U$)

As can be observed in Figure 4.19 the PSD scaled with free stream velocity (5 and 10 m/s) as a function of wavenumber $k = 2\pi * f/U$ is similar for both cases. It confirms the same flow characteristics and structures in terms of the energy content across the range of Reynolds numbers studied.

5. Acoustic excitation

5.1. Characteristics of the acoustic field in the test section

As stated in Chapter 2, whether numerical (Suzuki & Ishii, 2001) or experimental (Bernardini et al., 2012; Ol et al., 2005), most studies that investigate stability in the laminar separated shear layer involve artificial forcing of the boundary layer with known sinusoidal and periodic perturbations of at the most unstable frequency of the separated shear layer observed in the natural flow (Yarusevych et al., 2007; Yarusevych & Kotsonis, 2017). The choice of the frequency is based on the observation that the instabilities leading to the l-t transition lock on to the excitation frequency (Yarusevych & Kotsonis, 2017). On the other hand Kurelek et al., (2018) have shown, that this impact can modify the extent of LSB and also alter the flow stability characteristics. They also stated that, band forcing may be more effective because the frequency tunes to the current local characteristics of the boundary layer. One of the possible advantages of broadband excitation is the possibility of amplification of all relevant frequencies already present in the flow. In this study it was decided to verify this hypothesis assuming that for both Reynolds numbers a broadband acoustic forcing was applied, while for the higher Reynolds, number the harmonic forcing would be applied.

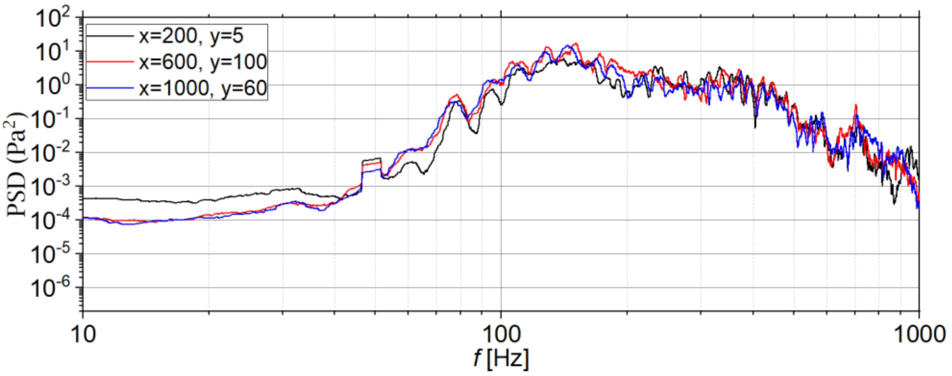

Figure 5.1 PSD of acoustic field

For the acoustic field characterisation, measurements were carried out at several points in the test section using the free–field microphone. As a representative case 10 m/s was chosen with acoustic forcing with pink noise in the range of 100 – 650 Hz at SPL = 135 dB. As can be seen from Figure 5.1

showing the spectra recorded at several points the sound field is homogeneous and no significant changes in both spectral distribution and average sound power are noticed.

To a limited extent, measurements using flush–mount microphones were also used. Measurements were carried out for the test case 10 m/s with a free–field sensor (mic 1) located in front of the loudspeaker and two flush–mount microphones located at distances x = 400 mm (mic 2) and x = 600 mm (mic 3) from the leading edge, respectively. The free–field microphones mounted at the outlet of the measuring section and the flush–mount microphone mounted 400 mm from the leading edge did not detect any dominant frequencies.

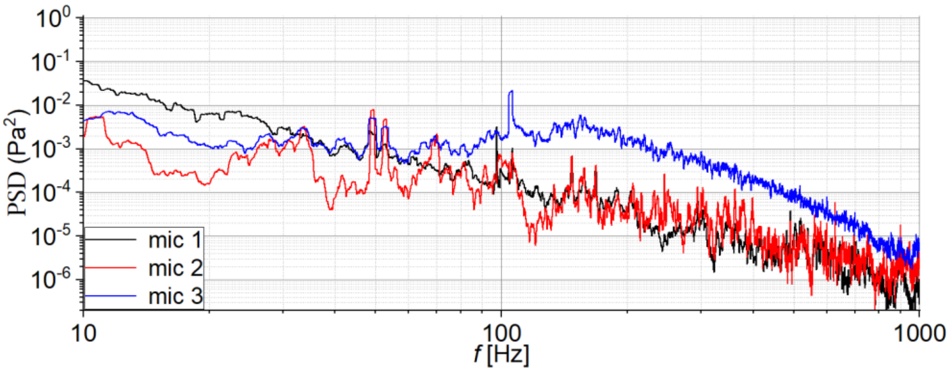

Figure 5.2 PSD of signals recorded by microphones for 10 m/s

However, it can be noted that the second flush–mount microphone located under the separated shear layer (x = 600 mm) showed an increased SPL for $f \gtrsim 80$ Hz. One can also notice a clear peak at f = 110 Hz and a subsequent stretched maximum around 155 Hz. As the 600 mm traverse is located in the separation area, it can be assumed that the dominant frequencies visible on the acoustic spectrum are the result of instability occurring in the separated shear layer. This issue will be discussed in detail in Chapter 7.

5.2. Selection of the tonal excitation frequency for 10 m/s case

For the test case for 10 m/s in addition to broadband forcing of 100 – 650 Hz, tonal forcing was used for comparison. In this subsection, a description of the process of selecting the excitation frequency is provided.

In the first stage, a spectral analysis was carried out based on the signals recorded in the fore part of the boundary layer separation to detect the most unstable frequency observed in the natural flow. Three traverses were selected, i.e. x = 550, 575, 600 mm. For the purposes of this analysis, the spectra were averaged with a window corresponding to a frequency interval of 1.4 Hz.

5.2. Selection of the tonal excitation frequency for 10 m/s caseFigure 5.3 shows that, in the absence of acoustic excitation, several frequency peaks appear. Initially, most of the energy is concentrated around ~110 Hz. Subsequently, the characteristic instability at this frequency is amplified, but secondary instabilities with characteristic frequencies ~130 Hz and ~155 Hz show up. For a traverse of x = 600 mm, the maximum energy is already concentrated around a frequency of ~155 Hz and the process of coherent structures breakdown into smaller scales triggering turbulent flow.

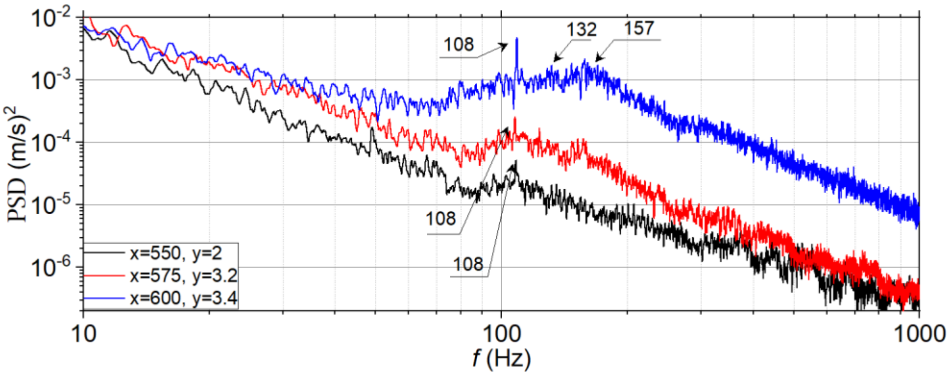

Figure 5.3 PSD of Hot-wire signals from boundary layer region

As a second step, it was decided to test how the boundary layer would respond to tonal forcing in the range of observed naturally induced frequencies. The generated signal was sinusoidal, the excitation was kept constant and equal 125 dB. Single hot-wire probe was placed in a fixed position, x = 575 mm y = 2.4 mm. The forcing frequency was changed in 5 Hz steps from 100 to 190 Hz. By analysing the distribution of velocity fluctuations shown in Figure 5.4, it is possible to observe a varying value of u' depending on the forcing frequency. Three maxima 105, 130, and 155 Hz can be seen, which corresponding quite well to the detected frequencies in the natural flow.

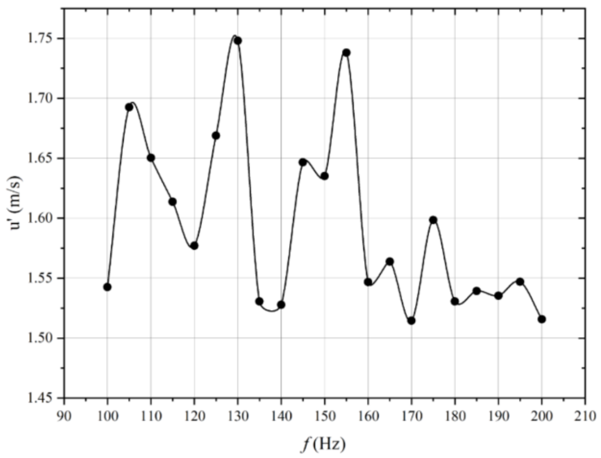

Figure 5.4 Distribution of velocity fluctuations in the function of tonal acoustic excitation

Figure 5.5 shows comparison of recorded spectra related to the NE case, where a clear response of the boundary layer to the forcing can be seen. For 100 Hz only a slight increase is observed. However, for higher frequencies, a strong amplification of energy around the forced frequency is noticeable. These observations confirm that the shedding process of structures (Kelvin-Helmholtz structures as it will be discussed later in Chapter 7) locks on to the excitation frequency. It is interesting that the tonal forcing also strongly amplifies the higher harmonics of the fundamental frequency, which has not been observed in previous studies.

It is also worth to analyse the values of the maximum amplitude of the excited frequency in the responding flow f_h. The diagram (Figure 5.6) shows that, contrary to expectations, even though the excitation always has the same acoustic power (SPL = 125 dB), the values of maximum amplitude of the excited frequency (f_h) are not constant, but show a clear variation as a function of frequency. Three maxima can be seen, corresponding exactly to the frequencies found in the natural BL. This can be related to the observation of (Kurelek et al., 2018) that the strong amplification of the tonally excited instabilities damps on the other hand growth of all other disturbances. In summary, based on the above results the frequency 110 Hz thatappears in the natural flow (NE case) was selected for further study.

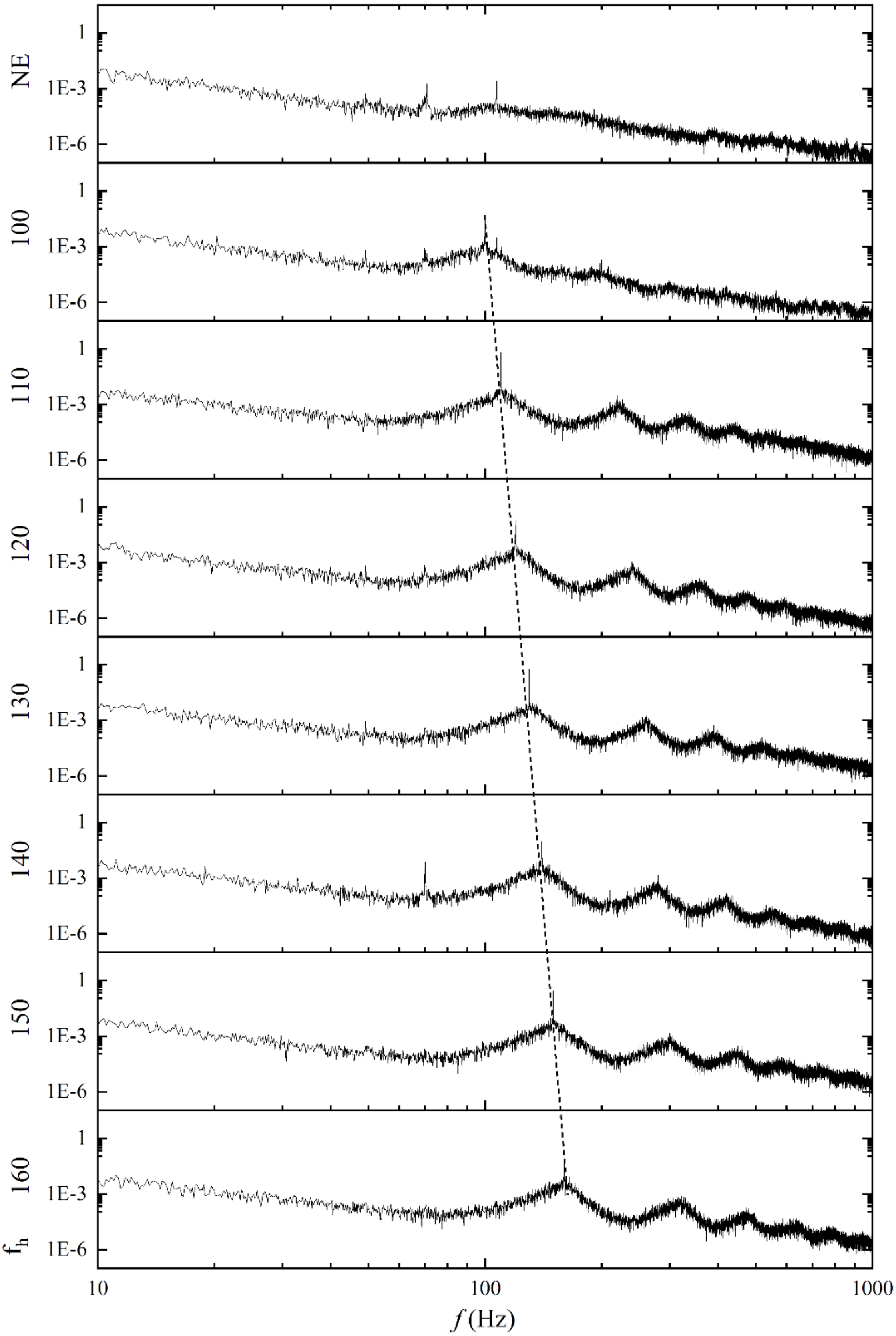

Figure 5.5 PSD of the hot-wire signal during generated excitation

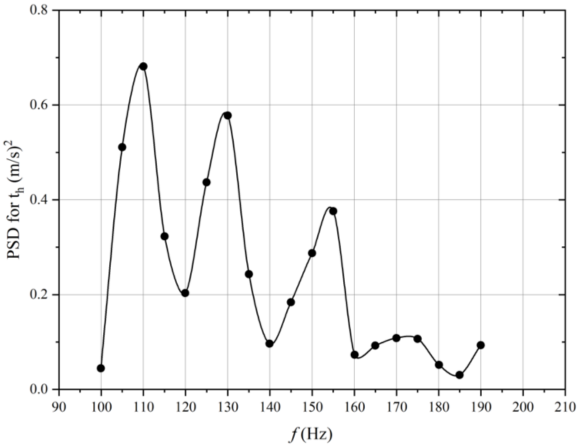

Figure 5.6 Maximum amplitude of the excited frequency

6. Analysis of the naturally developing separated boundary layer

In this chapter, the properties of the boundary layer for the reference cases i.e. the flow without acoustic forcing in the presence of APG are analysed. The velocity measurements were conducted at two Reynolds numbers: $Re_x = 185\,000$ ($U_{in} = 5$ m/s) and $Re_x = 370\,000$ ($U_{in} = 10$ m/s). A detailed description of the inlet conditions and streamwise static pressure distribution is included in Chapter 4. At the contraction part of the channel (see Figure 4.3) the flow accelerates while the laminar boundary layer (LBL) is developing. Further downstream the LBL is exposed to APG in the diverging part of the channel where laminar separation bubble occurs and the transition to turbulent boundary layer (TBL) occurs. In the relevant literature, it is also common to define the Reynolds number in this type of geometry using the core flow velocity at the trailing edge and the suction length, i.e. from the velocity maximum point to the trailing edge, instead of the length of the entire plate (Serrano, 2013). According to that definition the suction length is the length of the plate from the begging of APG section.

$$Re_{L_{APG}} = \frac{U_2 L_{APG}}{\nu} \qquad \text{(Eq. 9)}$$

Therefore, the Reynolds number for the cases studied in the paper will be calculated based on (Eq. 9) and equal $Re_{L_{APG}}$ = 175 000 and 350 000 respectively (see Table 6.1). Where U_2 is velocity at the APG ending and L_{APG} is length of APG section (see Figure 4.3 where dP / dx > 0).

Table 6.1 Investigated Reynolds numbers

U_{in} (m/s)	U_2 (m/s)	L_s (m)	L_{APG} (m)	Re_x	$Re_{L_{APG}}$
5	4.4	0.525	0.6	185 000	175 000
10	8.8	0.525	0.6	370 000	350 000

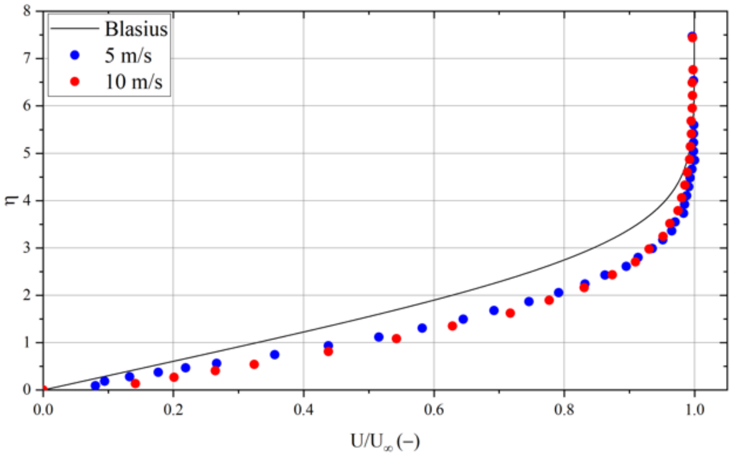

Figure 6.1 Comparison of the experimental velocity profiles with the Blasius profile

In order to check the similarity of the inlet conditions for the both cases and verify the laminar character of boundary layer a comparison was made between the reduced velocity profiles and the Blasius profile for a given distance (x = 400 mm). As can be seen in Figure 6.1, the two experimental profiles fully overlap. On the other hand, a some discrepancy with the laminar, self–similar Blasius profile is noticeable. The slight acceleration of the flow near the wall is due to the still present impact of the FPG in the upstream flow.

However, it can be seen that the profiles are similar, which demonstrates that the cases share also the comparable flow characteristics in the LBL on the lower flat plate before the bump crest.

Having characterised the boundary layer at the APG inlet, an analysis of the evolution of the boundary layer further downstream can be carried out. Initially, the boundary layer was studyed using a smoke visualisation (Figure 6.2). The visualisation was limited only to the case with a freestream velocity of 5 m/s due to insufficient performance of the available smoke generator. The smoke visualization provided important information about the flow patterns of the boundary layer and helped to further understand flow behaviour in this region. The recorded and presented in Figure 6.2 (bottom panel) image indicates that the separation bubble has its origin at a distance of approximately x = 525 mm from leading edge and reattachment was observed at x = 650 mm, which is consistent with the results from the HWA. The height of the separation bubble builds up to the coordinate *x* = 625 mm and then, as a result of the apparent breakdown of the flow, a rapid reattachment of the separated shear layer occurs.

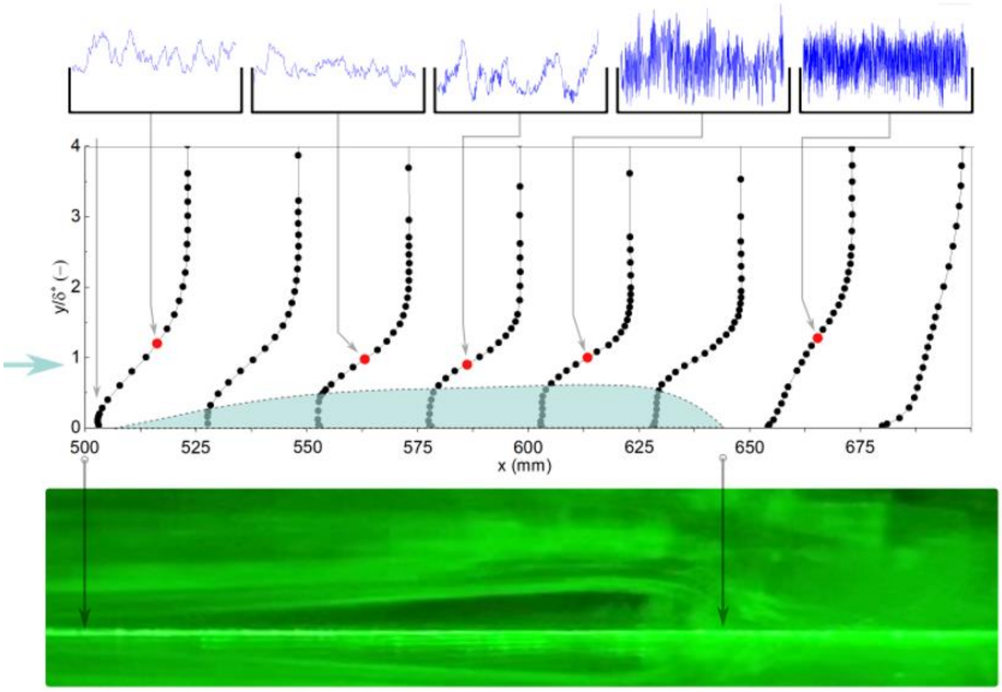

Figure 6.2 Separation bubble analysis visualisation

The mean velocity profiles (Figure 6.2 – central panel) obtained using single hot-wire probe allowed for quantitative analysis of the unseparated flow only as the probe used in this study allows to measure only the modulus of the instantaneous velocity vectors *U(t)* and *V(t)*, what makes the estimation of the direction of the flow impossible, resulting in no negative values in the profiles. Nevertheless, it is evident that the shape of the velocity profiles is consistent with the result of the visualisation, which is confirmed by the schematically marked area of detachment in Figure 6.2 (central panel). The upper part of Figure 6.2 shows the velocity signal waveforms recorded in the separated shear layer (at the wall normal location of u'_{max}). The first waveforms indicate the presence of low-frequency oscillations. Then, for the traverse *x* = 575 mm, initial evidence of flow breakdown and traces of turbulent spots appear, which then develop rapidly, leading to increased momentum transfer towards the wall and finally to reattachment of the flow and transition to turbulent boundary layer.

Once the flow behaviour was initially characterised, using flow visualisation, the further essential part of the study is devoted to Reynolds number impact on the separation bubble. The analysis will be based on mean velocity and velocity fluctuation profiles as well as on selected boundary layer parameters. The velocity profiles can provide insight into the flow conditions in the separation region (see Figure 6.3). The boundary layer was assessed at several traverses from *x* = 70 to 700 mm downstream of the leading edge. Velocity signals were recorded at up to 45 points ranging from the proximity of the wall to 150 mm above the wall in the normal direction to the flat plate. The acquisition time for single point was 40 seconds at frequency of 5 kHz. The distance from the wall (*y*) has been normalised with the displacement thickness (δ*), which represents the measure of an artificial shift of the wall position to obtain the same volumetric flow rate in the boundary layer for the inviscid flow as in the analysed viscous flow. By normalizing the distance from the wall in this manner, the influence of the boundary layer thickness on the velocity profile can be avoided, enabling a more accurate analysis of the flow in the boundary layer. At the initial stages of separation, when the flow is still laminar, the velocity profiles exhibit typical parabolic shapes, which are the results of the balance between the pressure gradient and the viscous forces in the fluid. The similar results were observed in many previous investigations (Hosseinverdi et al., 2012; Michelis et al., 2017; Nash et al., 1999).

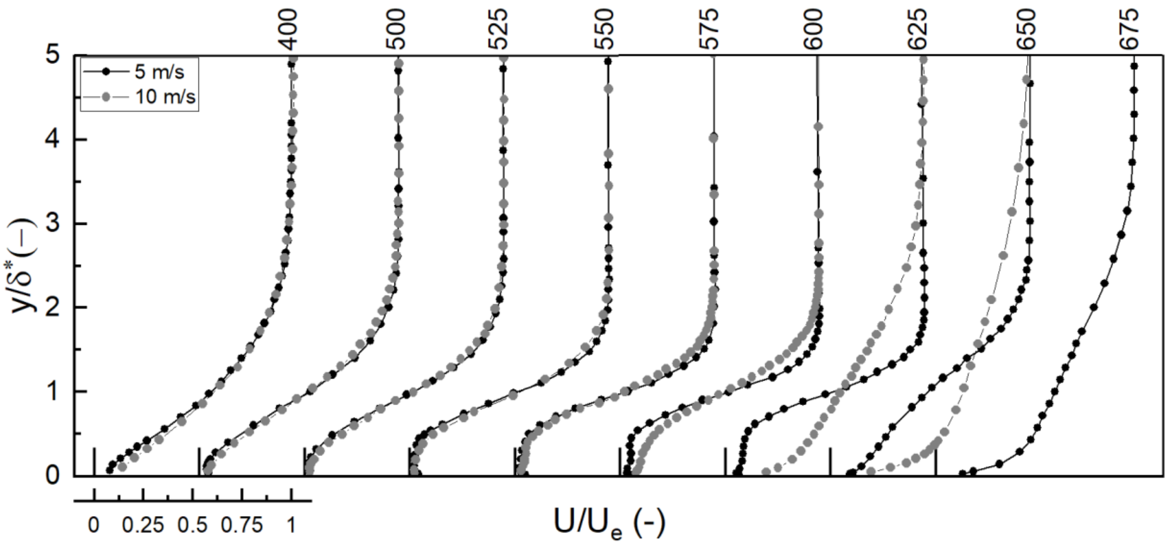

Figure 6.3 Velocity profiles measured in the APG region

When comparing the mean velocity profiles for the *x* = 400 and 500 traverses, some differences in shape are observed indicating a later flow separation for the higher Reynolds number. In the case of *U* = 5 m/s, an inflection point, which is characteristic of flow with separated boundary layer, is already present in the profile for *x* = 400. For the subsequent traverse, no significant differences in the profile shape are observed, while for *x* = 600 and especially *x* = 650 mm the velocity profile is more filled for the case *U* = 10 m/s, which is the result of an earlier initiation of the laminar-turbulent transition. Further downstream in the turbulent region the velocity profile is characterized by a high gradient of velocity near the wall and by the absence of an inflection point with increasing distance from the flat plate. That kind of profile shape is a typical representation of the turbulent region after the transition process in the separated boundary layer.

Analysing the velocity fluctuation profiles (Figure 6.4) no clear differences are observed up to *x* = 550. Then for higher Reynolds numbers, the fluctuation peak is reached earlier, which confirms the conclusions drawn from the analysis of the mean velocity profiles of an earlier initiation of the laminar-turbulent transition for that case. It is interesting to note that the position of the fluctuation peak in the laminar and an early transitional region scales on a displacement thickness, suggesting the presence of the low frequency streaky flow structures called Klebanoff mode (Matsubara & Alfredsson, 2001).

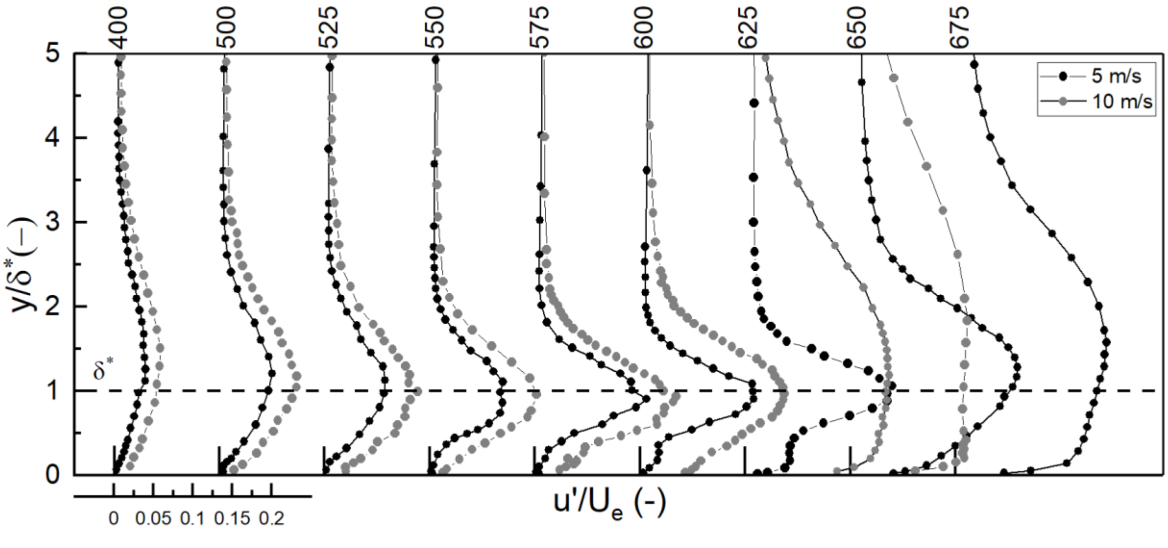

Figure 6.4 Distribution of normalized velocity fluctuations for the separated

bubble region

A more detailed analysis of the development of the near-wall flow is possible based on selected statistical quantities, the first of which is the boundary layer thickness δ_{99}. This parameter, is defined as the distance from the wall at which $U = 0.99U_\infty$ where U_∞ is a free-stream velocity. This parameter is influenced by several factors, including the Reynolds number, the pressure gradient or the geometry of the surface. Figure 6.5 shows the distribution of δ_{99} on the bottom flat plate. In the FPG flow region, it remains relatively constant while, beyond a certain coordinate (*x* = 400), it increases rapidly, which is a characteristic behaviour of δ_{99} in the APG flow region. The increase in δ_{99} is due to the combined effect of the pressure gradient and the viscous forces, and turbulence.

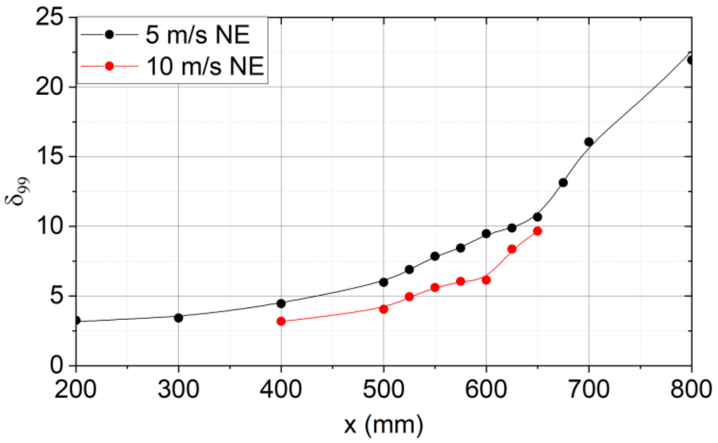

Figure 6.5 Distribution of the boundary layer thickness δ_{99}

The distribution of integral parameters δ^* (Eq. 10) and θ (Eq. 11), was showed in Figure 6.6a and 6.6b, respectively, where the error for both was calculated to be 2%. The momentum thickness θ represents the linear measure of amount of zero momentum deficit in the boundary layer compared to the freestream momentum.

Definitions of $\delta^*$and θ:

$$\delta^* = \int_0^\delta \left(1 - \frac{U}{U_\delta}\right) dy \qquad \text{(Eq. 10)}$$

$$\theta = \int_0^{\delta} \frac{U}{U_\delta}\left(1 - \frac{U}{U_\delta}\right) dy \qquad \textit{(Eq. 11)}$$

Figure 6.6 shows that the higher the Reynolds number the lower the displacement thickness, which is consistent with the observation of Lardeau et al., (2012). Moreover, at the separation region the integral parameter δ^* is also affected by Reynolds numbers the maximum is reached at *x* = 625 and *x* = 575 for *U* = 5 m/s and for *U* = 10 m/s, respectively. According to Simoni et al., (2017), the peak location of δ^* corresponds to the LSB maximum displacement positions (which approximates the core of the separated shear layer), whereas the maximum of the shape factor *H* (Eq. 12)*,* which usually occurs upstream, may be attributed to the onset of transition (Sarkar, 2008). These conclusions are supported by the analysis of integral parameter θ (Figure 6.6b), increase of which indicates a process of breakdown of the flow. These both parameters play an important role in determining the flow characteristics, and the indication of important phases of the separated bubble development.

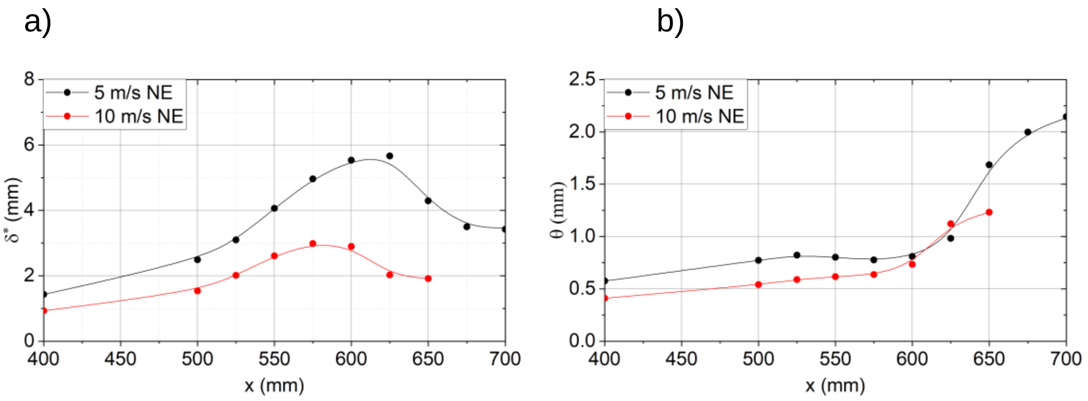

Figure 6.6 Distribution of displacement thickness (a) and momentum thickness (b)

Additionally, the shape factor *H* is a measure of the curvature of the boundary layer mean velocity profile. As seen in Figure 6.7, five characteristic areas can be distinguished. In the first area from *x* = 200 to *x* = 400, *H* exhibits constant value for both cases. This means that the negative pressure gradient present in this region has a stabilising effect on the boundary layer. In the second region, beyond the point *x* = 400, where the pressure starts to increase (see Figure 4.3) there is a sharp increase in the value of *H*. A qualitative change in the nature of the flow occurs from x = 500, where there is an approximate location of flow separation. As can be seen in Figure 6.7, at this point, the gradient in the shape parameter increases. Downstream that point the Reynolds number has the strongest impact. After reaching a maximum at x = 600 for U = 5 m/s and x = 575 for U = 10 m/s, respectively, the l-t transition process begins and the shape factor reduces continuously to the value typical for turbulent boundary layer. The increase in kinetic energy in the separated shear layer and the transport of momentum towards the wall result in rapid closure of the separation bubble. At a distance of x = 700 (for 5 m/s) the value of H is 1.59, and in the case of 10 m/s at a distance of x = 650 H = 1.55, indicating the presence of a turbulent boundary layer. It should be noted that the shape factor uncertainty is equal to 4%. a detailed analysis of the location of the separation point, the transition onset, and the reattachment point will be carried out below.

$$H = \delta^{*}/\theta \qquad \text{(Eq. 12)}$$

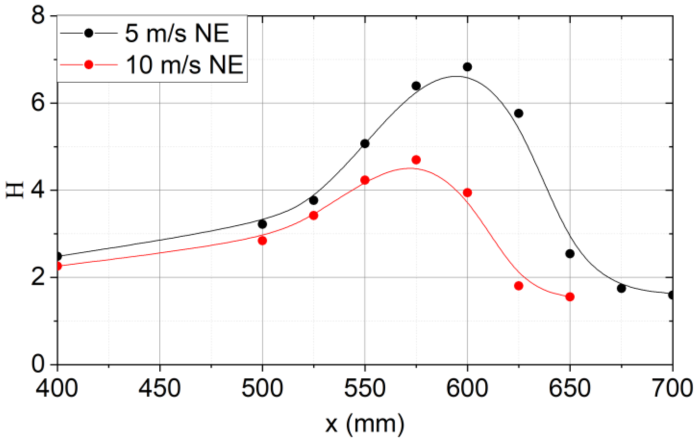

Figure 6.7 Distribution of the shape factor H

The one ofdimensionless parameters used to describe the flow regime in a boundary layer is Momentum Thickness Reynolds Number (Re_θ). Re_θ is often used to predict the onset of l-t transition in the boundary layer. The onset of the laminar-turbulent transition is located where the local value of the Re_θ is equal to the critical value Re_θ calculated from experimental correlations. There are several correlations that are commonly used, including Abu–Ghannam & Shaw, (1980), Hourmouziadis, (1989), and Mayle, (1991). The distribution of Re_θ (see Figure 6.8) is correlated with the θ and H curves and takes generally constant values in the laminar part of the separation bubble and increases in the rear part of the bubble, which is clearly visible on the graph.

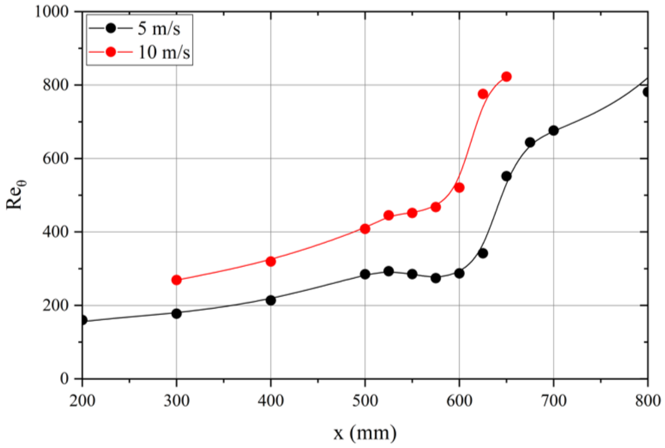

Figure 6.8 Distribution of Momentum Thickness Reynolds Number Re_θ

Another measure in determining the flow regime in a separated boundary layer is the wall shear stress $\tau_w = \mu dU/dy$, and it can be used to predict the separation onset and l-t transition point. The skin friction coefficient, marked C_f, is a factor that takes into account the wall shear stress and is often used as a surrogate for that measure. However, because of the inability to determine the velocity vector using a single hot-wire probe, obtaining C_f directly is a challenge. Techniques based on oil-film interferometry (Dróżdż et al., 2018; Tanner & Blows, 1976) can be used only far from separated region due to extensive impact of high oil–surface tension forces with respect to weak shear stress in separated region. Therefore, in the thesis, an approximation (Eq. 13) proposed by Johansen and Sorensen (1998) can be used to obtain an estimate of the skin friction coefficient.

$$Re_\theta \frac{C_f}{2} = -0.067 + 0.01977 \frac{(7.4 - H)^2}{H - 1} \qquad \textit{(Eq. 13)}$$

The presence of negative values of this coefficient indicates backflow and confirms the presence of a separation bubble. For the analysed cases (Figure 6.9), the negative value are observed in the range between *x* = 530 – 640 mm and 550–600 mm for 5 m/s and 10 m/s, respectively. This observation demonstrates that the size of the separated bubble is reduced as the Reynolds number increases.

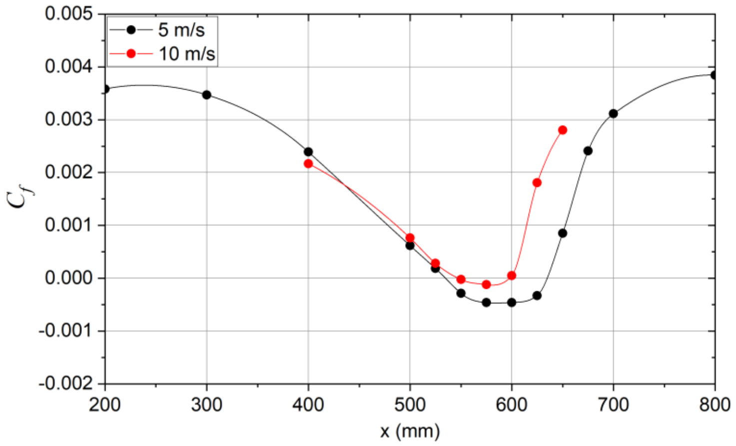

Figure 6.9 Distribution of skin friction coefficient C_f

In order to further characterise the flow the streamwise distributions of the velocity fluctuation maximum reduced by the edge velocity u'_{max}/U_e are shown in Figure 6.10. A straight line, in the range 500 – 650 mm for the lower and 500 – 575 mm for the higher Reynolds number, indicates an exponential amplification of disturbances. Initially, it is a result of streamwise streaks (Klebanoff mode) while in the rear part K-H instability mechanism dominates. The slightly different growth rates measured in the fore and the rear parts of the separated shear layer show analogies with the different amplification observed by Marxen et al., (2004). The details will be discoussed in Chapter 7.

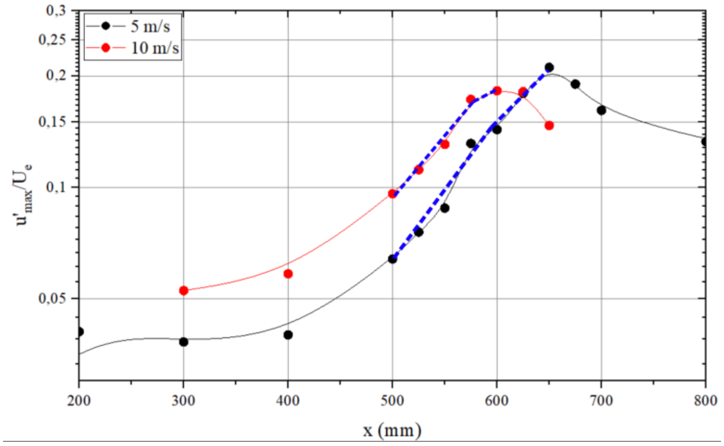

Figure 6.10 Distribution of the maximum value of the root mean square

The transient amplification in the fore part of the bubble, attributed to spanwise waves (Klebanoff mode), is substituted by an exponential behaviour in the rear part of it, typical of the K-H instability mechanism (Simoni et al., 2017). As reported in the literature (Dovgal et al., 1994; Yarusevych et al., 2007) the higher the Reynolds number, the higher the growth rate. However, this effect is not observed in current research. A more detailed analysis of the mechanism of destabilisation of flow in the separated shear layer will be presented in the next chapter.

However, analysis of the distribution of the velocity fluctuation maximum does not precisely indicate the onset point of the transition, and thus the appearance of the first turbulent spots. Diagnostics in this aspect can be carried out on the basis of velocity time-traces analysis. An interesting alternative is the determination of the the intermittency factor γ. It is defined as the fraction of time that the flow remains turbulent. The value of the intermittency factor varies from 0 to 1, where the zero value represents a fully laminar region and the value of one represents a fully turbulent regime. This definition shows that it is a convenient parameter to discriminate between laminar, turbulent, and transitional regions of the flow.

The calculation of streamwise intermittency function was carried out to evaluate the spatial distribution of turbulent spots density within the boundary layer. The method of γ calculation is described in detail in Appendix 1. As demonstrated in Figure 6.11 for the case of 5 m/s, the transition region extends from *x* = 625 mm to *x* = 675 mm, while for the case of 10 m/s, the transition region is located between *x* = 575 mm and *x* = 625 mm.

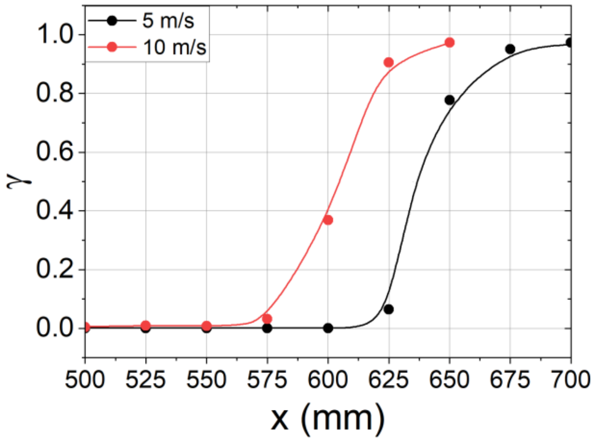

Figure 6.11 Streamwise intermittency distribution

The results demonstrate that as the Reynolds number increases, the transition onset moves upstream. This can be attributed to the increase in inertial forces relative to the viscous forces, which leads to an enhancement in the rate of energy transfer from the large-scale structures to the smaller scales, resulting in an increase in turbulence intensity and earlier onset of turbulence in the flow.

The analysis carried out so far indicates that a number of boundary layer parameters can be used to diagnose the laminar separation and indicate its characteristic points, which generally give converging indications. Before investigating the influence of acoustic forcing, it is necessary to define precisely reference cases. For this reason, the following will summarize the study by sorting out information on the separation onset (x_s), the length (L_s) and the position of maximum height (x_m) of the separation bubble, the transition onset (x_t), the end of the l-t transition (x_T) and the reattachment point (x_r).

It is, of course, recognised that there is the potential for uncertainty in definition of these locations based on hot-wire data, particularly because this is due to the inability to determine the velocity vector using the single hot-wire probe. Therefore, the decision is made on the basis of a range of comprehensive available data. In addition, due to the measurements sparsely located in the longitudinal direction within the separation bubble, the interpolation procedure was applied. Finally, the validity of the characteristic points was examined by comparing the indications obtained on the basis of the various available parameters. All data, separately for both Reynolds numbers, are summarised in Table 6.2

To determine the position of flow detachment x_s, two parameters, H and C_f, were utilized along with qualitative analysis from smoke visualization and average velocity profiles. An unambiguous indication of the point of separation is possible based on the C_f coefficient. However, it should be remembered that this distribution (Figure 6.9) was obtained based on Eq 13. This equation is based on Johansen and Sorensen correlation, which stated that detachment occurs at a value of the shape factor $H = 4$. Then x_s would be $x_\mathrm{s} = 527$ for 5 m/s and 545 for 10 m/s, respectively. However, other reports in the literature (Simoni et al., 2017) indicate that a value of $H = 3.5$ should be a more appropriate criterion, in which case x_s would be $x_s = 510$ mm for 5 m/s and $x_s = 530$ mm for 10 m/s, respectively.

Table 6.2 Separation bubble characteristics (NE)

U_{in} (m/s)	Method	x_s (mm)	x_m (mm)	x_t (mm)	x_T (mm)	$x_T - x_t$ (mm)	x_r (mm)
5	s.visulisation	525	625	–	–	–	650
	δ^*	525	625	–	–	–	–
	θ	525	–	600	700	100	–
	H (Drela)	527	–	600	700	–	–
	H (Simoni)	510	–	600	700	–	–
	C_f	530	–	–	–	–	640
	γ	–	–	600	700	–	–
10	s.visulisation	–	–	–	–	–	–
	δ^*	550	575	–	–	–	–
	θ	–	–	575	650	75	–
	H (Drela)	545	–	575	650	–	–
	H (Simoni)	530		–	–	–	–
	C_f	550	–	–	–	–	600
	γ	–	–	550	650	–	–

The C_f based indications, which appear to be somewhat overestimated specify x_s to be equal $x_s = 530$ for 5 m/s and $x_s = 550$ for 10 m/s, respectively. Helpful indicators, which however, are already reflected in the shape factor, are also δ^*, and θ. The respective distributions (Figure 6.6) show a change in trend between the LSB and APG area with detachment. However, it must be acknowledged that in this case interpretation of the distributions is quite subjective. Although the smoke visualisation gave only a qualitative insight into the flow, it can be stated with a high degree of confidence, based on the image in Figure 6.2, that for 5 m/s the separation onset is at $x_s = 525$. As can be seen from the data presented above, the position of the separation onset is, to some extent, dependent on Reynolds number. Data from the literature give different and inconsistent conclusions in this matter. For example, Lou and Hourmouziadis (2000); Simoni et al. (2017) concludes that the x_s point is not dependent on *Re*, while a certain sensitivity (shift in downstream direction) is confirmed by the works of Park, Shim, and Lee (2020); Suzen et al. (2003) – where LSB was developed on aerofoil and depended of the angle of attack and Reynolds number. This effect is dependent on the Reynolds number range considered here, the local value of the adverse pressure gradient and the level of turbulence intensity. On the other hand, some investigators (Istvan et al., 2018; Istvan & Yarusevych, 2018) present a shift of x_s upstream.

Another characteristic feature is the bubble maximum displacement position x_m, which is generally agreed to correspond to the location of maximum displacement thickness δ^*. The location of this point either coincides with the transition onset or is located slightly downstream of this point. Marxen et al. (2004) and Simoni et al. (2012) observed that *u'* grow up to the bubble maximum displacement position, where saturation of this parameter occurs. In the case considered, the location is clearly marked as x_m = 625 and 575, for the lower and higher Reynolds numbers, respectively. Verification of these values is only possible based on the smoke visualisation for 5 m/s, the interpretation of which is consistent with the above conclusion.

Two other distinctive points are the transition onset and end of the transition. Here, we have several parameters available, i.e. θ, *H*, *u'* and γ. Park et al. (2020) show that near the streamwise location of maximum shape factor, there is rapid growth at all measurable frequencies, which is indicative of the onset of transition. This is consistent with Sarkar (2008) observation that the peak of the shape factor *H,* which usually occurs upstream *u'* maximum, shows the location of the onset of transition x_t. Based on these rules, the start of the transition can be determined at x_t = 600 and x_t = 575, for the lower and higher Reynolds numbers, respectively. These conclusions are supported by an analysis of integral parameter θ (Figure 6.6b), which does not change significantly in the fore portion of the bubble where the near-wall flow is nearly stagnant. Then the rapid increase of θ indicates a process of breakdown of the flow. An unambiguous parameter is also the intermittency factor γ. As the analysis of the graph in Figure 6.11 and the data in Table 6.2 shows, the results here are consistent. Based on the same quantities, the end of the transition can also be determined and equals x_t = 700 and x_t = 650, for the lower and higher Reynolds numbers, respectively. From the data presented, it appears that the Reynolds number has a very strong influence on the l-t transition and the resulting length of the separation bubble. It was confirmed that the locations of transition onset and reattachment tended to move upstream as the Reynolds number increased. It should also be noted that the transition length became shorter with increasing Reynolds number.

Finally, the point of the reattachment, should also be analysed. It can be determined, with the reservations formulated earlier, that it is located at the positions x_r = 650 and 600, for the lower and higher Reynolds numbers, respectively. The obvious conclusion, then, is that the reattachment tended to move upstream with the Reynolds number resulting in a shorter separation bubble. An important observation is that in both cases, LSB reattachment occurs while the transition process is still not fully complete.

The comprehensive data analysis indicates that, based on single hot-wire probe measurements, even with relatively sparsely located measurements, characteristic wall flow points can be assessed with a high degree of accuracy. It must be kept in mind, however, that the identified locations suffer from a certain level of uncertainty since they depend on number of factors like measurements accuracy, accuracy of calculations, and data approximation.

Table 6.2 contains the *x* coordinates of key phases in the development of a separated bubble, calculated based on analysed parameters of the boundary layer, for both tested cases. These stages include the initiation point of the separation bubble, the laminar-turbulent transition point, and the reattachment point. This information is crucial for determining the extent of the separation bubble and further impact of acoustic excitation on the separated bubble, as will be demonstrated in the subsequent chapters. The positions of the above characteristic points are also shown in Figure 6.12.

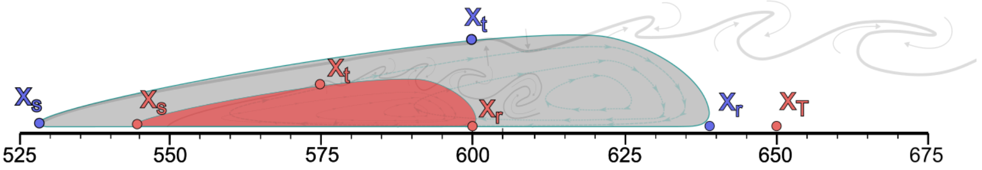

Figure 6.12 Scheme of LSB dimensions (5 and 10 m/s)

In summary, this chapter highlights the discrepancies in the results that help to identify the key stages in the development of the separated shear layer. To determine the position of x_s, two parameters, H and C_f, were utilised along with qualitative analysis from smoke visualization and mean velocity profiles. Based on the correlation proposed by Drela (2014), it can be stated that the separation begins at x_s = 527 mm and x = 545 mm for cases of 5 m/s and 10 m/s, respectively. On the other hand, the C_f distributon indicate the separation onset at distances of x_s = 530 mm and x_s = 550 mm for the 5 m/s and 10 m/s cases, respectively.

The identification of the laminar-turbulent transition onset is based on the intermittency function and the distribution of u'_{max} (see Figure 6.10), as it is apparent from of u'_{max} distributions the flow breakdown starts at the distances of approximately x_t = 575 mm and x_t = 625 mm from the leading edge for test cases 10 and 5 m/s, respectively. The intermittency function (Figure 6.11) supports this estimates and also pinpoints the onset of the laminar-turbulent transition at x_t = 575 mm and x_t = 625 mm.

The reattachment point in a separated boundary layer is determined based on the distribution of the friction coefficient along the surface. The location of the reattachment point was found to be at a distance of 630 mm from the leading edge for the case of 5 m/s and 600 mm from the leading edge for the case of 10 m/s. For the test case, at 5 m/s the results are well confirmed with the smoke visualisation.

The results of the analysis presented in this chapter indicated that the Reynolds number has a significant impact on the size of the separated boundary layer. The increase in Reynolds number was found to result in a decrease in the size of the separated bubble, which is consistent with previous studies in the field (Burgmann & Schröder, 2008; Istvan et al., 2018; Istvan & Yarusevych, 2018; Lou & Hourmouziadis, 2000) and many others. Additionally, the Reynolds number also influence the position of other phases in the development of the separated bubble. As demonstrated in Table 6.2 for the case of 10 m/s, the separation onset is shifted downstream by ~ 20 mm compared to the case of 5 m/s. However, the position of formation of the first turbulent spots is shifted upstream by 50 mm, and the reattachment point is shifted upstream by 40 mm. These findings suggest that an increase in the Reynolds number leads to a later initiation of the separation point and an earlier l-t transition in the boundary layer, which in turn results in an earlier reattachment of the separated bubble.

7. The influence of acoustic excitation on the development of the boundary layer in the separation bubble.

7.1. Overall assessment of the impact of acoustic forcing on the laminar separation bubble

One of the primary tasks of the thesis was to find an answer to the question of how acoustic forcing, broadband and harmonic, affects laminar separation bubble and what mechanism is responsible for the observed effects. To this end, as shown in Table 7.1, the research programme was arranged as follows. For the lower Reynolds number, broadband noise forcing with two SPLs was applied. For the higher Reynolds number, a broadband noise forcing with two SPLs was applied, plus a monoharmonic forcing with a selected frequency. A description of the choice of this forcing frequency is given in Chapter 5. This made it possible to study the impact of acoustic energy, type of forcing (broadband or harmonic) for flows characterised by different Reynolds numbers.

Table 7.1 Parameters of the boundary layer (BL) at separation point

Re_x (–)	Case	U_e (m/s)	δ_{99} (mm)	H (–)	Re_{δ^*} (–)	Re_θ (–)
185 000	NE (87dB)	5.43	6.89	3.77	1105	293
	125dB	5.39	7.00	3.99	1118	281
	135dB	5.38	6.62	3.85	1078	280
370 000	NE (89 dB)	10.84	5.6	4.23	1911	452
	125dB	10.81	5.32	3.75	1709	456
	Sin125 dB	10.71	5.17	4.0	1684	420
	135dB	10.69	5.33	2.73	1540	461

To establish reference conditions, the key parameters at the separation point ($x \approx 525$ mm) for all analysed cases have been calculated and presented in Table 7.1. The table includes the mean velocity at the boundary layer edge (U_e), boundary layer thickness (δ_{99}), shape factor (H) and Reynolds numbers based on displacement thickness (Re_{δ^*}) and momentum thickness (Re_θ). The data indicate that for lower Reynolds numbers, only a slight change in flow parameters is observed at the point of separation with increasing SPL, while for higher Reynolds number, stabilising effect of acoustics on near-wall flow is observed. This is evidenced by a reduction in the shape factor as well as Re_{δ^*}. The impact of acoustic forcing on different phases of boundary layer development will be analysed later in this section.

To demonstrate the qualitative effect of acoustic forcing on the detachment bubble, Figure 7.1 shows the freestream velocity U_e distributions for both Reynolds numbers for non–excited and all excited conditions. The values have been normalized with the edge velocity at the throat of the channel $U_{\infty x = 400}$. The dashed line represents the condition of the attached boundary layer. The results show that boundary layer separation promotes, for the NE cases, the development of a relatively linear reduction of the U_e, followed by its drop to the level of attached flow shown by the dashed line, indicating the reattachment of the separated shear flow. These data also suggest that for the lower *Re* the reattachment point moves upstream with the response to acoustic forcing, while for the higher *Re* acoustic forcing reduces almost entirely the separation bubble.

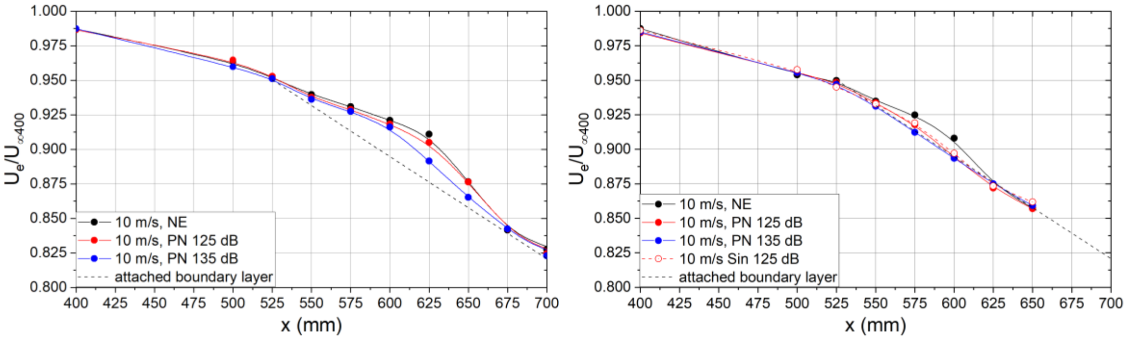

Figure 7.1 Distributions of edge velocity U_e/U_{in} in the LSB region for $Re_x = 185\,000$ (a) and $Re_x = 370\,000$ (b).

To assess the impact of acoustic forcing more precisely, the mean velocity profiles and velocity fluctuations profiles in the successive traverses from $x = 70$ to 700 mm were analysed. Representative mean velocity profiles for all cases are shown in Figure 7.2. It is important to note that mean velocity is reduced by U_e, which scale is presented on the bottom left corner of the figure. It can be observed that in the initial phase, where the flow is laminar, the velocity profiles of cases with noise excitation overlap with reference profiles (NE). These findings indicate the insensitivity of the laminar flow to external acoustic influences. However, in the traverse $x = 625$ mm (for a lower Reynolds number) and in the traverse x = 575 mm (for a higher Reynolds number), the influence of acoustic forcing becomes evident, as indicated by an earlier gradual increase of momentum near the wall. On the last traverses (x = 675 mm for a lower Reynolds number and x = 625 mm for a higher Reynolds number) profiles overlap, which also shows the low susceptibility of the turbulent flow to the impact of acoustic excitation. The evolution of these profiles is consistent with U_e distributions presented in Figure 7.1. A comparison of two cases with acoustic excitations of 125 and 135 dB indicates that the SPL of the excitation has a clear impact on the near-wall flow. It is apparent that this effect is significantly stronger for SPL = 135 dB. As stated above, forcing causes the boundary layer to be almost attached for higher *Re*.

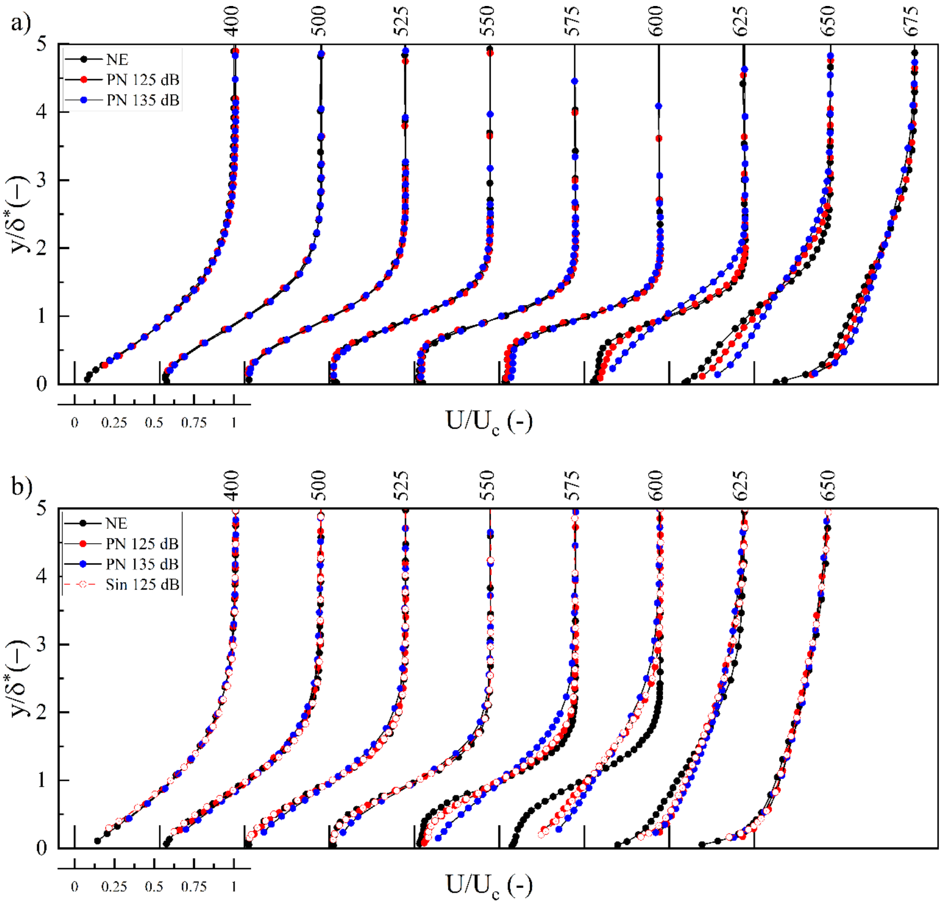

Figure 7.2 Mean velocity profiles for non-disturbed and disturbed cases for $Re_x = 185\ 000$ (a) and $Re_x = 370\ 000$ (b).

In a similar layout Figure 7.3, shows turbulence intensity profiles. The analysis of these data confirms the change in the shape of the *u'* profiles under the influence of different SPLs in the l-t transition region.

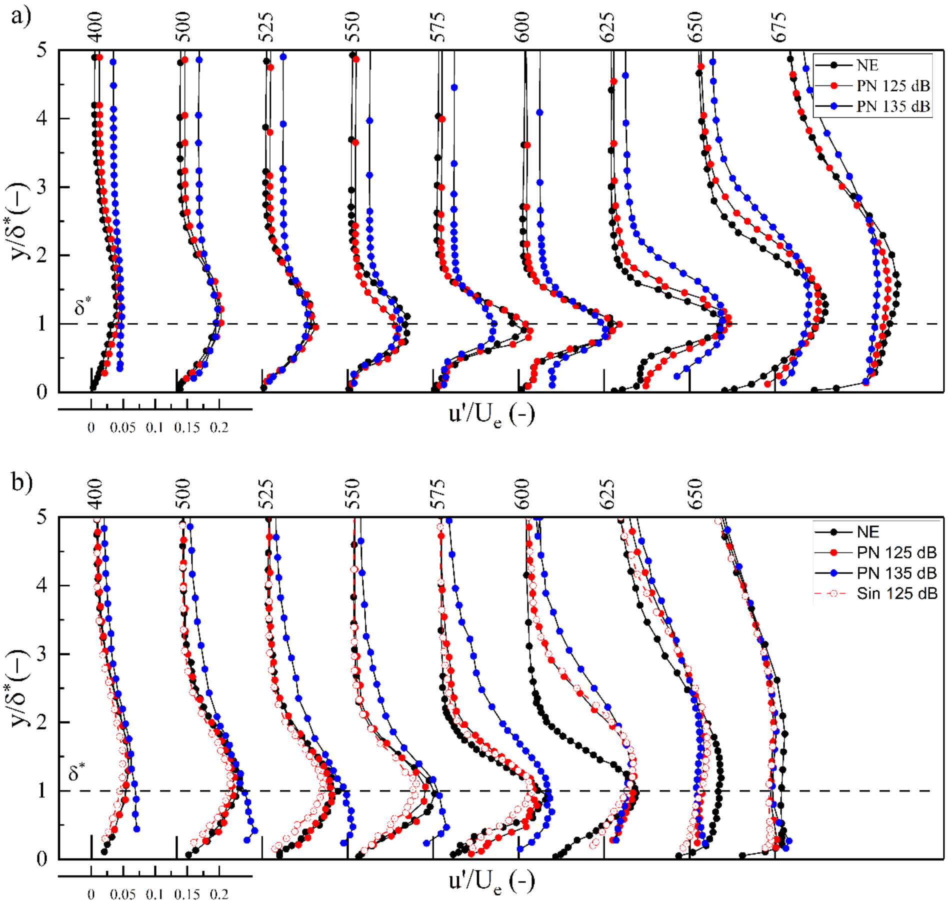

Figure 7.3 u' profiles for non-disturbed and disturbed cases for $Re_x = 185\ 000$ (a) and $Re_x = 370\ 000$ (b).

The first observation concerns the energy level of the flow outside the BL. It can be seen that for SPL = 135 dB there is a few percent increase in the turbulence intensity in the free-stream. The reason for this effect is not clear. However, at such a high sound pressure level, there may exist an impact of the acoustic pressure on hot-wire cooling due to flow density variation which has, however, minor effect inside BL. In the boundary layer, in turn, in the fore part of the separated bubble ($x \approx 525 – 575$ mm), acoustic forcing causes a reduction in the level of *u'* in the maximum for some cases. This is probably an effect of interaction with longitudinal structures (Klebanoff mod), which will be discussed later. This is followed by an increase in the thickness of the shear layer and redistribution of energy towards the wall, as well as towards the outer edge of the boundary layer and the strongest changes are observed in the rear part of the separation for ($x > 575$ mm). One can notice that the SPL is of great importance, while the differences between the effect produced by pink noise and by monoharmonic forcing are almost negligible.

7.2 Analysis of effect of broadband acoustic excitations on boundary layer flow for test case 5 m/s.

This chapter is aimed to analyse a few most important boundary layer parameters which will help to get deeper knowledge on the effect of acoustic excitation on separated flow. Figure 7.4 shows the distribution of integral parameters δ^* and θ. In the Figure 7.4a a reduction of δ^* maximum values in response to SPL can be observed. A particular change can be noticed downstream x = 525 mm, where, as was presented in Chapter 6 the separation onset was detected. These changes indicates decreasing of LSB thickness under the acoustic impact. The maximum value of δ^* moves gradually upstream under the influence of acoustics indicating an earlier l-t transition onset. These conclusions are consistent with analysis the shape of the momentum thickness θ curves (Figure 7.4b). The θ distributions starts to deviate above x = 600 mm, indicating an increase in energy in the separated shear layer resulting from turbulisation of the flow.

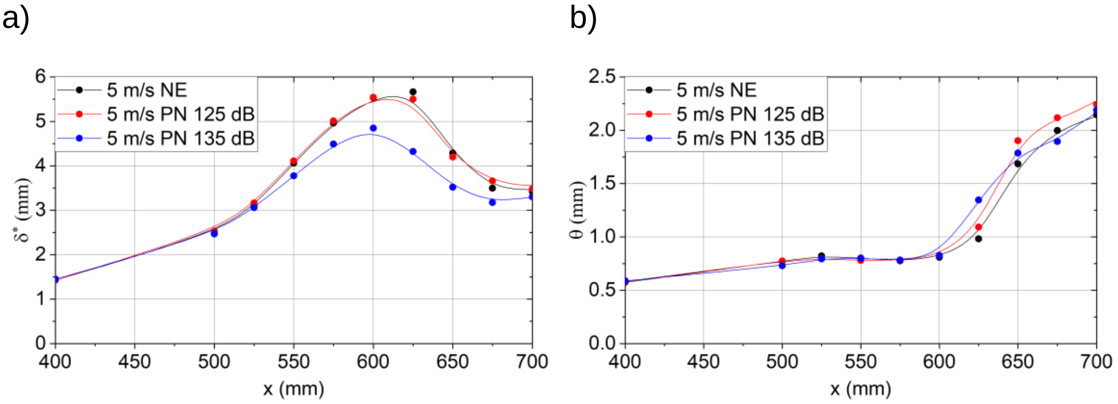

Figure 7.4 Distribution of displacement thickness (a) and momentum thickness (b)

Figure 7.5a depicts the distribution of the shape factor H, across the surface of the flat plate. Notably, an evident increase in H occurs at x = 500 mm, attributed to the influence of APG. At x = 525 mm, H reaches a value close to 4, which, as discussed in Chapter 6, indicates the separation of the laminar boundary layer. High value of the shape factor within the range x = 525 – 625 mm confirms the presence of LSB. Furthermore, the peak value of the shape factor identifies the position where the l-t transition is initiated. For the undisturbed flow case, this transition onset is observed at $x \approx 600$ mm. It is difficult to judge on the relative change in the transition onset location in the cases with the acoustic excitation active, based only on shape factor due to a limited number of experimental data. However, comparison of results in Figure 7.2a and Figure 7.3a reveals small changes in the mean velocity and u' profiles within the streamwise distances of x = 600 – 650 mm when subjected to acoustic excitation at an SPL = 125 dB. A much significant effect on the separated boundary layer is observed in the range of x = 550 – 625 mm in the case of acoustic excitation at SPL = 135 dB. A huge decrease of H value suggest the decrease of the size of LSB and an earlier laminar-turbulent transition. Notably, from a statistical perspective, despite the intense acoustic excitation, there is no observable impact on the laminar (x < 500 mm) and fully turbulent (x > 675 mm) boundary layers. Additionally, assuming that the shape factor at separation remains constant at $H = 4$ for all cases (excited and unexcited), it can be concluded that the effect of acoustic excitation on the separation onset (x_S = 527 mm) is hardly noticeable. The above analysis therefore demonstrates that acoustic excitation has a huge impact only on the l-t transition flow region.

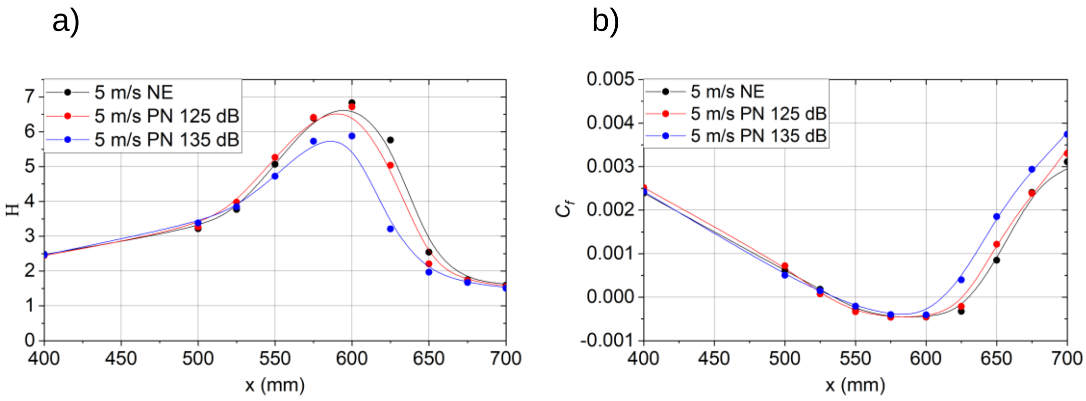

Figure 7.5 Shape factor (a) and skin-friction coefficient (b) distributions

The effect of acoustics excitation is also well reflected in the distribution of the friction coefficient C_f (Figure 7.5b). At the point where the value of C_f transit from positive to negative values, the separation onset is identified. A return to positive values indicates a position of the reattachment point of the separated bubble. The friction coefficient indicates that the acoustic excitation does not have a significant impact on the separation onset, but it has an effect on the reattachment point. These observations confirm that the conclusions reached based on the H and C_f parameter are consistent.

To gain a deeper understanding of the influence of acoustic excitation on the transition process in the separated boundary layer, the time-traces for the selected lower Reynolds number were analysed in Figure 7.6. Four streamwise distances, x = 575 mm, 600 mm, 625 mm, and 650 mm were chosen for this purpose. At each location, the velocity signal was measured at the same wall–normal distance, y = 2 mm. In the unexcited case (NE), only large-scale instability waves are visible in the free shear layer of the bubble at x = 575 mm and 600 mm. The disturbance amplitudes increase at x = 625 mm and the first signs of turbulent spots can be observed. Breakdown to turbulence occurs in the next traverse, i.e. at x = 650 mm. In the presence of acoustic forcing at 125 dB (Figure 7.6b), high-frequency perturbations are superimposed on low-frequency unsteadiness and are observed at x = 575 mm and 600 mm. However, the energy of these perturbations is not sufficient to induce turbulisation of the flow. The distinct change in the shape of the time signal between cases can be seen from x = 625 mm onwards, where, with acoustic amplification, more and more events that resemble the shape of turbulent spots are visible in the signal. For example, for SPL = 135 dB (Figure 7.6c), the time traces at x = 625 mm resemble the time traces for the unexcited flow (Figure 7.6a) at x = 650 mm, indicating an earlier turbulence breakdown with the acoustic excitation being activated. At a distance of 650 mm, the time traces for all cases show a similar heavily perturbed flow character, suggesting that the transition is almost complete, which is in line with the trend of the shape factor observed in Figure 7.5a.

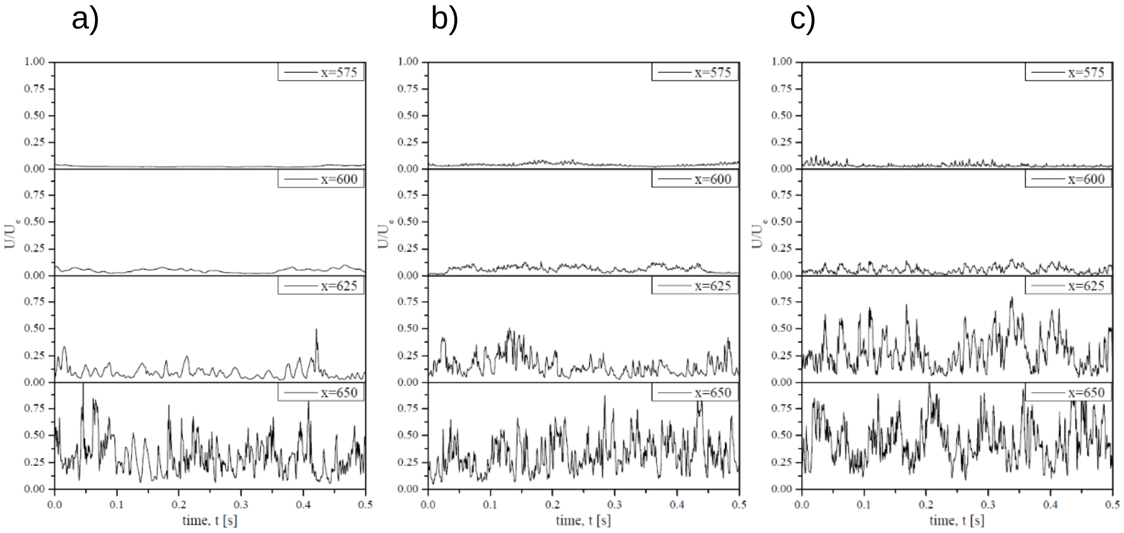

Figure 7.6 Sample hot-wire signals for the test case 5 m/s: without the acoustic excitation (NE) (a), with the acoustic excitation SPL = 125 dB (b) and SPL = 135 dB (c).

Figure 7.7 shows the intermittency function for different levels of acoustic broadband excitation. As can be seen, the ramp-up of the intermittency function shifted upstream in response to acoustic excitation. For cases, PN 125 dB and PN 135 dB ramp-up can be seen at the distance *x* = 600 mm and *x* = 575 mm, respectively, whereas for not disturbed case start at the distance *x* = 625 mm. As can be seen, as SPL increases the gamma curves begin to deviate earlier, indicating an increase in energy in the separated shear layer resulting from tubulisation of the flow. Base on this data one can determine the transition onset on 600 mm for SPL = 125 dB and 575 for SPL = 135 dB. Looking at the slope of the intermittency function, it can be concluded that the acoustic forcing does not significantly affect the length of the l-t transition.

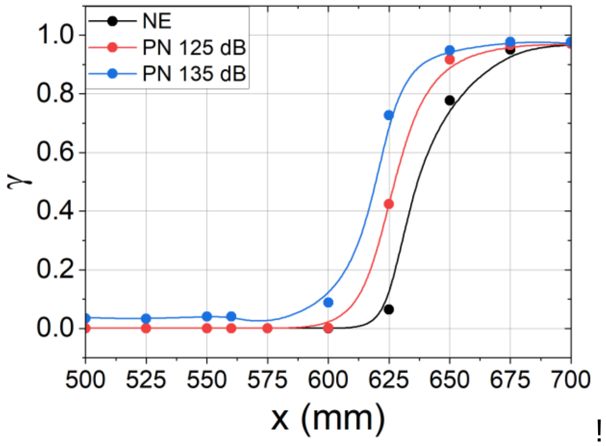

Figure 7.7 Intermittency distribution (test case 5 m/s)

Table 7.2 Separation bubble characteristics points(case 5 m/s)

U_{in} (m/s)	Test case	x_s (mm)	x_t (mm)	x_T (mm)	$x_T - x_t$ (mm)	x_r (mm)
5	NE	525	625	700	75	630
	PN 125 dB	525	600	675	75	620
	PN 135 dB	525	575	675	100	610

Based on analysed parameters presented in this chapter important stages of separated bubble development can be described (see Table 7.2). Schematically, the size with characteristic of LSB shown on the Figure 7.8.

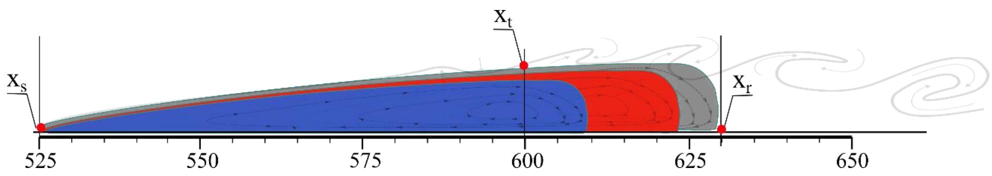

Figure 7.8 Scheme of LSB dimensions (5 m/s case)

7.3 Analysis of effect of broadband acoustic excitations on boundary layer for test case 10 m/s.

In the previous chapter, the experimental results of the effect of acoustic excitation on the boundary layer flow were presented for a test case with a velocity of U = 5 m/s. This section focuses on examining the impact of acoustic excitation on the separated boundary layer flow at a higher Reynolds number (U = 10 m/s). Another difference is the use of, in addition to broadband noise excitation, a harmonic signal (Sin 125 dB). Generated signal has a sinusoidal shape with a frequency 110Hz and SPL on the outlet of the loudspeaker equals to 125 dB. Details of the selection of this frequency are described in Chapter 5.2.

Figure 7.9 illustrates the distribution of integral parameters δ^* and θ. In Figure 7.9a, a clear reduction in the maximum values of δ^* can be observed in response to increasing SPL. Important to note, a drop of δ^* for PN 135 dB, at the location of separation onset for NE case (x = 550 mm). These observations indicate a decrease in the thickness of LSB under the influence of acoustic excitation. Moreover, the maximum value of δ^* gradually shifts upstream, indicating an earlier onset of the l-t transition under the influence of acoustics. These conclusions are in line with the analysis of the momentum thickness θ curves (Figure 7.9b). The θ distributions exhibit overlapping values up to x = 550 mm, after which the curves for PN 125 dB, Sin 125 dB, and 135 dB begin to deviate earlier, signifying an increase in energy within the separated shear layer as a result of flow tubulisation induced by the acoustic excitation. When comparing test cases involving acoustic excitation, it is evident that the impact on the flow is similar between the case with broadband excitation (PN 125 dB) and sinusoidal excitation at (Sin 125 dB). This similarity is observed despite the difference in the frequency range of the generated energy. In the first example, the energy is spread across the range of frequencies 100 – 650 Hz, while in the second example, it is concentrated around 110 Hz.

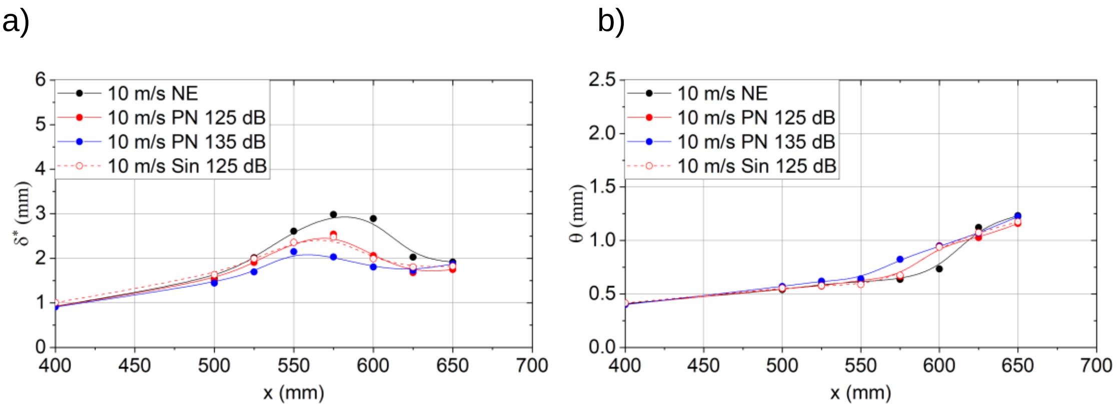

Figure 7.9 Distribution of displacement thickness (a) and momentum thickness (b)

Figure 7.10a illustrates the spatial distribution of the shape factor *H* along the surface of a flat plate. Similar to the methodology discussed in Chapter 7.2.

A noticeable observation is that the impact of acoustic excitation for the higher Reynolds number case exhibits a significant impact on the size of the separated bubble. For the PN 125 dB and Sin 125 dB cases, the flow is at the limit of detachment, while for 135 dB the layer is already attached. Since under the impact of Re, the separated bubble decreases in size, the use of active acoustic excitation leads to removal of separated bubble. This observation is confirmed by *H* values lying below 4, indicating the absence of a fully formed separated boundary layer.

Comparing the cases with the same sound pressure level of 125 dB, the influence of signal type on boundary layer behaviour can be demonstrate. Specifically, when employing a sinusoidal signal for acoustic excitation, it is observed that the maximum value of shape factor shifts upstream (*x* ≈ 550) in comparison to the use of broadband acoustic excitation (*x* ≈ 575). This phenomenon can be attributed to the flow's enhanced susceptibility to excitation near its natural frequency. As a result, the flow experiences a slightly earlier loss of stability. But still, the highest effect, within investigated cases, has SPL of generated noise. As can be seen, the use of pink noise with SPL = 135 dB leads to decreasing of *H* values (PN 135 dB).

These results clearly indicate that, in the case of broadband forcing, only frequencies occurring in the natural flow (K-H instability) are excited, while they are probably attenuated by the layer and do not play a significant role in the initiation of flow instability.

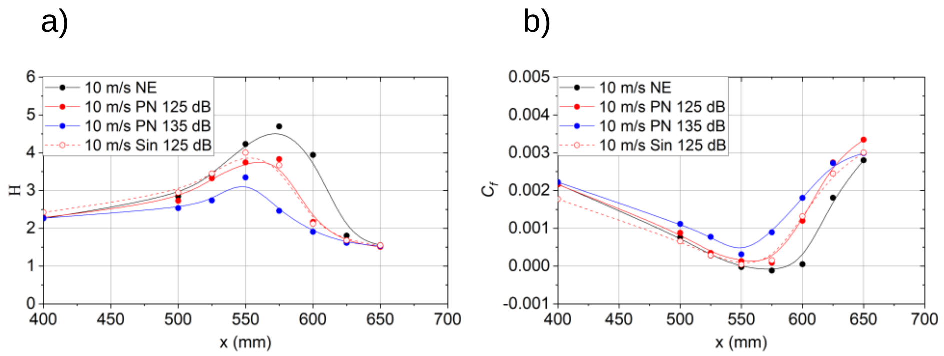

Figure 7.10 Shape factor (a) and skin-friction coefficient (b) distributions

The absence of separated bubbles is confirmed by the distribution of the skin-friction coefficient, as depicted in Figure 7.10b. In cases involving acoustic excitation, the absence of negative values is notable. These observations provide additional confirmation that the conclusions derived from the analysis of the shape factor and the friction coefficient are consistent.

An analysis of velocity time traces were conducted for each of the tested cases, including NE, PN 125 dB, Sin 125 dB, and PN 135 dB. The purpose was to investigate the effect of acoustic excitation on laminar, transitional and turbulent boundary layers. For this analysis, four distances from the leading edge (500, 550, 600, and 650 mm) were chosen. All signals were recorded at a constant normal distance from the flat plate, specifically at y = 2 mm.

In the case with no acoustic excitation (Figure 7.11a), the time traces at x = 500 mm and x = 550 mm, where laminar flow is observed, exhibit large-scale low-frequency fluctuations. At the distance x = 600 mm, an increase in both the amplitude and frequency of flow fluctuations is observed. This signal exhibits a transitional flow that is confirmed by the curve of the shape factor distribution in the range of 575 – 650 mm. At x = 650 mm, the time traces indicate nearly turbulent flow, which is confirmed by the shape factor value approaching H = 1.5.

During active acoustic excitation, a combination of high-frequency disturbances and low-frequency instabilities can be observed consistently at 500 mm and 550 mm for all types of acoustic excitation. In the case of monoharmonic forcing (Figure 7.11d), the signal exhibits periodicity that coincides with the generated frequency (110 Hz). In all cases, however, there are no signs of flow breakdown. At a distance of 600 mm, a clear amplification of signal fluctuations is evident. At 650 mm, the time traces for all cases demonstrate a similar highly perturbed flow pattern, indicating that the transition to turbulence is nearing completion. This finding aligns with the observed trend of the shape factor presented in Figure 7.10a.

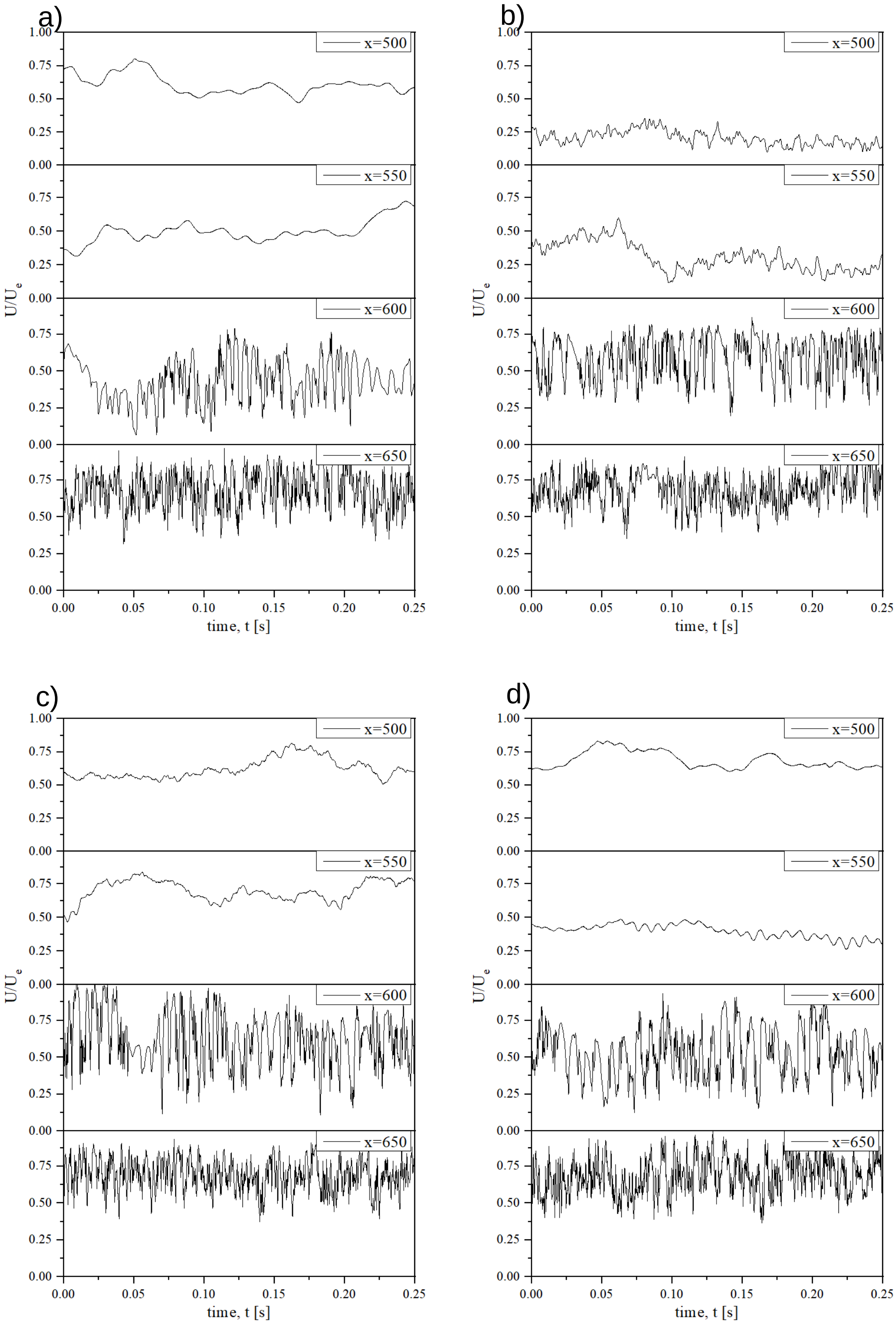

Figure 7.11 non-disturbed flow (a), pink noise 135 dB (b), pink noise 125 dB (c), monoharmonic excitation 125 dB (d)

Figure 7.12 presents the intermittence function for the considered cases at a velocity of 10 m/s. As can be seen in the case without acoustic excitation, the ramp-up of the intermittence function begins at *x* = 575 mm, indicating the onset of l-t transition. This finding is in line well with the previously analysed boundary layer parameters, particularly the shape factor.

In the cases of acoustic excitation with PN 125 dB and Sin 125 dB, notable the same trend of distribution, including the same ramp-up location at *x* = 550 mm and the overlapping of the intermittence functions is noticed. Analysis of the distribution of these two functions shows that both types of excitation (monoharmonic and broadband) have the same effect on the position of the l-t onset, and on l-t termination. However, it is worth noting that although the shape factor analysis indicated an earlier transition with the use of a monoharmonic signal, the intermittence function does not fully reflect this observation. This may be due to the insufficient density of the measurement on the *x*-axis.

In the case of PN 135 dB, an unexpected shape of the intermittence function is observed. In the range from *x* = 400 to *x* = 550 where laminar flow is expected, gamma equals ~ 0.1, and function is not reached value 1 in the area of turbulent flow. This can be attributed to the high sound pressure level and their influence on the measurement, as a result. A detailed description of the intermittence function algorithm can be found in Appendix 1.

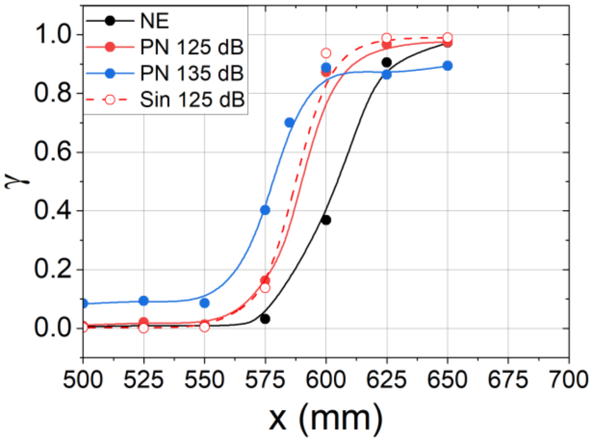

Figure 7.12 Intermittency distribution (test case 10 m/s)

Based on the analysis of the boundary layer parameters presented in this chapter, it is possible to define the significant stages in the development of the separated bubble. The schematic representation of the bubble size is depicted in Figure 7.13. Furthermore, Table 7.3 illustrates the precise positions of the key stages observed during the separated bubble development process.

Table 7.3 Separation bubble characteristics (case 5 m/s)

U_{in} (m/s)	Test case	x_S (mm)	x_t (mm)	x_T (mm)	$x_T - x_t$ (mm)	x_r (mm)
10	NE	550	575	650	75	600
	PN 125 dB	550	550	625	75	–
	Sin 125 dB	550	550	625	75	–
	PN 135 dB	–	550?	–	–	–

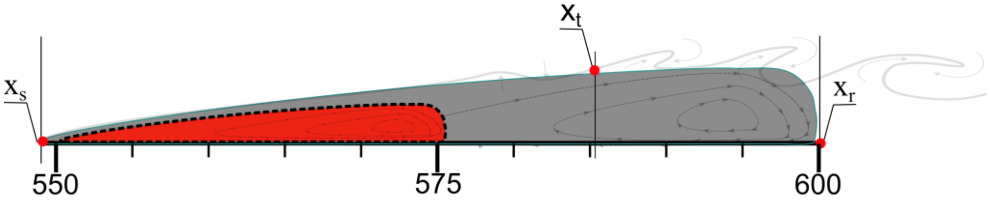

Figure 7.13 Scheme of LSB dimensions (10 m/s case)

7.4. Analysis of the mechanism responsible for the development of laminar separation

7.4.1 Naturally developing separated boundary layer

The above sub-section has shown how acoustics affect the position and size of the separation bubble. An important point, however, is to try to clarify what is the mechanism responsible for the observed changes in the flow. The starting point are the conclusions formulated for undisturbed flow and presented in Chapter 7.1. Literature studies indicate that the l-t transition, in a separated shear layer, can result from the presence of T-S waves, spanwise waves (Klebanoff mode), and Kelvin-Helmholtz instability. The T-S instability is usually associated with the l-t transition of the attached boundary layer (Schlichting & Gersten, 2000). However, some recent studies suggests that this instability mechanism may also play a significant role in the breakdown to turbulence in separation bubbles (Marxen et al., 2004, 2012; McAuliffe & Yaras, 2005) For example, McAuliffe & Yaras, (2008), in their numerical study, confirmed T-S instability growth rate within the boundary layer prior to separation. This instability was also present in the separated shear layer, which then evolved into discrete vortex structures, which is typical of Kelvin-Helmholtz instability. Authors concluded that the breakdown to turbulence was mainly due to the last mechanism. These calculations were carried out for a very low turbulence intensity level of 0.1%, where there is a high chance of T-S wave development. In the current study, however, in the thesis the inlet turbulent intensity is of the order of 1%, so the presence of T-S waves can be excluded.

At elevated levels of free-stream turbulence, low-frequency disturbances penetrating the laminar boundary layer can undergo algebraic growth leading to the formation of elongated streamwise streaks called Klebanoff mode. This mode is fundamentally different from T-S waves as it characteristic features is its low frequency and spanwise length scale of a few boundary layer thicknesses. Balzer & Fasel, (2016) conducting DNS calculations investigated the effect of turbulence level in the free stream on the boundary layer separation. They confirmed the presence of Klebanoff mode even for very low *Tu* levels of the order of 0.05 – 0.5%, without, excluding the possibility of a T-S module. They noted, however, that for that conditions the Klebanoff modes are quite weak and are not connected directly with the breakdown to turbulence. In the experiments by Istvan & Yarusevych, (2018) the streaks forming upstream of separation were also observed for the flow over NACA0018 airfoil in low and medium/high freestream turbulence environment (*Tu* = 0.51 – 1.99%). For elevated levels of turbulence intensity, Balzer & Fasel, (2016) as well as other authors (Hosseinverdi et al., 2012; Simoni et al., 2012), despite the presence of the Klebanoff mode, pointed to another dominant mechanism, i.e. Kelvin-Helmholtz instability.

The first question to be answered in this part of the thesis is whether the characteristic features typical of the Klebanoff mode can be identified in the recorded data, in the region before the transition onset. And if so, how long has this mode been present in the flow. The data already presented in Figure 7.3 (Chapter 7.1) shows that the peak values on fluctuating velocity components, in the pseudo laminar BL and fore part of LSB, are located at a δ^* distance from the wall which, suggests according to the literature (Matsubara & Alfredsson, 2001), that this can be the signature of the Klebanoff streaks.

To clarify the phenomenon occurring in the boundary layer a spectral analysis of the velocity signal for NE conditions has been performed. Figure 7.14a presents, premultiplied by frequency, the PSD of the near-wall velocity at several streamwise locations (x = 400 – 650 mm) for the lower Reynolds number, while Figure 7.17b presents the PSD of the near-wall velocity for the higher Reynolds number.

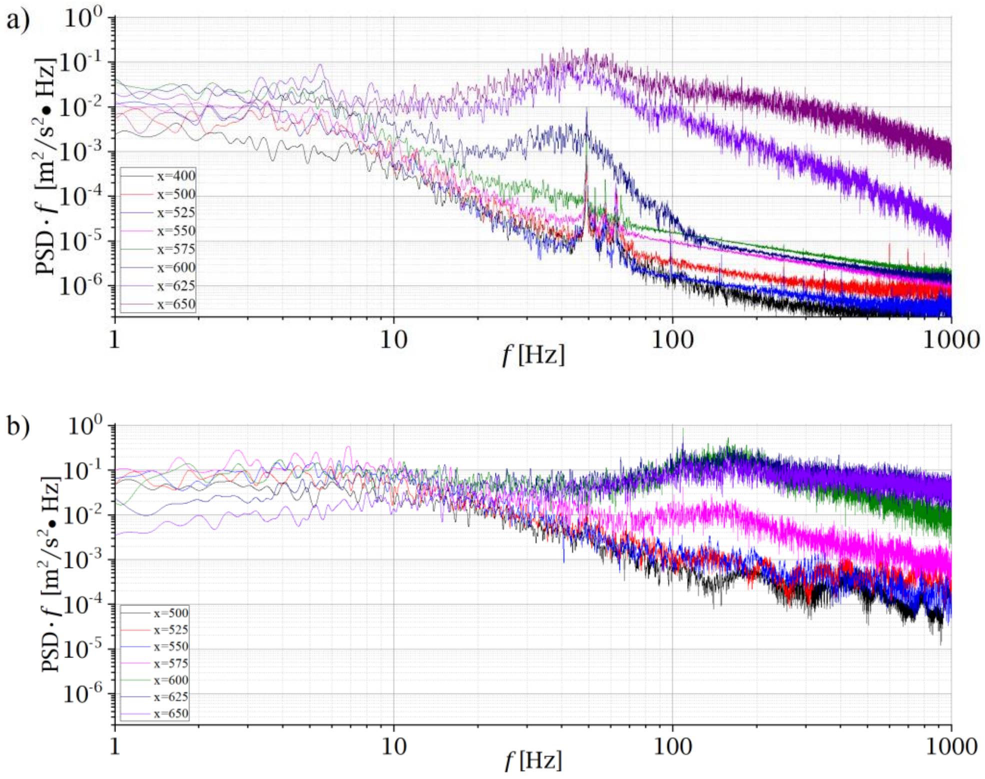

Figure 7.14 PSD of undisturbed test cases 5 m/s (a) and 10 m/s (b)

Before a general assessment of the spectral distributions, attention will be given to the phenomena observed in Figure 7.14a for the frequency range f = 1 – 10 Hz. PSD graphs confirms that the low-frequency events are responsible for a significant part of energy in laminar and separated flow regions. It can be assumed, based on the literature (Lengani et al., 2017; Schlatter et al., 2008) that these low-frequency fluctuations indicate the presence of Klebanoff streaks in the pseudo-laminar boundary along the flat plate.

To confirm this assumption, the average wavelength, λ_K, of Klebanoff streaks was estimated using the correlation by Lengani et al., (2017). The average Klebanoff wavelength equals $\lambda_K = K\delta^*_{\mathrm{ref}}$, where K is a wavelength expressed in local displacement thickness and δ^*_{ref} is the boundary layer displacement thickness at the location, where the streaky structures become to grow (x = 500 mm). The coefficient K = 10.5 in the formula, as characteristic of low- speed streaks, was adopted based on the investigation performed for flat plate flows presented by Lengani et al., (2017). Other numerical and experimental works (Schlatter et al., 2008) indicate that this coefficient can be in a very wide range, even 9 – 20. With the mean value of u' for the consecutive traverses, 400 mm, 500, 550, approximately equal to u' = 0.12, 0.15 and 0.21 m/s, the average frequency ($f = u'/\lambda_K$, Hz) of Klebanoff streaks for a lower *Re* is estimated as: f = 8.2, 5.8 and 5.3 Hz. This estimation is in good agreement with energy content of low-frequency band (f = 1 – 10 Hz) in Figure 7.14a. A similar analysis performed for the higher *Re* number indicates that the average frequency of Klebanoff streaks can be estimated at f = 38, 34 Hz and 24 Hz.

As this estimate has a large uncertainty due to the arbitrary adoption of the K factor of 10.5 as well as the mean values of u', and after detailed analysis of the PSD spectra it was decided, in the following analysis, to assume that the Klebanoff mode be present in the range 1 – 10 Hz for the lower *Re* and in the range 1 – 30 Hz for the higher *Re*. From this frequency range, the u' value denoted as u'_{K} for all traverses was than determined and shown in the Figure 7.15 as solid blue marks with a dashed line. Figure 7.15a presents u'_{K} for test case 5 m/s and Figure 7.15b for case 10 m/s, as well as the $u'_{\mathrm{K-H}}$ (the u' of Kelvin-Helmholtz instability) with superimposed overall u' distributions for both cases. Proceeding downstream from the leading edge, a distinctly large (dominant) energy emerges at low frequencies band. These low-frequency modes amplify after the shift from favourable to adverse pressure gradient at x = 400 mm. However, this large scale, low frequency disturbances begin to diminish, before the l-transition point, i.e. for x = 600 mm for the lower *Re* and for x = 550 mm for the higher Re. From that points the higher frequency phenomena start to dominate (the u'_{K-H} shown by the red line).

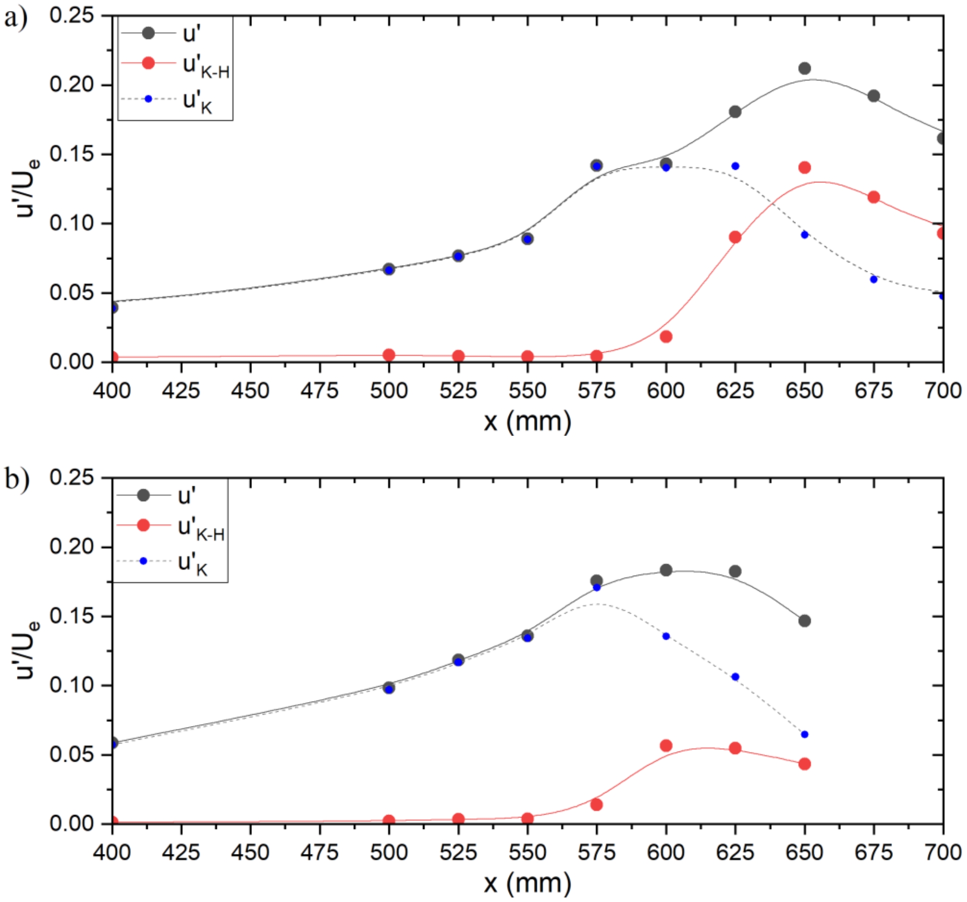

Figure 7.15 u' distributions for undisturbed cases 5 (a) and 10 (b) m/s

Looking at the PSD, for the low Re (Figure 7.14a), for the $f > 10$ Hz, initially (x = 525 and 550 mm) the energy is concentrated in a very narrow frequency range ~48 Hz, where the Strouhal number of the vortex shedding based on the momentum thickness and the velocity at the separation point (Eq. 14) equals 0.007. It should be borne in mind that the Strouhal number being in the range St = 0.005 – 0.011, (Yang & Voke, 2001) and St = 0.008 – 0.012 (Talan & Hourmouziadis, 2002), suggests the presence of the Kelvin-Helmholtz instability. It can therefore be assumed that in the case under consideration, taking additionally the narrow bandwidth of the excited frequency, we are dealing with this type of instability. At further streamwise locations (from x = 600 mm), there is an significant increase in energy over a broad bandwidth, but with a still visible maximum at around 48 Hz. In subsequent traverses a strong increase in the energy level of fine scales is observed, characteristic of transitional flow. To confirm these observations, the *u'* value in the 30 – 70 Hz band (u'_{K-H}) for all traverses was determined and additionally plotted in Figure 7.15 as solid red marks. It is evident that K-H instability appears even before the onset of the l-t transition and then quickly begins to dominate the flow.

$$St = f * \theta / U \qquad \textit{(Eq. 14)}$$

The above analysis indicates that in the range *x* = 525 – 650 mm both instabilities are present, however, from about *x* = 600 Klebanoff mode clearly weakens while the energy contribution associated with the K-H instability increases. It can therefore be hypothesised that the breakdown of the flow to turbulence in the separated shear layer is caused by the latter mechanism mainly.

In the case of higher Reynolds numbers similar variability in the energy contribution of low-frequency events is apparent. The low-frequency modes amplify after the shift from favourable to adverse pressure gradient at *x* = 400 mm. Then this large scale, low frequency disturbances begin to diminish from *x* = 550 mm i.e. before the l-transition point. From that points higher frequency phenomena start to dominate.

Looking at the PSD, for the higher *Re* case (Figure 7.14b), for the *f* > 30 Hz the flow picture is a bit different. In the range *x* = 525 and 550 mm there is a lack of narrow band peak and only for *x* = 575 mm there is a noticeable increase in energy across a wider range of frequencies, with a prominent peak centred around 155 Hz. This frequency corresponds to the Strouhal number St = 0.0086 and also falls within the range typical of the Kelvin-Helmholtz instability. As the flow progresses further downstream, the locations such as *x* = 600 and 650 mm, there is a continued amplification and then redistribution of energy across a broader bandwidth, however, with a still visible maximum at the characteristic frequency of 155 Hz.

The above analysis indicates that in the range *x* = 575 – 600 mm both instabilities are present, however, from 575 mm Klebanoff mode clearly weakens while the energy contribution associated with the K-H instability increases (see u'_{K-H} distribution in Figure 7.15b). It can therefore be hypothesised that also for this case the breakdown of the flow to turbulence in the separated shear layer is caused by the latter mechanism mainly.

7.4.2 Separated boundary layer under acoustic forcing

Chapters 7.2 and 7.3 describe how acoustics affect the global flow statistics and characteristic points of the separation bubble and the location of the l-t transition. In the following section, an analysis of the effect of acoustics on the two flow instabilities present in the undisturbed boundary layer will be presented, which causes the global changes discussed in the two chapters above.

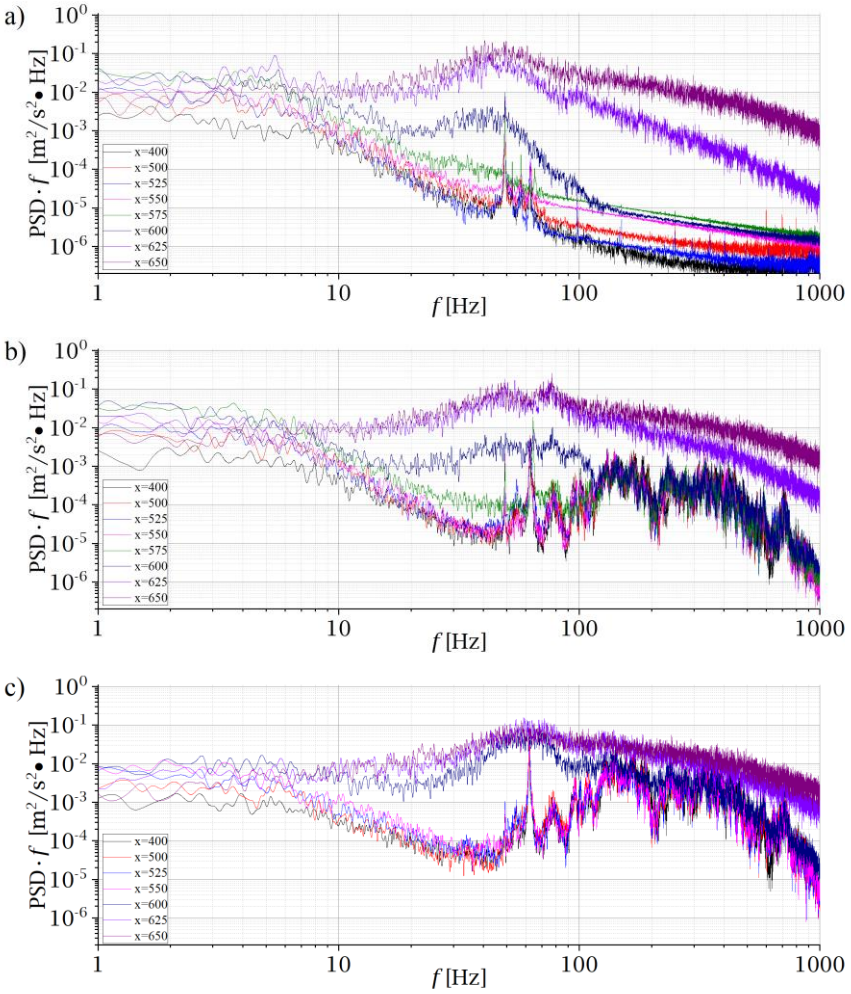

Figure 7.16 PSD of test cases 5 m/s with noise excitation NE (a), PN 125 dB (b), PN 135 dB (c)

Figure 7.16 presents, premultiplied by frequency, the PSD of the near-wall velocity at several streamwise locations (*x* = 400 – 650 mm) for the lower Reynolds number, while Figure 7.17 presents the PSD of the near-wall velocity for the higher Reynolds number. For comparison, these compilations also include spectra for the NE which are treated as the reference case.

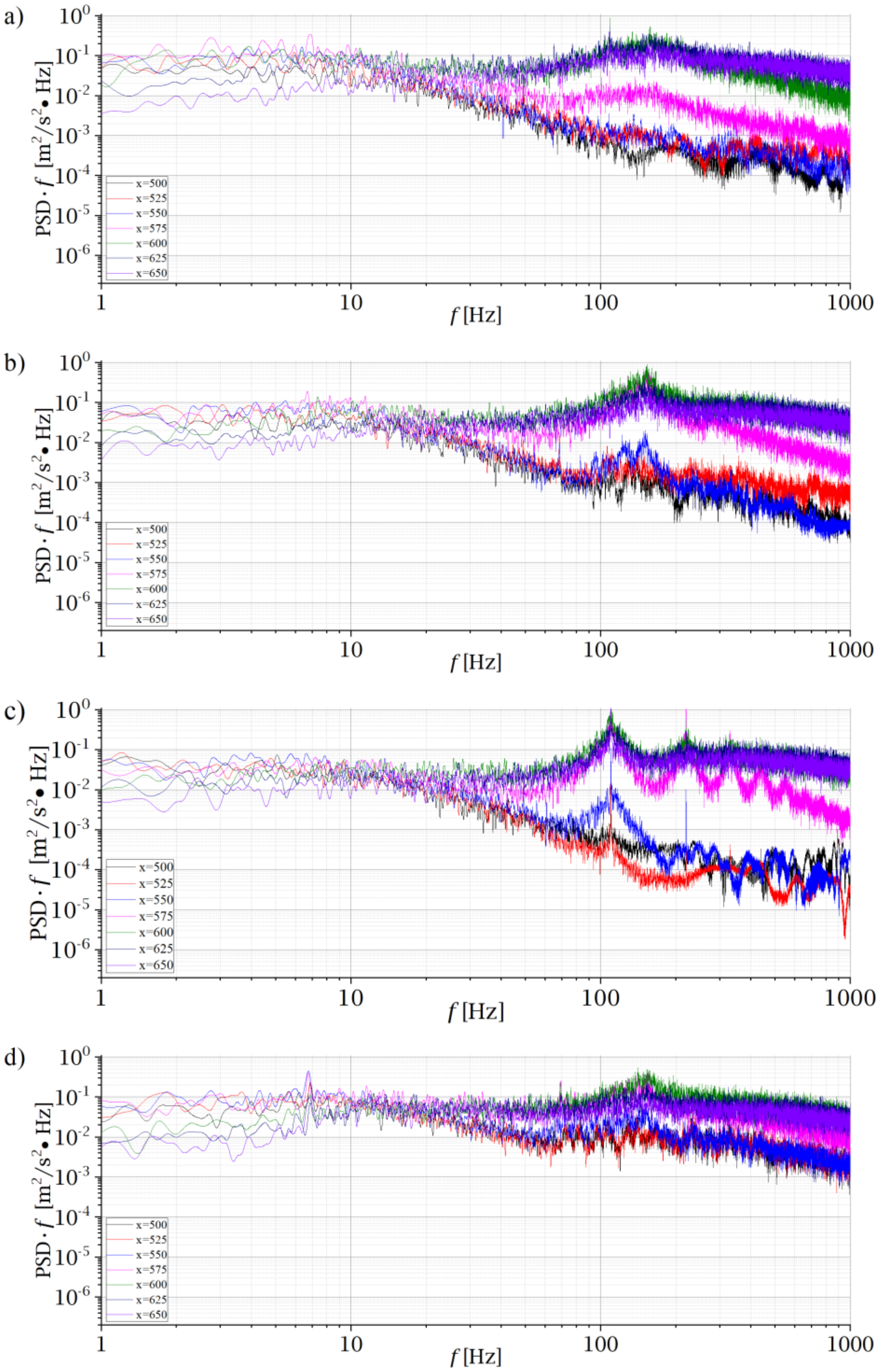

Figure 7.17 PSD of test cases 10 m/s with noise excitation NE (a), PN 125 dB (b), Sin 125 dB (c), PN 135 dB (d)

For the lower Reynolds number the acoustic forcing is applied in the range of 100 – 650 Hz, and this is clearly reflected in the spectra from the pseudolaminar boundary layer region (x = 400 – 550 mm). In the transition and turbulent boundary layer, this effect is already covered by the energy from the developing small–scale turbulence. In the low-frequency range (1 – 10 Hz), characteristic of the Klebanoff mode, a certain influence of the acoustics can be observed. This is confirmed by the analysis of the u'_K distributions shown in Figure 7.18. While, indeed, the effect of an acoustic forcing of SPL = 125 dB is almost negligible, a significant drop in the energy contribution in this frequency band is, however, apparent already for 135 dB. In both cases, however, this large-scale, low-frequency disturbances begin to diminish, before the I-transition point. The drop in u'_K occurs well before for higher SPL. Then the higher frequency phenomena start to dominate. In particular, in the later stages of LSB development (x = 525 and 550 mm), frequencies around 64 Hz are amplified Figure 7.16. This frequency corresponds to a Strouhal number around 0.009 and can also be associated with the Kelvin-Helmholtz instability (Talan & Hourmouziadis, 2002; Yang & Voke, 2001), which is stimulated by broadband noise.

Note that a similar effect was reported by Kurelek et al., (2018), however in their case the broadband acoustic excitation with the frequency range including the frequency of most amplified disturbances of the unperturbed flow was developed. The role of the Kelvin-Helmholtz instability was confirmed by the distribution of the u'_{K-H} shown in Figure 7.18. The current analysis shows that similar effect is observed with broadband acoustic forcing employed with the higher frequency range (f = 100 – 650 Hz) than the frequency of the unperturbed flow instability mechanism (f = 48 – 64 Hz). The physical mechanism of this phenomenon is not entirely clear, but it can be assumed that there is coupling of the sub-harmonic forcing generated by acoustics to the natural frequency of the K-H instability.

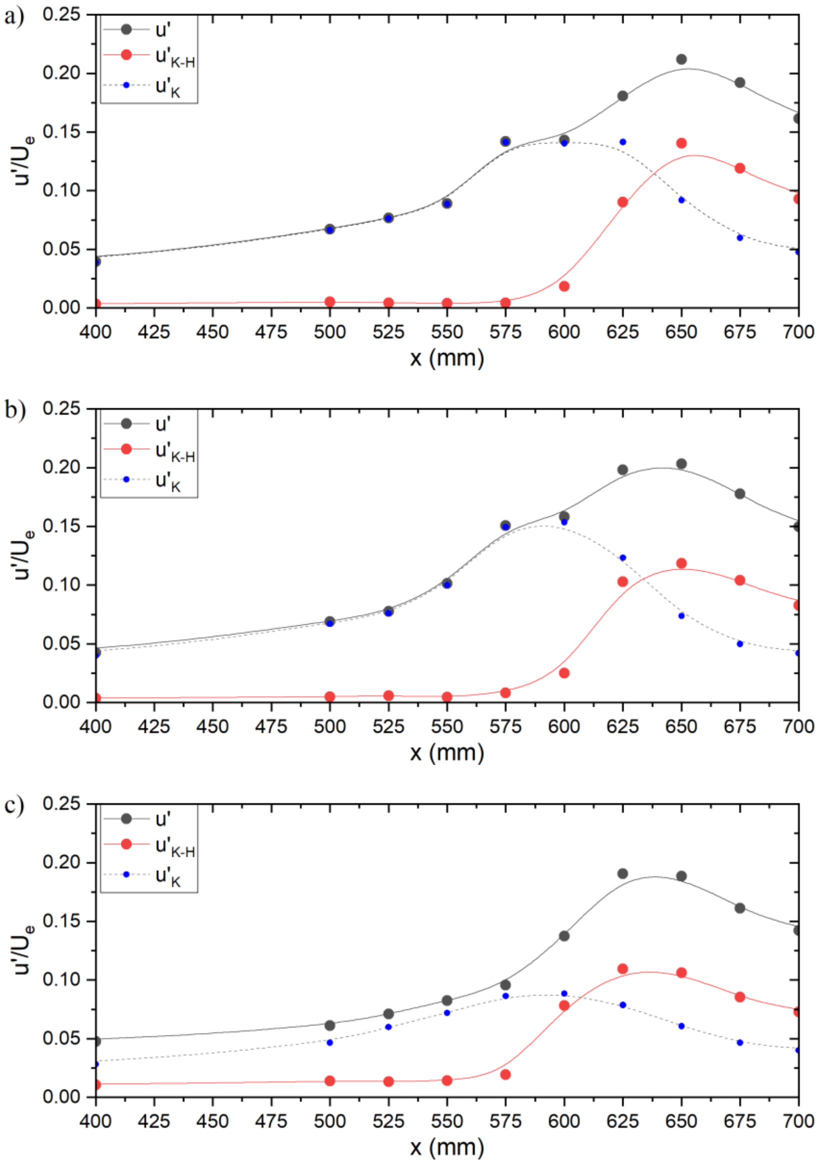

Figure 7.18 Distribution of maximum fluctuation *u'* test case 5 m/s, NE (a), PN 125 dB (b), PN 135 dB (c)

For the higher Reynolds number the acoustic forcing was also applied in the range of 100 – 650 Hz (see Figure 7.17b and Figure 7.17d), and this is also clearly reflected in the spectra from the pseudolaminar boundary layer region (x = 400 – 550 mm). A separate case is the use of harmonic forcing (see Figure 7.17), which will be discussed later. The weak effect of acoustics on the Klebanoff mode was also confirmed for the higher *Re*, by not significant changes in u'_K, as shown in Figure 7.19. For that case, the acoustic frequency band forcing (f = 100 – 650 Hz) covers the natural frequency of the shear layer instability (f = 155 Hz).

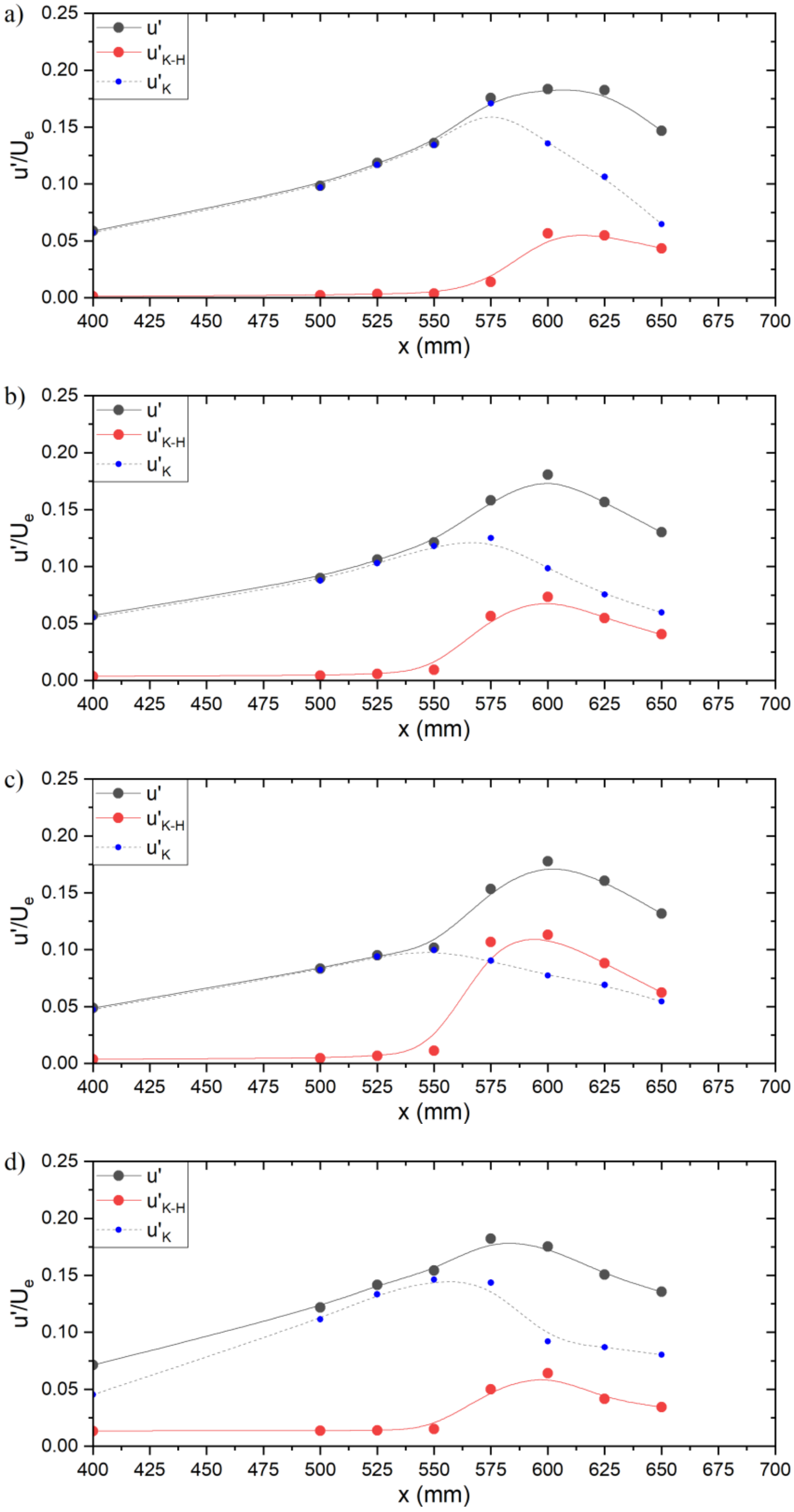

Figure 7.19 Distribution of maximum fluctuation *u'* test case 10 m/s, NE (a), PN 125 dB (b), Sin 125 dB (c), PN 135 dB (d)

A pronounced resonant enhancement of the natural frequency in the flow and acceleration of the l-t transition is evident, especially for SPL = 125 dB

(Figure 7.17b). For a higher value of SPL (Figure 7.17d), the level of transmitted acoustic energy is so high that for *x* = 500 – 650 mm a rapid increase of PSD occurs over the entire frequency range. In the later stages of LSB development (*x* = 575 – 650 mm), frequencies around 155 Hz are amplified. This frequency corresponds to a Strouhal number around 0.0078. So, in this case, it may also be concluded that the l-t transition is due to the Kelvin-Helmholtz instability. Although, indeed, very strong acoustic forcing for an SPL of 135 dB also has a damping effect in the 90 – 170 Hz frequency band.

The final part of the analysis concerns the comparison of the impact of pink noise and the monoharmonic signal forcing. As already presented in Chapter 7.3, in spite of the equivalent energy input levels are, there is no noticeable difference observed as the effect of broadband acoustic excitation and tonal forcing on the parameters of separated shear layers. Both types of acoustic excitation lead to the same upstream shift in the l-t onset, resulting in an earlier reattachment of the flow. This observation is supported by the consistent distribution of shape factor, skin-friction coefficient, as well as intermittency function.

Analysis of the PSD plots (Figure 7.17 b, c) reveals however, a clear difference in spectra for both cases. This applies in particular to the rear part of the separated bubble (*x* = 575 mm and 600 mm), where unlike pink noise the tonal excitation amplifies several harmonic frequencies. This effect can be attributed to the enhanced sensitivity of the rear part of the separated bubble to tonal excitation. For the first harmonic the energy is concentrated within a narrow frequency range centred around *f* = 110 Hz. The Strouhal number associated with this frequency equals 0.0069, which also suggests the presence of the Kelvin-Helmholtz instability. On the other hand, broadband acoustic excitation with pink noise amplifies disturbances across the entire frequency range (100 – 650 Hz), leading to the initial growth of unstable disturbances in the flow at earlier stages of boundary layer development concentrated near the frequency 155 Hz.

Table 7.4 summarises the frequency and determined *St* values for all cases analysed. It should also be noted (Figure 6b and c) that tonal forcing results in a stronger amplification of the K-H instability and, as can be supposed, organises somehow the generation of rollup structures. In contrast, such an effect is not observed for Klebanoff instability, which is characterised by much larger scales. In both cases, irrespective of the different input energy distributions, there is a rapid redistribution of energy in the last phase of the l-t transition to a wide frequency range, leading to termination of the l-t transition process and reattachment of the boundary layer, as shown in Figure 7.10 (Chapter 7.3).

To summarise this section, the comparison of the effects of broadband and tonal forcing, at equivalent SPLs, reveals distinct differences in PSD spectrum, mode enhancement, and the sensibility of the separated bubble. A Similar conclusions, although using a much lower SPL = 96 dB, was presented by Kurelek et al., (2018). They found that tonal excitation results in transition being dominated by the excited mode and damps the growth of all other disturbances. It has the most distinct effect on the development of the K-H type shear layer vortices. For the broadband excitation the amplitudes were more moderate for the natural and broadband frequencies. Finally, however, as in the case discussed in the thesis, tonal and broadband excitation can produce equivalent changes in the mean separation bubble topology.

Table 7.4 Observed frequency and Strouhal numbers

U_{in} (m/s)	Acoustic excitation	*f* (Hz)	*St*
5	NE	48	0.007
	PN 125 dB	64	0.0094
	PN 135 dB	64	0.0097
10	NE	155	0.0086
	PN 125 dB	155	0.0087
	PN 135 dB	155	0.009
	Sin 125 dB	110	0.006

It can be concluded that for all analysed cases (both for natural flow and with acoustic forcing) at a larger portion of LSB, the Klebanoff distortions dominate, but in the background, a distinct frequency characteristic of the K-H mode starts to rise and at the rear part of LSB begins to dominate the flow. It therefore appears that Klebanoff mode do not reach a sufficiently high amplitude to become seat for bypass transition. Instead, the K-H mode is the dominant trigger for the breakdown of the flow.

An application of acoustic forcing, in the frequency range f = 100 – 650 Hz, enhanced the natural flow instability and advanced the l-t transition. An important observation was that the effect of acoustic excitation on the separation point was hardly noticeable, while earlier, laminar – turbulent transition, reattachment point and decrease in the height of the bubble was observed. It is found that tonal excitation has influence on the development of shear layer vortices, exhibiting distinct effects on their characteristics. The organized and synchronized behaviour of vortices induced by tonal excitation results in coherent structures that are observed in rear part of separated bubble (the first harmonic). They further contributing to the overall stability of the shear layer. It can be concluded that equivalent SPL provides the same impact on the size of separated bubble, but the type of the generated acoustic signal has a significant impact on dominant instability and can change the frequency of vortex shedding.

8. Conclusion

This thesis was aimed at providing an insight into the process of acoustic impact on the laminar separation bubble and the laminar-turbulent process responsible for reattachment of the separated shear layer. Having in mind that in real flow configurations, for example in aircraft engines, noise level inside the aircraft engine is very high, reaching up to SPL = 150 dB an attempt was made to get closer to that conditions by using pink noise at SPL equal 125 and 135 dB, which have not been reached experimentally so far. In addition, for comparison, a mono–harmonic signal with forcing of 125 dB was used for a one given Reynolds number.

To achieve this objective, an extensive experimental study of flat plate flow was conducted for two distinct Reynolds numbers, namely 185 000 and 370 000. To investigate these flows, a subsonic, open circuit wind tunnel equipped with a specially designed test section was employed, as detailed in Chapter 4. The test stand was additionally equipped with a designed and optimized acoustic forcing system, as well as measurement apparatus. The use of hot-wire anemometry technique enabled the acquisition of data with exceptional accuracy and frequency resolution. Accurate measurements using this technology require calibration of the sensor and it was done using the StreamLine Pro Automatic Calibrator, which offers in-situ air velocity calibration in wide range of velocities. The test stand was also equipped with advanced sound field measurement system, which comprises of both flush-mounted and free-field microphones, as well analog-digital amplifier.

Addressing the questions specified in the thesis, it was shown that the Reynolds number has a significant impact on the size of the separated boundary layer. The increase in Reynolds number was found to result in a decrease in the size of the separated bubble, which is consistent with previous studies in the field (Burgmann & Schröder, 2008; Istvan et al., 2018; Istvan & Yarusevych, 2018; Lou & Hourmouziadis, 2000) and many others. Additionally, the Reynolds number also influence the position of important stages in the development of the separated bubble. The assessment of these stages relied on integral parameters of the boundary layer, including H, C_f, δ^*, gamma, and θ, which were further validated through smoke visualization conducted at a lower Reynolds number. Figure 8.1 shows schematically the dimensions of separated bubbles for the lower Reynolds number (in grey) and the higher Reynolds numbers (in red). The diagram illustrates that an increase in the Reynolds number resulted in a downstream shift of the separated bubble onset (x_s) downstream by ~ 20 mm, significant upstream shift of the onset of the laminar-turbulent transition (x_t) by 50 mm as well as the definite change in the reattachment point (x_r) by 40 mm.

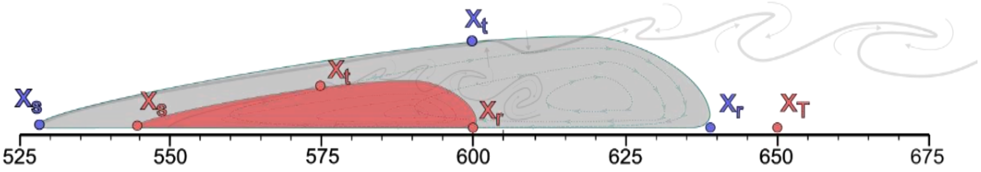

Figure 8.1 Scheme of LSB dimensions (5 and 10 m/s)

Studying the effect of acoustics on separated shear layer development, it was shown such an impact causes a considerable reduction in the thickness and streamwise extent of the separated bubble, or even its complete absence (for the higher *Re*), along with an earlier initiation of the laminar-turbulent transition. Examining the flow statistics and the integral parameters of the boundary layer, it becomes apparent that acoustic excitation leads to a huge effect especially on the rear part of the separated bubble, without a significant effect on the fore, laminar or so-called pseudolaminar part of the separation. In this area, it may be related to the stability of the boundary flow and the insufficient energy of the acoustic excitation to modify the flow topology. Instead, a notable influence on the separated shear layer becomes apparent within the rear part of the separated bubble. This phenomenon was explained as the interaction between sound waves generated by the loudspeaker and the inviscid Kelvin-Helmholtz instability. As a result, a shift of the transition onset upstream of the flow by about 50 mm was observed for the lower *Re* and the higher SPL and by about 25 mm for the higher Re and the higher SPL.

The most important result of the thesis was to clarify the underlying physical phenomena are responsible for the turbulence breakdown in the LSB. The examination of the power spectra supplemented by energy analysis in selected frequency bands (u'_{K} and u'_{K-H}) reveals that, across all analysed cases, including both natural flow and those subjected to acoustic forcing, Klebanoff distortions dominate a substantial portion of the LSB. However, in the background, a discernible frequency typical of the Kelvin-Helmholtz mode begins to emerge and starts to dominates the flow towards the rear part of the LSB. These observations indicate that the Klebanoff mode fails to reach a sufficiently high amplitude to become seat for bypass transition. Instead, the K-H mode is the dominant trigger for the breakdown of the flow. So it is clear that the application of acoustic forcing within the frequency range of 100 – 650 Hz enhances the inherent instability of the natural flow and accelerates the laminar-turbulent transition. However, some differences exist between the two Re cases. For the lower Reynolds number the acoustic forcing was employed with the higher frequency range (f = 100 – 650 Hz) than the frequency of the unperturbed flow instability mechanism (f = 48 – 64 Hz). Despite this, a strong reaction in the separated shear layer was observed. The physical mechanism of this phenomenon is not entirely clear, but it can be assumed that there is coupling of the sub-harmonic forcing generated by acoustics to the natural frequency of the K-H instability. For the higher Reynolds number the acoustic forcing was applied in the same range of 100 – 650 Hz, which in this case covers the natural frequency of the shear layer instability (f = 155 Hz). A pronounced resonant enhancement of the natural frequency in the flow and acceleration of the l-t transition is evident, especially for SPL = 125 dB. For a higher value of SPL, the level of transmitted acoustic energy is so high that in the rear part of LSB the rapid increase of PSD occurs over the entire frequency range. Nevertheless, frequencies around 155 Hz were amplified.

The comparison of the effects of broadband and monoharmonic forcing, at equivalent SPL levels, reveals distinct differences in PSD spectrum, mode enhancement, and the sensibility of the separated bubble. Tonal excitation primarily influences the transition by dominant activation of the excited mode, thereby suppressing the growth of other disturbances. It exerts a pronounced effect on the development of Kelvin-Helmholtz type shear layer vortices.

Conversely, broadband excitation yields more moderate amplitudes for the naturally occurring and broadband–excited flows. Nevertheless, in line with the case discussed in this thesis, both tonal and broadband excitation can result in comparable modifications in the mean separation bubble topology.

In summary, it can be said that the application of acoustic forcing enhances the inherent instability of the natural flow and accelerates the laminar-turbulent transition. Notably, the impact of acoustic excitation on the separation onset is scarcely discernible. However, the effects observed include an earlier onset of the laminar-turbulent transition, a shift in the reattachment point, and a reduction in the height of the separation bubble. Moreover, tonal excitation exerts a notable influence on the development of shear layer vortices, characterized by distinctive effects on their properties. The organized and synchronized behavior induced by tonal excitation results in coherent structures within the rear part of the separated bubble, specifically the first harmonic, contributing to the overall stability of the shear layer. Consequently, it can be inferred that equivalent sound pressure levels (SPLs) produce equivalent effects on the size of the separated bubble.

Future research can take advantage of the developed experimental facility, refined experimental methods, and the insights gained from this thesis to further explore steady transitional separated flows. To enhance our understanding of the impact of acoustic excitation on separated bubble phenomena, the following avenues for investigation are proposed:

- Investigation of Acoustic Frequency Effects: Future studies should delve into the influence of different acoustic frequency ranges on separated bubble dynamics. By systematically varying the frequency of acoustic excitation within a wider range, the resonant frequencies and their effects on the flow characteristics can be identified and analyzed.

- Study of Acoustic Amplitude Effects: It is crucial to explore the effects of varying acoustic amplitudes on separated flows. By carefully adjusting the amplitude of acoustic excitation, the thresholds for flow modification and transition can be determined, shedding light on the underlying mechanisms and potential for flow control.

- Use of new methods of investigation of near flow wall as Particle Image Velocimetry and pressure distribution on the surface of a flat plate. The non–invasive technique gives the opportunity for faster and more detailed research of the boundary layer flow, avoiding resonance of generated noise with measuring aparature.
- Increase the number of measured profiles in the area of the separated bubble. The lack of high–resolution increases the error of indicating important stages of separated boundary layer development, such as separation onset, the onset of l-t transition, and the reattachment point. Which leads to a decrease in the accuracy of determining the effect of acoustic excitation on the flow.

By pursuing these research directions, further advancements can be made in elucidating the intricate interplay between acoustic excitation and separated bubble phenomena, ultimately leading to enhanced control and understanding of transitional separated flows.

9. Appendix 1

To identify precisely the laminar-turbulent region, transition onset, and transition termination in a separated boundary layer the concept of intermittency has been proposed. The intermittency factor (γ) is a measure of turbulence activity in the flow, that ranges from 0 to 1 and indicating a fully laminar flow and a fully turbulent flow, respectively. The initial concept of intermittency was introduced by (Corrsin, 1943) as a means to differentiate turbulent and non-turbulent patterns in axisymmetric turbulent jets. Initially, intermittency was investigated using photographs of hot-wire signals captured on an oscilloscope screen (Schubauer & Klebanoff, 1956) aimed to identify the number of turbulent spots. Later, Hedley and Keffer (1974) proposed a computer-based method for intermittency identification that consists of four sequential steps:

1. Detector function D(t): This step involves distinguishing laminar and turbulent parts of the flow by "sensitizing" the signal. The time derivative of the velocity signals is commonly used as the detector function.
2. Criterion function: In this step, the second derivative of the signal is smoothed to avoid turbulent dropouts and spurious signals in laminar flow.
3. determination of threshold value (T_h): This step involves determining the threshold value, which has a significant impact on the identification of the number of turbulent spots. Several techniques have been proposed to standardize this process, but there is still no universally accepted algorithm.
4. Indicator function I(t): In this step, an indicator function, I(t), is assigned. The function assigns a value of 1 for every sample in the spot area and a value of 0 for every sample in the remaining part of the signal.

Determining the threshold value is a critical step in the identification of the onset and end of turbulent transition in the boundary layer. As previously mentioned, several algorithms have been proposed for determining the threshold value, but there is still no universally accepted method.

Typically, the threshold value is based on the mean square deviation of the second derivative of the signal at the point where the first signs of turbulence in the flow can be observed. It is important to note that the presence of flow turbulence has a significant influence on the value of the root mean square deviation, particularly in detached boundary layers where the Kelvin-Helmholtz instability is present. The presence of such instability impacts the total fluctuation in the analysed area. Transitional boundary layer research involves a variety of methods for calculating intermittency, including TERA, MTERA, dual-slope, and Probability Density Function (PDF). The TERA method, proposed by Falco and Gendrich (1988), and the MTERA method, introduced by Zhang et al., (1995), determine the intermittency threshold based on a predetermined percentage of the u' value of a specific criterion function.

The dual-slope method, first introduced by Kuan and Wang (1990) employs a graphical approach to determine the T_h value. This method plots the cumulative frequency distribution of the sensitised transitional signal against the detector function, with the intersection point between two distinct slopes representing the threshold. Although some researchers have successfully employed the dual-slope method, such as Ramesh et al., (1996) and Jahanmiri et al., (1997), others, like Canepa et al., (2002) and Fransson et al., (2005), have encountered difficulties in identifying the two slopes. Additionally, the subjective nature of the graphical approach can lead to variation in selecting the threshold value. Despite these limitations, the dual-slope method remains widely used in transitional flow studies.

It is worth mentioning the work of Veerasamy and Atkin (2020), in this work tried to propose a rational method for determining intermittency in the transitional boundary layer. Their method was used partly in the present thesis, the incomplete efficacy of the method can potentially be the presence of Kelvin-Helmholtz (K-H) instability in the flow and high SPL excitation.

All of the above-mentioned methods for determining the threshold value have their own shortcomings and considerations, each of these methods can be applied, but none of them serve as a generalised method for determining a threshold value. The peculiarity in case considered in the thesis is related to the acoustic forcing applied and to the detached boundary layer, where the level of fluctuation can be dependent on Kelvin-Helmholtz instability. Given the unusual experimental conditions for calculating T_h, a graphical method was chosen. The definition of the relevant level of T_h is based on the calculation of the Intermittency level for different values of the threshold value, after which the interference distribution is compared with each other. Than the minimal value of T_h for which distribution of interpretation can be observed in the range from 0 to 1 is selected. Threshold selection was done out for the lower Reynolds number and for the case without forcing. Figure 9.1 presents intermittency distributions for same test case (5 m/s NE) but with different T_h.

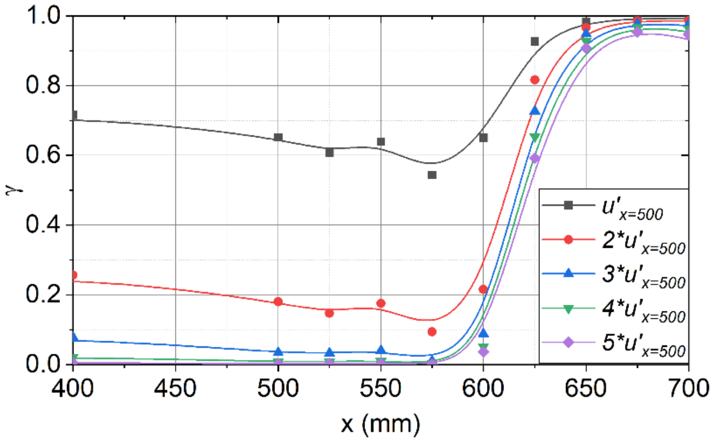

Figure 9.1 Distribution of intermittency

To avoid the region of the separation bubble, *u'* from the position x = 500 was used to define the T_h value. As can be observed on Figure 1, only 4*$u'_{x=500}$ would meet the requirements of the T_h choice. The same procedure was repeated for all other cases, demonstrating the validity of this method.

The following paragraph contains the description of main stages of calculation procedure.

Detection function.

The first step in detecting intermittency is the process of sensitizing, which is a well-known procedure that has been used in previous investigations. The aim of this procedure is to eliminate the perturbations caused by turbulent spots, by sensitizing the signals through double differentiation with respect to time and then squaring the result $(d^2u/dt^2)^2 = D(t)$. This approach amplifies the high-frequency signals, which are typically due to turbulent spots, and enables them to be clearly distinguished from the laminar perturbations.

```
def Derivative(x, y):  # x- time, y – U [m/s]

    dx = np.diff(x, 1, axis=0)
    dx = np.append(dx, [np.array([1])]).reshape(len(x), 1)

    y1 = np.append(y, np.array([0]))
    y1 = np.delete(y1, 0).reshape(len(y1) - 1, 1)

    y2 = np.append(np.array([0]), y)
    y2 = np.delete(y2, -1).reshape(len(y2) - 1, 1)

    diff1 = np.subtract(y1, y)

    diff2 = np.subtract(y, y2)

    add = np.add(diff1, diff2)

    diff = (add / dx) * 0.5

    return diff
```

Script 1 Derivative

To calculate the intermittency function, a custom code was created using the Python language and the standard libraries available for this coding language.

The Script 1 requires a signal consisting of two columns time and velocity to be added using standard *Python* functions and the open *“NamPy”* library. The script returns the first derivative of the signal, and to calculate the second derivative, the script has to be run again using the signal of first derivative created in the first run.

The second derivative signal is then squared to amplify the high-frequency oscillations in the signal, which enables the identification of turbulent spots. This procedure is conducted for single point from each measured velocity profile along the flow.

Criterion function.

The criterion function is then applied to the signal, using the "*uniform_filter1d*" function from the "*SciPy*" library. This procedure smooths the signals to avoid turbulent dropouts and spurious signals (laminar spikes) being considered during the analysis. The filtered signal is then compared to a threshold value, and values that exceed this threshold have been assign as turbulent spots.

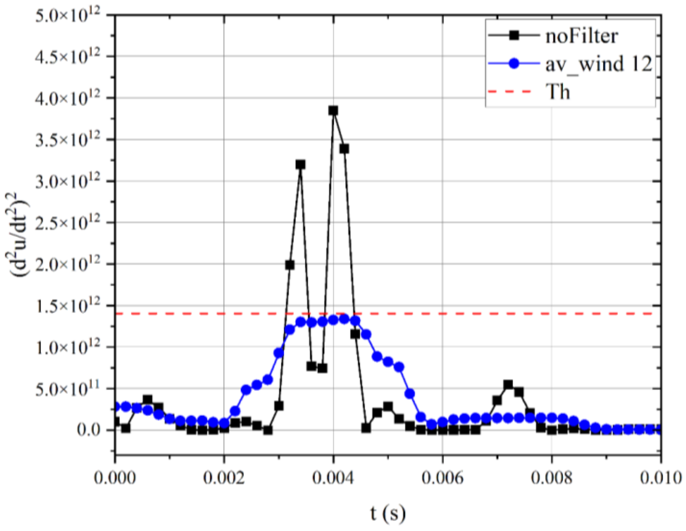

Figure 9.2 2$_{nd}$ derivative of velocity signal

In Figure 9.2, can be seen that after smoothing the signal with an averaging window of 12 samples, the values of the filtered signal do not exceed the threshold value. The window of averaging should be chosen based on acquisition frequency and Kolmogorov time scale, in cases present in this work 12 samples equal $12 * \Delta t = 12 * 0.0002\,s \approx 0.0024\,s$ what is approximately 50 times the Kolmogorov time scale. This parameter is choosing in the beginning of the script (Script 3)

```
def intermittency (x, y, sens, adding_points):

    s = 0
    spots_production_rate = 0
    number_of_samples_in_spot = []
    indicator_function = []
    for i in range(len(x) - 1):

        number_of_samples_in_spot_varible = 0
        try:

            if all(val > y for val in x[0:sens]):

                try:
                    spots_production_rate += 1

                    number_of_samples_in_spot_varible += adding_points*2
                    s += adding_points*2

                    for pop in range(adding_points):
                        try:
                            indicator_function.pop()
                        except IndexError:

                            pass

                    for indicator in range(adding_points):
                        indicator_function.append(1)

                    while any(val > y for val in x[0:sens]):

                        number_of_samples_in_spot_varible += 1
                        indicator_function.append(1)
                        s += 1
                        x = np.delete(x, 0)
                except IndexError:

                    pass
                number_of_samples_in_spot = np.append(number_of_samples_in_spot, number_of_samples_in_spot_varible)

                x = np.delete(x, [*range(0, adding_points, 1)])

                for indicator in range(adding_points):
                    indicator_function.append(1)

            else:
                indicator_function.append(0)
                x = np.delete(x, 0)
        except IndexError:
            break
    indicator_function = np.delete(indicator_function, [*range(0, adding_points, 1)])
    return s, spots_production_rate, number_of_samples_in_spot, indicator_function
```

Script 2 Function of intermittency

Indicator function.

The *Indicator* Function serves as a valuable tool in fluid dynamics analysis, facilitating the quantification of turbulent spots within a flow. This algorithm, referred to as Script 2, operates by assigning a value of 0 or 1 to each sample identified as part of a laminar region or a part of the turbulent spot in the signal, respectively.

This algorithm is founded upon two primary equations:

For **$D(t)_x \leq Th, I(t) = 0$**: This equation stipulates that when the value of **$D(t)_x$** is less than or equal to the threshold value Th, the intermittency, represented by **$I(t)$**, is assigned a value of 0. In this scenario, the flow is considered to be laminar.

For **$D(t)_x > Th, I(t) = 1$**: Conversely, this equation dictates that when the value of $D(t)_x$ exceeds the threshold value Th, the intermittency, denoted by $I(t)$, is assigned a value of 1. In this case, the flow is considered turbulent.

In essence, the provided piecewise function outlines a rudimentary binary model characterizing intermittency during the transition to turbulence.

To ensure the high accuracy of the results, the algorithm takes into consideration the threshold value, which is used to eliminate the inclusion of individual samples whose values exceed the threshold but are primarily a result of random laminar fluctuations or noise. To mitigate this issue, only those turbulent spots whose length exceeds a specified window, known as the "*sens*" (Script 3) window, are counted. This parameter is established at the beginning of the programme and is usually based on the Kolmogorov time scale (Veerasamy & Atkin, 2020).

```
av_wind = 12
sens = 10
adding_points = 5
```

Script 3 Parameters of intermittency

As depicted in Figure 9.3, the Indicator Function identifies the presence of a turbulent spot. The threshold value is represented by the blue dashed line, while the red dots signify the samples that are situated within the turbulent spot and are accounted for in the total number of turbulent samples. The empty dots on either side of the spot indicate the samples that have been added, as specified by the variable "*adding_points*" These additional samples are crucial for incorporating the tails of the turbulent spots. It is worth noting that the value of the "*adding_points*" variable can be freely modified within the code.

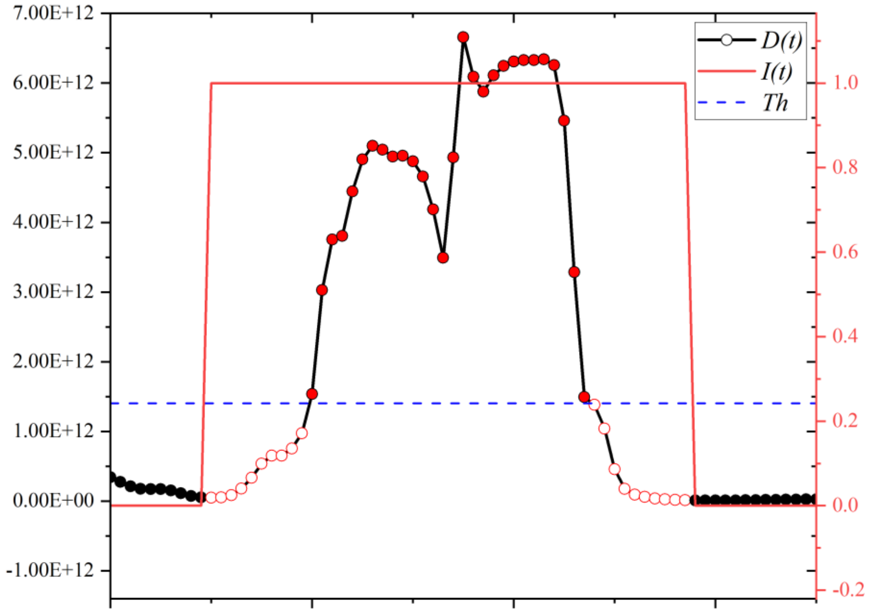

Figure 9.3 The time interval of turbulent spot with the inclusion of supplementary samples.

Upon examination of Figure 9.4, it is clear that the entire algorithm effectively identifies turbulent spots within the transitional flow regime. The graphical representation demonstrates the algorithm's capability to distinguish between laminar and turbulent regions, providing a clear demarcation of the flow characteristics.

The successful identification of turbulent spots can be attributed to the careful selection of the threshold value T_h, which is crucial for accurately differentiating between laminar and turbulent flow samples. Furthermore, the algorithm's robustness in processing the input data, such as the detector function D(t)x, ensures reliable and consistent results.

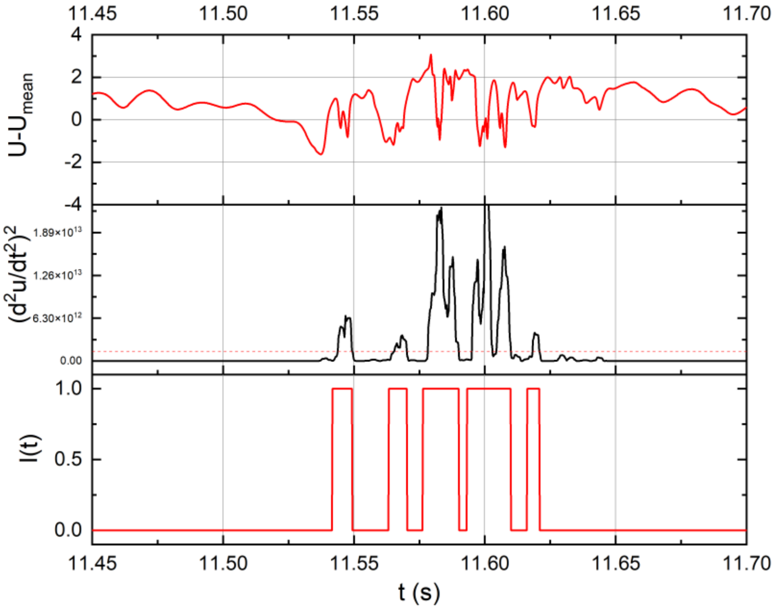

Figure 9.4 Indicator function I(t)

In summary, the algorithm depicted in Figure 9.4 demonstrates a noteworthy ability to identify turbulent spots within the transitional flow regime, providing

List of Figures

List of Tales

10. Bibliography

Abu-Ghannam, B. J., & Shaw, R. (1980). Natural Transition of Boundary Layers—The Effects of Turbulence, Pressure Gradient, and Flow History. *Journal of Mechanical Engineering Science*, *22*(5), 213–228. https://doi.org/10.1243/JMES_JOUR_1980_022_043_02

Açıkel, H. H., & Serdar Genç, M. (2018). Control of laminar separation bubble over wind turbine airfoil using partial flexibility on suction surface. *Energy*, *165*, 176–190. https://doi.org/10.1016/j.energy.2018.09.040

Alam, M., & Sandham, N. D. (2000). Direct numerical simulation of ‘short’ laminar separation bubbles with turbulent reattachment. *Journal of Fluid Mechanics*, *410*, S0022112099008976. https://doi.org/10.1017/S0022112099008976

Arbey, H., & Bataille, J. (1983). Noise generated by airfoil profiles placed in a uniform laminar flow. *Journal of Fluid Mechanics*, *134*, 33–47. https://doi.org/10.1017/S0022112083003201

Atzori, M., Vinuesa, R., Fahland, G., Stroh, A., Gatti, D., Frohnapfel, B., & Schlatter, P. (2020). Aerodynamic Effects of Uniform Blowing and Suction on a NACA4412 Airfoil. *Flow, Turbulence and Combustion*, *105*(3), 735–759. https://doi.org/10.1007/s10494-020-00135-z

Balzer, W., & Fasel, H. F. (2016). Numerical investigation of the role of free-stream turbulence in boundary-layer separation. *Journal of Fluid Mechanics*, *801*, 289–321. https://doi.org/10.1017/jfm.2016.424

Bernardini, C., Benton, S., & Bons, J. P. (2012). The Effect of Acoustic Excitation on Boundary Layer Separation of a Highly Loaded LPT Blade. *Volume 8: Turbomachinery, Parts A, B, and C*, *8*(PARTS A, B, AND C), 1559–1569. https://doi.org/10.1115/GT2012-69618

Boutilier, M. S. H., & Yarusevych, S. (2012). Separated shear layer transition over an airfoil at a low Reynolds number. *Physics of Fluids*, *24*(8), 084105. https://doi.org/10.1063/1.4744989

Burgmann, S., Brücker, C., & Schröder, W. (2006). Scanning PIV measurements of a laminar separation bubble. *Experiments in Fluids*, *41*(2), 319–326. https://doi.org/10.1007/s00348-006-0153-6

Burgmann, S., & Schröder, W. (2008). Investigation of the vortex induced unsteadiness of a separation bubble via time-resolved and scanning PIV measurements. *Experiments in Fluids*, *45*(4), 675–691. https://doi.org/10.1007/s00348-008-0548-7

Canepa, E., Ubaldi, M., & Zunino, P. (2002). Experiences in the application of intermittency detection techniques to hot-film signals in transitional boundary layers. *The 16th Symposium on Measuring Techniques in Transonic and Supersonic Flow in Cascades and Turbomachines*, *September*.

Carmichael, B. H. (1981). Low Reynolds number airfoil survey. *NASA Contractor Report*, *1*.

Cattafesta, L. N., & Sheplak, M. (2011). Actuators for Active Flow Control. *Annual Review of Fluid Mechanics*, *43*(1), 247–272. https://doi.org/10.1146/annurev-fluid-122109-160634

Chong, T. P., & Joseph, P. (2012). “Ladder” structure in tonal noise generated by laminar flow around an airfoil. *The Journal of the Acoustical Society of America*, *131*(6), EL461–EL467. https://doi.org/10.1121/1.4710952

Collins, F. G., & Zelenevitz, J. (1975). Influence of Sound upon Separated Flow over Wings. *AIAA Journal*, *13*(3), 408–410. https://doi.org/10.2514/3.49717

Corke, T. C., Bowles, P. O., He, C., & Matlis, E. H. (2011). Sensing and control of flow separation using plasma actuators. *Philosophical Transactions of the Royal Society A: Mathematical, Physical and Engineering Sciences*, *369*(1940), 1459–1475. https://doi.org/10.1098/rsta.2010.0356

Corrsin, S. (1943). *Investigation of Flow in an Axially Symmetrical Heated Jet of Air*.

Diwan, S. S., & Ramesh, O. N. (2009). On the origin of the inflectional instability of a laminar separation bubble. *Journal of Fluid Mechanics*, *629*, 263–298. https://doi.org/10.1017/S002211200900634X

Dovgal, A. V., Kozlov, V. V., & Michalke, A. (1994). Laminar boundary layer separation: Instability and associated phenomena. *Progress in Aerospace Sciences*, *30*(1), 61–94. https://doi.org/10.1016/0376-0421(94)90003-5

Drela, M. (2014). Flight vehicle aerodynamics. *MIT Press*, *53*(9), 258.

Dróżdż, A., & Elsner, W. (2011). Detection of coherent structures in a turbulent boundary layer with zero, favourable and adverse pressure gradients. *Journal of Physics: Conference Series*, *318*(SECTION 6). https://doi.org/10.1088/1742-6596/318/6/062007

Dróżdż, A., & Elsner, W. (2013). Amplitude modulated near-wall cycle in a turbulent boundary layer under an adverse pressure gradient. *Archives of Mechanics*, *65*(6), 511–525.

Dróżdż, A., & Elsner, W. (2014). Comparison of single and x-wire measurements of streamwise velocity fluctuations in turbulent boundary layer. *Journal of Theoretical and Applied Mechanics (Poland)*, *52*(2), 499–505.

Dróżdż, A., Elsner, W., & Sikorski, D. (2018). Skin friction estimation in a strong decelerating flow. *Journal of Theoretical and Applied Mechanics*, 365. https://doi.org/10.15632/jtam-pl.56.2.365

Eto, K., Kondo, Y., Fukagata, K., & Tokugawa, N. (2019). Assessment of Friction Drag Reduction on a Clark-Y Airfoil by Uniform Blowing. *AIAA Journal*, *57*(7), 2774–2782. https://doi.org/10.2514/1.J057998

Ezerskii, A. B. (1985). *Acceleration of Transition to Turbulence in a Boundary Layer due to the Combination Effect of Sound Waves* (V. V. Kozlov (ed.); pp. 255–260).

Falco, R. E., & Gendrich, C. P. (1988). Turbulence burst detection algorithm of Z. Zaric. *Proceedings of the International Centre for Heat and Mass Transfer*.

Fosas de Pando, M., Schmid, P. J., & Sipp, D. (2014). A global analysis of tonal noise in flows around aerofoils. *Journal of Fluid Mechanics*, *754*, 5–38. https://doi.org/10.1017/jfm.2014.356

Fransson, J. H. M., Matsubara, M., & Alfredsson, P. H. (2005). Transition induced by free-stream turbulence. *Journal of Fluid Mechanics*, *527*. https://doi.org/10.1017/S0022112004002770

Funazaki, K., & Kato, Y. (2002). Studies on a Blade Leading Edge Separation Bubble Affected by Periodic Wakes: Its Transitional Behavior and Boundary Layer Loss Reduction. *Volume 3: Turbo Expo 2002, Parts A and B*, 561–569. https://doi.org/10.1115/GT2002-30221

Gaster, M., & Grant, I. (1975). An Experimental Investigation of the Formation and Development of a Wave Packet in a Laminar. In *The Royal Society* (Vol. 347, Issue A, pp. 253–269).

Glezer, A., & Amitay, M. (2002). Synthetic jets. *Annual Review of Fluid Mechanics*, *34*(1), 503–529. https://doi.org/10.1146/annurev.fluid.34.090501.094913

Goodfellow, S. D., Yarusevych, S., & Sullivan, P. E. (2011). Momentum Coefficient As A Parameter For Aerodynamic Flow Control With Synthetic Jets. *Proceeding of Seventh International Symposium on Turbulence and Shear Flow Phenomena*, 1–6. https://doi.org/10.1615/TSFP7.890

Gostelow, J. P., & Thomas, R. L. (2006). Interactions Between Propagating Wakes and Flow Instabilities in the Presence of a Laminar Separation Bubble. *Volume 3: Heat Transfer, Parts A and B*, *3 PART B*, 1261–1269. https://doi.org/10.1115/GT2006-91193

Häggmark, C. P., Hildings, C., & Henningson, D. S. (2001). A numerical and experimental study of a transitional separation bubble. *Aerospace Science and Technology*, *5*(5), 317–328. https://doi.org/10.1016/S1270-9638(01)01110-5

Hedley, T. B., & Keffer, J. F. (1974). Turbulent/non-turbulent decisions in an intermittent flow. *Journal of Fluid Mechanics*, *64*(4), 625–644.

https://doi.org/10.1017/S0022112074001832

Hosseinverdi, S., Balzer, W., & Fasel, H. (2012). Direct Numerical Simulations of the Effect of Free-Stream Turbulence on “Long” Laminar Separation Bubbles. *42nd AIAA Fluid Dynamics Conference and Exhibit*, *June*, 1–24. https://doi.org/10.2514/6.2012-2972

Hourmouziadis, J. (1989). Aerodynamic design of low pressure turbines. *AGARD Lecture Series*, *167*.

Howell, R. J. (1999). Wake-separation bubble interactions in low Reynolds number turbomachinery. In *Cambridge University Tesis de Doctorado* (Issue January). http://www-g.eng.cam.ac.uk/whittle/publications/rjh/rjh thesis acrobat3.pdf

Istvan, M. S., Kurelek, J. W., & Yarusevych, S. (2018). Turbulence Intensity Effects on Laminar Separation Bubbles Formed over an Airfoil. *AIAA Journal*, *56*(4), 1335–1347. https://doi.org/10.2514/1.J056453

Istvan, M. S., & Yarusevych, S. (2018). Effects of free-stream turbulence intensity on transition in a laminar separation bubble formed over an airfoil. *Experiments in Fluids*, *59*(3), 52. https://doi.org/10.1007/s00348-018-2511-6

Jahanmiri, M., Kumar, S. R., & Prabhu, A. (1997). A method for generating the turbulence intermittency function. *International Journal of Engineering*, *10*(2).

Johansen, J., & Sorensen, J. (1998). Prediction of laminar/turbulent transition in airfoil flows. *36th AIAA Aerospace Sciences Meeting and Exhibit*, *987*(May). https://doi.org/10.2514/6.1998-702

Jones, L. E., Sandberg, R. D., & Sandham, N. D. (2008). Direct numerical simulations of forced and unforced separation bubbles on an airfoil at incidence. *Journal of Fluid Mechanics*, *602*, 175–207. https://doi.org/10.1017/S0022112008000864

Jones, L. E., Sandberg, R. D., & Sandham, N. D. (2010). Stability and receptivity characteristics of a laminar separation bubble on an aerofoil. *Journal of Fluid Mechanics*, *648*, 257–296. https://doi.org/10.1017/S0022112009993089

Kornilov, V. I., Kavun, I. N., & Popkov, A. N. (2019). Modification of turbulent airfoil section flow using a combined control action. *Thermophysics and Aeromechanics*, *26*(2), 165–178. https://doi.org/10.1134/S0869864319020021

Kuan, C. L., & Wang, T. (1990). Investigation of the intermittent behavior of transitional boundary layer using a conditional averaging technique. *Experimental Thermal and Fluid Science*, *3*(2), 157–173. https://doi.org/10.1016/0894-1777(90)90084-K

Kubacki, S., & Dick, E. (2016). An algebraic intermittency model for bypass, separation-induced and wake-induced transition. *International Journal of Heat and Fluid Flow*, *62*, 344–361. https://doi.org/10.1016/j.ijheatfluidflow.2016.09.013

Kubacki, S., Rarata, Z., Dróżdż, A., Gnatowska, R., Sokolenko, V., & Elsner, W. (2023). Prediction of laminar-to-turbulent transition in a separated boundary layer subjected to an external acoustic forcing. *Archives of Mechanics*. [Submitted]

Kurelek, J. W., Kotsonis, M., & Yarusevych, S. (2018). Transition in a separation bubble under tonal and broadband acoustic excitation. *Journal of Fluid Mechanics*, *853*, 1–36. https://doi.org/10.1017/jfm.2018.546

Lardeau, S., Leschziner, M., & Zaki, T. (2012). Large Eddy Simulation of transitional separated flow over a flat plate and a compressor blade. *Flow, Turbulence and Combustion*, *88*(1–2), 19–44. https://doi.org/10.1007/s10494-011-9353-0

Lengani, D., Simoni, D., Ubaldi, M., Zunino, P., & Bertini, F. (2017). Experimental study of free-stream turbulence induced transition in an adverse pressure gradient. *Experimental Thermal and Fluid Science*, *84*, 18–27. https://doi.org/10.1016/j.expthermflusci.2017.01.019

Lin, J. C. M., & Pauley, L. L. (1996). Low-Reynolds-number separation on an airfoil. *AIAA Journal*, *34*(8), 1570–1577. https://doi.org/10.2514/3.13273

Lou, W., & Hourmouziadis, J. (2000). Separation Bubbles Under Steady and Periodic-Unsteady Main Flow Conditions. *Journal of Turbomachinery*, *122*(4), 634–643. https://doi.org/10.1115/1.1308568

Marxen, O., Lang, M., & Rist, U. (2012). Discrete linear local eigenmodes in a separating laminar boundary layer. *Journal of Fluid Mechanics*, *711*, 1–26. https://doi.org/10.1017/jfm.2012.263

Marxen, O., Rist, U., & Wagner, S. (2004). Effect of Spanwise-Modulated Disturbances on Transition in a Separated Boundary Layer. *AIAA Journal*, *42*(5), 937–944. https://doi.org/10.2514/1.565

Materny, M., Dróżdż, A., Drobniak, S., & Elsner, W. (2008). Experimental analysis of turbulent boundary layer under the influence of adverse pressure gradient. *Archives of Mechanics*, *60*(6), 449–466.

Matsubara, M., & Alfredsson, P. H. (2001). Disturbance growth in boundary layers subjected to free-stream turbulence. *Journal of Fluid Mechanics*, *430*, S0022112000002810. https://doi.org/10.1017/S0022112000002810

Mayle, R. E. (1991). The 1991 IGTI Scholar Lecture: The Role of Laminar-Turbulent Transition in Gas Turbine Engines. *Journal of Turbomachinery*, *113*(4), 509–536. https://doi.org/10.1115/1.2929110

McAuliffe, B. R., & Yaras, M. I. (2005). Separation-Bubble-Transition Measurements on a Low-Re Airfoil Using Particle Image Velocimetry. *Volume 3: Turbo Expo 2005, Parts A and B*, 1029–1038. https://doi.org/10.1115/GT2005-68663

McAuliffe, B. R., & Yaras, M. I. (2008). Numerical Study of Instability Mechanisms Leading to Transition in Separation Bubbles. *Journal of Turbomachinery*, *130*(2), 1–8. https://doi.org/10.1115/1.2750680

Michelis, T., Yarusevych, S., & Kotsonis, M. (2017). Response of a laminar separation bubble to impulsive forcing. *Journal of Fluid Mechanics*, *820*, 633–666. https://doi.org/10.1017/jfm.2017.217

Moreau, S. (2019). Turbomachinery Noise Predictions: Present and Future. *Acoustics*, *1*(1), 92–116. https://doi.org/10.3390/acoustics1010008

Mueller, T. J., & DeLaurier, J. D. (2003). Aerodynamics of Small Vehicles. *Annual Review of Fluid Mechanics*, *35*(1), 89–111. https://doi.org/10.1146/annurev.fluid.35.101101.161102

Nash, E. C., Lowson, M. V., & McAlpine, A. (1999). Boundary-layer instability noise on aerofoils. *Journal of Fluid Mechanics*, *382*, 27–61. https://doi.org/10.1017/S002211209800367X

Nishioka, M., Asai, M., & Yoshida, S. (1990). Control of flow separation by acoustic excitation. *AIAA Journal*, *28*(11), 1909–1915. https://doi.org/10.2514/3.10498

Ol, M., McCauliffe, B., Hanff, E., Scholz, U., & Kaehler, C. (2005, June 6). Comparison of Laminar Separation Bubble Measurements on a Low Reynolds Number Airfoil in Three Facilities. *35th AIAA Fluid Dynamics Conference and Exhibit*. https://doi.org/10.2514/6.2005-5149

Olsman, W. F. J. J., & Colonius, T. (2011). Numerical Simulation of Flow over an Airfoil with a Cavity. *AIAA Journal*, *49*(1), 143–149. https://doi.org/10.2514/1.J050542

Park, D., Shim, H., & Lee, Y. (2020). PIV Measurement of Separation Bubble on an Airfoil at Low Reynolds Numbers. *Journal of Aerospace Engineering*, *33*(1), 1–17. https://doi.org/10.1061/(ASCE)AS.1943-5525.0001099

Piotrowski, W., Elsner, W., & Drobniak, S. (2010). Transition Prediction on Turbine Blade Profile With Intermittency Transport Equation. *Journal of Turbomachinery*, *132*(1), 1–10. https://doi.org/10.1115/1.3072716

Plogmann, B., Herrig, A., & Würz, W. (2013). Experimental investigations of a trailing edge noise feedback mechanism on a NACA 0012 airfoil. *Experiments in Fluids*, *54*(5), 1480. https://doi.org/10.1007/s00348-013-1480-z

Ramesh, O. N., Dey, J., & Prabhu, A. (1996). Transitional intermittency distribution in a three-dimensional constant pressure diverging flow. *Experiments in Fluids*, *21*(4). https://doi.org/10.1007/BF00190675

Rist, U., Lang, M., & Wagner, S. (2004). Investigations on controlled transition development in a laminar separation bubble by means of LDA and PIV. *Experiments in Fluids*, *36*(1), 43–52. https://doi.org/10.1007/s00348-003-0625-x

Rizzetta, D. P., & Visbal, M. R. (2011). Numerical Investigation of Plasma-Based Control for Low-Reynolds-Number Airfoil Flows. *AIAA Journal*, *49*(2), 411–425. https://doi.org/10.2514/1.J050755

Roach, P. E. (1987). The generation of nearly isotropic turbulence by means of grids. *International Journal of Heat and Fluid Flow*, *8*(2), 82–92. https://doi.org/10.1016/0142-727X(87)90001-4

Sarkar, S. (2008). Identification of Flow Structures on a LP Turbine Blade Due to Periodic Passing Wakes. *Journal of Fluids Engineering*, *130*(6). https://doi.org/10.1115/1.2911682

Schlatter, P., Brandt, L., de Lange, H. C., & Henningson, D. S. (2008). On streak breakdown in bypass transition. *Physics of Fluids*, *20*(10), 101505. https://doi.org/10.1063/1.3005836

Schlichting, H., & Gersten, K. (2000). *Boundary-Layer Theory*. Springer Berlin Heidelberg. https://doi.org/10.1007/978-3-642-85829-1

Schubauer, G. B., & Klebanoff, P. S. (1951). Investigation of Separation of the Turbulent Boundary Layer. In *INVESTIGATION OF SEPARATION OF THE Tubulent boundary layer*.

Schubauer, G. B., & Klebanoff, P. S. (1956). *Contributions on the Mechanics of Boundary-Layer Transition*. *1*, 853–863.

Schumacher, K. L., Doolan, C. J., & Kelso, R. M. (2014). The effect of acoustic forcing on an airfoil tonal noise mechanism. *The Journal of the Acoustical Society of America*, *136*(2), EL78–EL83. https://doi.org/10.1121/1.4885485

Serrano, J. S. (2013). Experimental studies on transitional separated boundary layers [Universidad Politécnica de Madrid]. In *Tesis Doctoral*. https://doi.org/10.20868/UPM.thesis.14917

Sieverding, C. H., Bagnera, C., Boege, A. C., Anto`n, J. A. C., & Lue`re, V. (2004). Investigation of the Effectiveness of Various Types of Boundary Layer Transition Elements of Low Reynolds Number Turbine Bladings. *Volume 5: Turbo Expo 2004, Parts A and B*, *5 B*, 1439–1446. https://doi.org/10.1115/GT2004-54103

Simoni, D., Lengani, D., Ubaldi, M., Zunino, P., & Dellacasagrande, M. (2017). Inspection of the dynamic properties of laminar separation bubbles: free-stream turbulence intensity effects for different Reynolds numbers. *Experiments in Fluids*, *58*(6), 66. https://doi.org/10.1007/s00348-017-2353-7

Simoni, D., Ubaldi, M., & Zunino, P. (2012). Loss Production Mechanisms in a Laminar Separation Bubble. *Flow, Turbulence and Combustion*, *89*(4), 547–562. https://doi.org/10.1007/s10494-012-9407-y

Sokolenko, V., Elsner, W., Dróżdż, A., & Gnatowska, R. (2021). Physics of acoustic excitation on boundary layer development. *Acta Physica Polonica A*, *139*(5). https://doi.org/10.12693/APhysPolA.139.613

Stieger, R. D. (2002). *The Effects of Wakes on Separating Boundary Layers in Low Pressure Turbines* (Issue February).

Suzen, Y. B., Huang, P. G., Hultgren, L. S., & Ashpis, D. E. (2003). Predictions of Separated and Transitional Boundary Layers Under Low-Pressure Turbine Airfoil Conditions Using an Intermittency Transport Equation. *Journal of Turbomachinery*, *125*(3), 455–464. https://doi.org/10.1115/1.1580159

Suzuki, S., & Ishii, K. (2001). Numerical Studies of the Separated Flow Around a 2-D Airfoil at Moderate Angle of Attack by Acoustic Excitation. In *Computational Fluid Dynamics 2000*. https://doi.org/10.1007/978-3-642-56535-9_85

Takagi, S., & Konishi, Y. (2010). Frequency Selection Mechanism of Airfoil Trailing-Edge Noise. *Journal of Aircraft*, *47*(4), 1111–1116. https://doi.org/10.2514/1.45138

Talan, M., & Hourmouziadis, J. (2002). Characteristic Regimes of Transitional Separation Bubbles in Unsteady Flow. In *Flow, Turbulence and Combustion* (Vol. 69). https://doi.org/10.1023/A:1027355105017

Tani, I. (1964). Low-speed flows involving bubble separations. *Progress in Aerospace Sciences*, *5*(C), 70–103. https://doi.org/10.1016/0376-0421(64)90004-1

Tanner, L. H., & Blows, L. G. (1976). A study of the motion of oil films on surfaces in air flow, with application to the measurement of skin friction. *Journal of Physics E: Scientific Instruments*, *9*(3), 194–202. https://doi.org/10.1088/0022-3735/9/3/015

Ulrich, R., Ulrich, M., & Norbert, W. (1996). *Direct Numerical Simulation of Some Fundamental Problems Related to Transition in Laminar Separation Bubbles*. *January 1996*, 1–7. https://www.researchgate.net/publication/265073988

Veerasamy, D., & Atkin, C. (2020). A rational method for determining intermittency in the transitional boundary layer. *Experiments in Fluids*, *61*(1), 11. https://doi.org/10.1007/s00348-019-2856-5

Volino, R. J. (2003). Passive Flow Control on Low-Pressure Turbine Airfoils. *Journal of Turbomachinery*, *125*(4), 754–764. https://doi.org/10.1115/1.1626685

Watmuff, J. H. (1999). Evolution of a wave packet into vortex loops in a laminar separation bubble. *Journal of Fluid Mechanics*, *397*, 119–169. https://doi.org/10.1017/S0022112099006138

Wolf, E., Kähler, C. J., Troolin, D. R., Kykal, C., & Lai, W. (2011). Time-resolved volumetric particle tracking velocimetry of large-scale vortex structures from the reattachment region of a laminar separation bubble to the wake. *Experiments in Fluids*, *50*(4), 977–988. https://doi.org/10.1007/s00348-010-

0973-2

Yang, Z., & Voke, P. R. (2001). Large-eddy simulation of boundary-layer separation and transition at a change of surface curvature. *Journal of Fluid Mechanics*, *439*, 305–333. https://doi.org/10.1017/S0022112001004633

Yarusevych, S., & Kotsonis, M. (2017). Steady and transient response of a laminar separation bubble to controlled disturbances. *Journal of Fluid Mechanics*, *813*, 955–990. https://doi.org/10.1017/jfm.2016.848

Yarusevych, S., Sullivan, P. E., & Kawall, J. G. (2007). Effect of Acoustic Excitation Amplitude on Airfoil Boundary Layer and Wake Development. *AIAA Journal*, *45*(4), 760–771. https://doi.org/10.2514/1.25439

Zaman, K. B. M. Q. (1992). Effect of acoustic excitation on stalled flows over an airfoil. *AIAA Journal*, *30*(6), 1492–1499. https://doi.org/10.2514/3.11092

Zaman, K. B. M. Q., & McKinzie, D. J. (1991). Control of laminar separation over airfoils by acoustic excitation. In *AIAA JOURNAL* (Vol. 29, Issue 7, pp. 1075–1083).

Zhang, D. H., Chew, Y. T., & Winoto, S. H. (1995). A proposed intermittency measurement method for transitional boundary layer flows. *Experiments in Fluids*, *19*(6), 426–428. https://doi.org/10.1007/BF00190260

Zhang, X. F., Vera, M., Hodson, H., & Harvey, N. (2006). Separation and Transition Control on an Aft-Loaded Ultra-High-Lift LP Turbine Blade at Low Reynolds Numbers: Low-Speed Investigation. *Journal of Turbomachinery*, *128*(3), 517–527. https://doi.org/10.1115/1.2187524

Summary

A laminar separated boundary layer is often observed in crucial aeronautical processes, including the airflow around wings or turbomachinery blades, and can have a huge effect on efficiency by significantly changing the aerodynamic characteristics, leading to increased drag, decreased lift, and reduced overall performance. Another factor that is difficult to get rid of is the high concentrations of acoustic energy inside aircraft engines and compressors. Thus, the focus of the work was to study the effect of acoustic forcing on a separated laminar boundary layer. In particular, the main purpose was to investigate the mechanism by which acoustics, generated as broadband noise or harmonic excitation, affect the various phases of the development of the laminar separation bubble and especially the laminar-turbulent transition process.

In order to accomplish this objective, the experimental investigation was performed in an open circuit wind tunnel and special design test section, where the boundary layer was developed on a bottom flat plate. The upper wall was shaped according to the assumed distribution of pressure gradient corresponding to the conditions encountered in the axial compressor blading. During the study the advanced measurement techniques (hot-wire anemometry and sound field measurement systems) as well as data post processing was used. For the control of noise conditions inside the test section a suitable acoustic forcing system was designed and developed.

In the thesis two Reynolds numbers i.e. 185 000 and 370 000 were considered. It was shown that the increase in Reynolds number was found to result in a decrease in the size of the separated bubble what was confirmed by C_f and integral parameters of the boundary layer, including H, δ^*, gamma, and θ, which were further validated through smoke visualization conducted at a lower Reynolds number. For both cases Kelvin-Helmholtz and Klebanoff instabilities were observed, the observation of which was confirmed based on Strouhal numbers, integral parameters, and other statistics of the flow.

The second part of the thesis was targeted to describe the effect of acoustic excitation on the laminar separated boundary layer. For a better understanding two sound pressure levels (SPL) were investigated and the effect of pink noise and mono–harmonic excitation of the boundary layer was compared. Based on previous studies it was assumed that the best sensitivity of the separated shear layer to acoustic excitation will be in the range of natural fluctuation frequencies. To determine the proper range of generated frequencies the analysis of the characteristics of the acoustic field in the test section, and the frequency of instability in the near wall flow for non-disturbed cases were performed.

The study showed a significant effect of acoustic excitation on the position of l-t onset which leads to changes in integral boundary layers parameters, shift reattachment point upstream, and the decreasing size of the separated bubble. The use of a higher sound pressure level leads to a faster loss of stability in the flow, and decreasing in the separation bubble size, until it disappears. The main effect is observed in the rear part of the separated bubble. This phenomenon was explained as the interaction between sound waves, and the inviscid Kelvin-Helmholtz instability. However, acoustic did not show a significant effect on the initial part of separated bubble where Klebanoff mode was detected. The comparison of the effects of broadband and monoharmonic forcing, at equivalent SPL levels, reveals distinct differences in PSD spectrum, mode enhancement, and the sensibility of the separated bubble. However, it did not show a significant effect on integral boundary layer parameters.

This investigation presented in the thesis provides valuable information into the underlying physics of the interaction between sound waves and the laminar separated boundary layer. By delving into this unclear relationship, a deeper understanding of the mechanisms which play a significant role, opens the way for advancements in various fields. Including optimisation of the design and performance of aerodynamic systems, noise reduction strategies, and the overall efficiency of a wide range of applications.

Streszczenie

Laminarne oderwanie warstwy przyściennej jest często obserwowane w kluczowych procesach lotniczych, w tym w przepływie powietrza wokół profili lotniczych lub łopatek maszyn wirnikowych. Może to mieć ogromny wpływ na sprawność poprzez znaczną zmianę właściwości aerodynamicznych, prowadzących do zwiększonego oporu, zmniejszenia siły nośnej i zmniejszenia ogólnej wydajności. Kolejnym czynnikiem, który może oddziaływać na przepływ, jest wysokie stężenie energii akustycznej w silnikach lotniczych i sprężarkach. W związku z tym, celem pracy było zbadanie wpływu wymuszeń akustycznych na oderwaną laminarną warstwę przyścienną. W szczególności zbadanie mechanizmu, za pomocą którego akustyka, generowana jako szum szerokopasmowy lub wzbudzenie harmoniczne, wpływa na różne fazy rozwoju laminarnego pęcherza oderwania, a zwłaszcza na proces przejścia laminarno-turbulentnego.

Aby osiągnąć ten cel przeprowadzono badania eksperymentalne w tunelu aerodynamicznym z obiegiem otwartym i specjalnie zaprojektowaną sekcją pomiarową, w której warstwa przyścienna rozwijała się na dolnej płaskiej płycie. Ścianę górną ukształtowano zgodnie z założonym rozkładem gradientu ciśnień odpowiadającym warunkom panującym w łopatkach sprężarki osiowej. W badaniach wykorzystano zaawansowane techniki pomiarowe (anemometria z gorącym włóknem i systemy pomiaru pola akustycznego) oraz przeprowadzono analizę danych pomiarowych. Do kontroli warunków akustycznych wewnątrz sekcji pomiarowej zaprojektowano i opracowano odpowiedni system wymuszania akustycznego.

W pracy przeprowadzono badania dla dwóch liczb Reynoldsa tj. 185 000 i 370 000. Wykazano, że wzrost liczby Reynoldsa powoduje zmniejszenie wielkości pęcherza oderwania, co potwierdza C_f oraz parametry całkowe warstwy przyściennej, w tym H, δ^*, gamma i θ. Zmniejszenie wielkości pęcherza zostało dodatkowo potwierdzone przez wizualizację dymową przeprowadzoną dla niższej liczby Reynoldsa. W obu przypadkach zaobserwowano niestabilności Kelvina-Helmholtza i Klebanoffa, których obserwację

potwierdzono na podstawie liczb Strouhala, parametrów całkowych i danych statystycznych.

Celem drugiej części pracy było opisanie wpływu wzbudzenia akustycznego na oderwaną laminarną warstwę przyścienną. Dla lepszego zrozumienia zbadano dwa poziomy ciśnienia akustycznego (SPL) i porównano wpływ szumu różowego i wzbudzenia monoharmonicznego na warstwę przyścienną. Na podstawie dotychczasowych badań przyjęto, że najlepsza wrażliwość oderwanej warstwy przyściennej na wzbudzenie akustyczne jest w zakresie częstotliwości fluktuacji własnych. W celu określenia właściwego zakresu generowanych częstotliwości przeprowadzono analizę charakterystyki pola akustycznego w badanym odcinku oraz częstotliwości niestabilności warstwy przyściennej.

Badania wykazały istotny wpływ wzbudzenia akustycznego na położenie początku przejścia laminarno-turbulentnego, co prowadzi do zmian parametrów całkowych warstwy przyściennej, przesunięcia punktu ponownego przylgnięcia w górę przepływu oraz zmniejszenia wielkości oddzielonego pęcherza. Zastosowanie wyższego poziomu ciśnienia akustycznego prowadzi do szybszej utraty stabilności przepływu i lub nawet całkowitego zaniku oderwania. Główny efekt obserwuje się w tylnej części pęcherza oderwania. Zjawisko to przypisano jako interakcja między falami dźwiękowymi, generowanymi przez głośnik, a niestabilnością Kelvina-Helmholtza. Oddziaływanie akustyczne nie wykazało znaczącego wpływu na początkową część pęcherza oderwania, w którym wykryto tryb Klebanoffa. Porównanie efektów wymuszania szerokopasmowego i monoharmonicznego, przy jednakowych poziomach SPL, ujawnia wyraźne różnice w widmach i dla obserwowanych niestabilności. Nie wykazało to jednak istotnego wpływu na parametry całkowe warstwy przyściennej.

Badanie to dostarcza cenną informację na temat fizyki leżącej u podstaw interakcji między falami dźwiękowymi a niestabilnością oderwanej warstwy przyściennej. Powiększenie wiedzy w tej skomplikowanej zależności, głębsze zrozumienie mechanizmów, otwiera drogę do postępu w różnych dziedzinach. Takie zrozumienie ma znaczny potencjał w zakresie optymalizacji projektowania i wydajności systemów aerodynamicznych, strategii redukcji hałasu i ogólnej wydajności systemów w szerokim zakresie zastosowań.